UNIVERSITY OF SOUTHAMPTON

FACULTY OF PHYSICAL SCIENCES AND ENGINEERING

School of Physics and Astronomy

A lattice measurement of the $B^*B\pi$ coupling using DWF light quarks and the Relativistic Heavy Quark action

by

Benjamin Samways

Thesis for the degree of Doctor of Philosophy

November 2013

UNIVERSITY OF SOUTHAMPTON

ABSTRACT

FACULTY OF PHYSICAL SCIENCES AND ENGINEERING
School of Physics and Astronomy

Doctor of Philosophy

A LATTICE MEASUREMENT OF THE $B^*B\pi$ COUPLING USING DWF LIGHT QUARKS AND THE RELATIVISTIC HEAVY QUARK ACTION

by Benjamin Samways

I describe a calculation of the $B^*B\pi$ coupling in lattice QCD. The $B^*B\pi$ coupling is directly related to g_b, the leading order low-energy interaction constant of heavy meson chiral perturbation theory. Knowledge of the coupling will help decrease systematic uncertainties in lattice QCD B-physics studies, which are important to constrain the CKM matrix and probe the Standard Model. This calculation is performed with 2+1 flavours of dynamic quarks using the domain wall fermion action. To simulate the heavy b-quark I use a non-perturbatively tuned relativistic heavy quark action which keeps discretisation effects under good control. This allows me to make the first calculation of the $B^*B\pi$ coupling directly at the physical b-quark mass. I conduct a chiral and continuum extrapolation to the physical point and consider all sources of systematic error. The final result including both statistical and sytematic errors is $g_b = 0.567(52)_{stat}(58)_{sys}$.

Contents

Declaration of Authorship xv

Acknowledgements xvii

Nomenclature xix

1 The Standard Model 1
- 1.1 QCD . . . 3
  - 1.1.1 Other Symmetries of QCD . . . 3
    - 1.1.1.1 Chiral Symmetry . . . 4
    - 1.1.1.2 Discrete Symmetries . . . 4
      - Parity . . . 4
      - Charge . . . 4
  - 1.1.2 Strong CP . . . 5
- 1.2 Electroweak Theory . . . 6
- 1.3 The CKM matrix . . . 8
  - 1.3.1 CP violation . . . 9
- 1.4 B-Physics . . . 9
  - 1.4.1 $B^0 - \bar{B}^0$ mixing . . . 10
  - 1.4.2 $B \to \pi l \nu$ . . . 11

2 Effective Field Theories 13
- 2.1 Chiral Perturbation Theory . . . 14
  - 2.1.1 The CCWZ Formalism . . . 15
  - 2.1.2 The Chiral Lagrangian . . . 16
  - 2.1.3 Quark Masses . . . 17
- 2.2 Heavy Quark Effective Theory . . . 18
- 2.3 Heavy Meson Chiral Perturbation Theory . . . 20
  - 2.3.1 $g_{B^*B\pi}$ . . . 20
- 2.4 Symanzik Improvement Program . . . 21

3 Lattice QCD 23
- 3.1 Path Integrals . . . 23
- 3.2 Gauge Actions . . . 26
  - 3.2.1 Improved Gauge Actions . . . 26
- 3.3 Fermion Actions . . . 27
  - 3.3.1 Wilson Fermions . . . 28
  - 3.3.2 Domain Wall Fermions . . . 29

3.3.2.1 Continuum Formulation . . . 30
3.3.2.2 Discretisation . . . 30
3.4 Heavy Quark Actions . . . 33
3.4.1 Static Action . . . 34
3.4.2 Non-relativistic QCD . . . 34
3.4.3 Relativistic Heavy Quark Action . . . 34
3.4.4 RHQ parameter tuning . . . 35
3.5 Lattice Methods . . . 37
3.5.1 Correlation Functions . . . 37
3.5.2 Effective Mass . . . 39
3.5.3 Jack-Knife Analysis . . . 40
3.5.4 Point Sources . . . 40
3.5.5 Extended Sources . . . 41
3.5.6 Conjugate Gradient . . . 42
3.5.7 Preconditioning . . . 43
3.5.8 Low mode averaging . . . 44
3.5.9 Stochastic sources . . . 45
3.5.10 The one-end trick . . . 46

4 The $B^*B\pi$ coupling 49
4.1 Form Factors . . . 50
4.2 Calculational Strategy . . . 52
4.2.1 Method I . . . 52
4.2.2 Method II . . . 53
4.2.3 Method III . . . 54
4.3 Correlation Functions . . . 54
4.3.1 Three-point correlation function . . . 55
4.3.2 Two-point correlation function . . . 56
4.4 Correlator Ratios . . . 56
4.5 Axial Current Renormalisation . . . 58
4.6 Numerical Calculation . . . 59
4.6.1 Ensemble Properties . . . 59
4.6.2 Quark Sources . . . 60
4.6.3 Propagator Generation . . . 60
4.7 Results . . . 62
4.7.1 Three-Point Function . . . 62
4.7.2 Two-Point Functions . . . 63
4.7.3 Ratios . . . 65
4.7.4 Chiral and Continuum extrapolation . . . 69
4.8 Systematic Errors . . . 72
4.8.1 $1/M_Q$ effects . . . 72
4.8.2 Heavy-quark discretisation errors . . . 73
4.8.3 Light-quark and gluon discretisation errors . . . 75
4.8.4 Chiral Extrapolation . . . 75
4.8.5 Lattice Spacing Dependence . . . 77
4.8.6 Finite Volume . . . 79
4.8.7 RHQ parameter uncertainties . . . 80

4.8.7.1 Statistical 80
4.8.7.2 Systematic 81
4.8.8 Unphysical strange-quark mass 81
4.8.9 Final result and error budget 85

5 Conclusions **87**

A Correlator Ratios **89**

B Other Plots **91**
B.1 24^3, $m_l = 0.005$ 91
B.2 24^3, $m_l = 0.010$ 94
B.3 24^3, $m_l = 0.020$ 96
B.4 32^3, $m_l = 0.004$ 98
B.5 32^3, $m_l = 0.006$ 100
B.6 32^3, $m_l = 0.008$ 102

References **105**

List of Figures

1.1 The unitarity triangle. 9
1.2 The unitarity triangle showing the constraints provided by neutral B-meson mixing (Δm_d & Δm_s) and $|V_{ub}|$ from $B \to \pi l \nu$. Plot courtesy of the CKM fitter group [1]. 10
1.3 $B^0 - \bar{B}^0$ mixing proceeds mainly through box diagrams with a top quark in the loop. Being a highly suppressed next-to-leading-order process it is particularly sensitive to new physics [2]. 11

3.1 Chiral modes bound to the walls of the fifth dimension. 31
3.2 Connected (left) and disconnected contributions (right). 38
3.3 An effective mass plot of the B-meson correlator. The blue region shows the region where the correlator has been fitted. 39
3.4 The conjugate gradient algorithm 42
3.5 Pion correlator constructed using 20 eigenmodes and 64 stochastic sources. 45
3.6 The effect of deflation for two different quark masses. For lighter quark masses the Dirac operator is worse conditioned and deflation has a larger effect. 46

4.1 Quark flow diagram for the $\langle B(p)|A_\mu(q)|B^*(p')\rangle$ three-point function with Gaussian smeared source and sink. 53
4.2 Quark flow diagram for the $\langle B(p)|A_\mu(q)|B^*(p')\rangle$ three-point function using a stochastic wall source 53
4.3 Quark flow diagram for the $\langle B(p)|A_\mu(q)|B^*(p')\rangle$ with the operators arranged such that precalculated propagators can be used. 54
4.4 B-meson two-point functions with no smearing on the heavy propagator (left) and Gaussian smearing at both ends (right). In both cases the light-quark propagator has a point source and sink. Calculated using 550 configurations of the 24^3 $m_l = 0.005$ ensemble. 61
4.5 B-meson two-point functions with a smeared source and point sink on the heavy propagator (left) and point source and smeared sink (right). In both cases the light-quark propagator has a point source and sink. Calculated using 550 configurations of the 24^3 $m_l = 0.005$ ensemble. . . . 61
4.6 The three-point correlation functions summed over all spatial indices for $t_y = 6$ (left) and $t_y = 8$ (right). The top plots are on a log scale, whereas the lower plots are on a linear scale. The point where the correlation function blows-up is where the meson creation and annihilation operators are on the same lattice space. 62
4.7 Contributions to the three-point correlator for $t_x > t_y$ 64
4.8 Contributions to the three-point correlator for $t_x \leq t_y$ 65

4.9 The sum of all contributions to the three-point correlator as shown in figures 4.7 and 4.8 assuming immediate ground-state dominance, and setting all the matrix elements to unity. The shape closely matches what is seen in the actual calculation of the three-point function (see Figure 4.6). 66
4.10 Relative size of the eight contributions to the three-point function arising due to the periodicity of the lattice. To extract the correct matrix element the contribution of interest is C. This contribution dominates for large t_x. 66
4.11 B-meson effective mass (left) at zero momentum and B^*-meson effective mass at zero momentum, both on the 24^3, $m_l = 0.005$ ensemble 67
4.12 B^*-meson effective mass/energy (left) at the first non-zero momentum and B^*-meson effective mass/energy at the second non-zero momentum, both on the 24^3, $m_l = 0.005$ ensemble 67
4.13 B-meson effective mass (left) at zero momentum and B^*-meson effective mass at zero momentum, both on the 32^3, $m_l = 0.006$ ensemble 67
4.14 B^*-meson effective mass/energy (left) at the first non-zero momentum and B^*-meson effective mass/energy at the second non-zero momentum, both on the 32^3, $m_l = 0.006$ ensemble 68
4.15 The coupling g_b with jack-kife errors plotted against the bin size. No effect is seen, so we conclude each configuration is suitably uncorrelated. . 68
4.16 The ratio R_1 evaluated for different values of t_y on the 24^3, $m_l = 0.005$ ensemble. The longest plateau is seen for the value t_y=6. We show the region in the latter half of the lattice where we expect to see the signal. . 69
4.17 The ratios R_1, R_2 and R_3 calculated on the 24^3, $m_l = 0.005$ ensemble . . 70
4.18 The q^2 dependence of the form factor A_1 (left) and the linear extrapolation of the ratio G_2/G_1 to $q^2 = 0$ on 24^3, $m_l = 0.005$ ensemble 70
4.19 Combined chiral and continuum extrapolation to the physical point. The blue points and dashed line are the 24^3 data points and fit respectively. The red points, and dashed line correspond to the finer 32^3 ensembles. The green solid is the extrapolation to the continuum, surrounded by a one sigma error band. The point where the green line crosses the vertical dashed line corresponds to a physical pion mass. The fit function is given by Eq. (4.44). 72
4.20 Chiral fits of the 32^2 data points (top) and the data points from both lattices (bottom). The data points in both plots are fitted to Eq. (4.43). . 76
4.21 Increasing the value of f_π used in the fit (Eq. 4.44) by 25% (top) and decreasing by 25% (bottom). 77
4.22 Chiral fit (Eq. 4.44) with the heaviest masses missing (top), and a simple linear fit ($g_0(1 + m_{pi}^2 + \beta a^2)$) to all the data (bottom). 78
4.23 g_b as a function of the three RHQ parameters $m_0 a$ (top), c_p (left) and ξ (right). The vertical dashed line shows the tuned parameter value, and the shaded region shows the systematic error coming from the heavy-quark discretisation effects. 82
4.24 g_b as a function of the three RHQ parameters $m_0 a$ (top), c_p (left) and ξ (right). The vertical dashed line shows the tuned parameter value, and the shaded region shows the systematic error coming from the lattice scale uncertainty. 83

4.25 g_b as a function of the three RHQ parameters m_0a (left), c_p (middle) and ξ (right). The vertical dashed line shows the tuned parameter value, and the shaded region shows the systematic error coming from the experimental uncertainties in the quantities used to tue the paramaters. 84
4.26 Reweighting on a subset of configurations. 32^3 $m_l = 0.004$ (left), 32^3 $m_l = 0.006$ (right) 85

5.1 Comparison of recent calculations of the HMχPT coupling. The inner bars represent statistical errors and the outer bars represent systematic errors, except Becirevic and Hass who only quote a single error. Quenched calculations are represented with circular markers, the n_f=2 calculations are shown with square markers and diamond markers correspond to n_f=2+1 calculations. 88

B.1 Ratio R_1 on the 24^3, $m_l = 0.005$ ensemble. 91
B.2 Ratio R_2 on the 24^3, $m_l = 0.005$ ensemble, at the first (left) and second (right) non-zero momentum. 92
B.3 Ratio R_3 on the 24^3, $m_l = 0.005$ ensemble, at the first (left) and second (right) non-zero momentum. 92
B.4 Ratio R_4 on the 24^3, $m_l = 0.005$ ensemble, at the first (left) and second (right) non-zero momentum. 92
B.5 B meson (left) and B^* meson effective mass on the 24^3, $m_l = 0.005$ ensemble, at zero momentum. 92
B.6 B^* meson effective mass on the 24^3, $m_l = 0.005$ ensemble at the first non-zero momentum (left) and the second non-zero momentum (right). . . 93
B.7 $A_1(q^2)$ and $G2/G1(q^2)$ on the 24^3, $m_l = 0.005$ ensemble. 93
B.8 Ratio R_1 on the 24^3, $m_l = 0.010$ ensemble. 94
B.9 Ratio R_2 on the 24^3, $m_l = 0.010$ ensemble, at the first (left) and second (right) non-zero momentum. 94
B.10 Ratio R_3 on the 24^3, $m_l = 0.010$ ensemble, at the first (left) and second (right) non-zero momentum. 94
B.11 Ratio R_4 on the 24^3, $m_l = 0.010$ ensemble, at the first (left) and second (right) non-zero momentum. 95
B.12 B meson (left) and B^* meson effective mass on the 24^3, $m_l = 0.010$ ensemble, at zero momentum. 95
B.13 B^* meson effective mass on the 24^3, $m_l = 0.010$ ensemble at the first non-zero momentum (left) and the second non-zero momentum (right). . . 95
B.14 $A_1(q^2)$ and $G2/G1(q^2)$ on the 24^3, $m_l = 0.010$ ensemble. 95
B.15 Ratio R_1 on the 24^3, $m_l = 0.020$ ensemble. 96
B.16 Ratio R_2 on the 24^3, $m_l = 0.020$ ensemble, at the first (left) and second (right) non-zero momentum. 96
B.17 Ratio R_3 on the 24^3, $m_l = 0.020$ ensemble, at the first (left) and second (right) non-zero momentum. 96
B.18 Ratio R_4 on the 24^3, $m_l = 0.020$ ensemble, at the first (left) and second (right) non-zero momentum. 97
B.19 B meson (left) and B^* meson effective mass on the 24^3, $m_l = 0.020$ ensemble, at zero momentum. 97
B.20 B^* meson effective mass on the 24^3, $m_l = 0.020$ ensemble at the first non-zero momentum (left) and the second non-zero momentum (right). . . 97

B.21 $A_1(q^2)$ and $G2/G1(q^2)$ on the 24^3, $m_l = 0.020$ ensemble. 97
B.22 Ratio R_1 on the 32^3, $m_l = 0.004$ ensemble. 98
B.23 Ratio R_2 on the 32^3, $m_l = 0.004$ ensemble, at the first (left) and second (right) non-zero momentum. 98
B.24 Ratio R_3 on the 32^3, $m_l = 0.004$ ensemble, at the first (left) and second (right) non-zero momentum. 98
B.25 Ratio R_4 on the 32^3, $m_l = 0.004$ ensemble, at the first (left) and second (right) non-zero momentum. 99
B.26 B meson (left) and B^* meson effective mass on the 32^3, $m_l = 0.004$ ensemble, at zero momentum. 99
B.27 B^* meson effective mass on the 32^3, $m_l = 0.004$ ensemble at the first non-zero momentum (left) and the second non-zero momentum (right). . . 99
B.28 $A_1(q^2)$ and $G2/G1(q^2)$ on the 32^3, $m_l = 0.004$ ensemble. 99
B.29 Ratio R_1 on the 32^3, $m_l = 0.006$ ensemble. 100
B.30 Ratio R_2 on the 32^3, $m_l = 0.006$ ensemble, at the first (left) and second (right) non-zero momentum. 100
B.31 Ratio R_3 on the 32^3, $m_l = 0.006$ ensemble, at the first (left) and second (right) non-zero momentum. 100
B.32 Ratio R_4 on the 32^3, $m_l = 0.006$ ensemble, at the first (left) and second (right) non-zero momentum. 101
B.33 B meson (left) and B^* meson effective mass on the 32^3, $m_l = 0.006$ ensemble, at zero momentum. 101
B.34 B^* meson effective mass on the 32^3, $m_l = 0.006$ ensemble at the first non-zero momentum (left) and the second non-zero momentum (right). . . 101
B.35 $A_1(q^2)$ and $G2/G1(q^2)$ on the 32^3, $m_l = 0.006$ ensemble. 101
B.36 Ratio R_1 on the 32^3, $m_l = 0.008$ ensemble. 102
B.37 Ratio R_2 on the 32^3, $m_l = 0.008$ ensemble, at the first (left) and second (right) non-zero momentum. 102
B.38 Ratio R_3 on the 32^3, $m_l = 0.008$ ensemble, at the first (left) and second (right) non-zero momentum. 102
B.39 Ratio R_4 on the 32^3, $m_l = 0.008$ ensemble, at the first (left) and second (right) non-zero momentum. 103
B.40 B meson (left) and B^* meson effective mass on the 32^3, $m_l = 0.008$ ensemble, at zero momentum. 103
B.41 B^* meson effective mass on the 32^3, $m_l = 0.008$ ensemble at the first non-zero momentum (left) and the second non-zero momentum (right). . . 103
B.42 $A_1(q^2)$ and $G2/G1(q^2)$ on the 32^3, $m_l = 0.008$ ensemble. 103

List of Tables

1.1 Quantum numbers of the Dirac bilinears in the form J^{PC}, where P represents the eigenvalue of parity (± 1), C charge and J is the total spin. Euclidean versions of these bilinears are commonly used in Lattice QCD as *interpolating* operators to produce states of the required quantum numbers. 5

1.2 The Standard Model matter content of the first generation, and each particle's electric charge Q, third component of weak iso-spin T_3 and hypercharge Y. 6

4.1 Propagator calculation time using 32 nodes of Iridis 3 on the RBC-UKQCD 24^3 x 64, $m_{ud} = 0.005$, $\beta = 2.13$ configurations. 52

4.2 Axial current renormalisation factors used in this work 59

4.3 Ensemble properties. All ensembles are generated using 2+1 flavours of Domain Wall Fermions and the Iwasaki gauge action. The fifth dimensional extent of both lattices is $L_S = 16$ and the domain wall height $M_5 = 1.8$, corresponding to a residual chiral symmetry breaking of $m_{res}^{24} a = 0.003$, $m_{res}^{32} a = 0.0007$. 60

4.4 Parameters used to apply covariant Gaussian smearing to all heavy-quark propagator sources calculated in this work 61

4.5 Tuned RHQ parameters for b-quarks and their uncertainties, these are statistical, heavy-quark discretisation effects, lattice scale uncertainty, and experimental uncertainties respectively [3]. 62

4.6 Fit ranges used for the two-point functions and the ratios. For non-zero momenta equivalent combinations are averaged. 71

4.7 Variation in g_b as a function of the lattice spacing, where $a_{24}^{-1} = 1.729(28)$ GeV and $a_{32}^{-1} = 2.28(3)$ GeV 79

4.8 Finite volume corrections to the effective coupling 80

4.9 Values of the (unrenormalised) coupling constant g_b on the 24^3 $m_l = 0.005$ ensemble calculated directly at the tuned RHQ parameters, and interpolated to the tuned point under the jack-knife. The difference between the two values is negligible. 81

4.10 The effect of RHQ parameter systematic errors on g_b. Each parameter was shifted by one sigma and the effect on g_b calculated by extrapolation using equation (4.68). 82

4.11 Parameters and results of strange-quark mass reweighting. The Δg_b column gives the difference between the coupling at the simulated and physical strange mass, calculated underneath a jack-knife. The differences are not statistically significant. 85

4.12 Systematic error budget. 85

Declaration of Authorship

I, Benjamin Samways , declare that the thesis entitled *A lattice measurement of the $B^*B\pi$ coupling using DWF light quarks and the Relativistic Heavy Quark action* and the work presented in the thesis are both my own, and have been generated by me as the result of my own original research. I confirm that:

- this work was done wholly or mainly while in candidature for a research degree at this University;
- where any part of this thesis has previously been submitted for a degree or any other qualification at this University or any other institution, this has been clearly stated;
- where I have consulted the published work of others, this is always clearly attributed;
- where I have quoted from the work of others, the source is always given. With the exception of such quotations, this thesis is entirely my own work;
- I have acknowledged all main sources of help;
- where the thesis is based on work done by myself jointly with others, I have made clear exactly what was done by others and what I have contributed myself;

Signed:.....

Date:.....

Acknowledgements

Firstly I would like to thank Jonathan Flynn for his help and guidance over the last four years. I would not have got to the point of writing this thesis if it were not for his patience. This work was supported by an EPSRC Doctoral Training Centre grant (EP/G03690X/1) which has funded me to complete this research. I also acknowledge the use of the IRIDIS High Performance Computing Facility and associated support services at the University of Southampton, USQCD resources at Fermilab, as well as computers at Brookhaven National Laboratory and Columbia University. I am also grateful for much advice, and helpful input from the members of the RBC/UKQCD collaboration, including but not limited to, Oliver Witzel, Ruth Van de Water, Christoph Lehner, and Norman Christ. Finally, thanks to Jo for putting up with me. I love you.

Nomenclature

SM	The Standard Model
SSB	Spontaneous Symmetry Breaking
QCD	Quantum Chromodynamics
VEV	Vacuum Expectation Value
EFT	Effective Field Theory
NGB	Nambu-Goldstone Boson
LQCD	Lattice Quantum Chromodynamics
DWF	Domain Wall Fermion
NLO	Next-to-leading order
RHQ	Relativistic Heavy Quark
LEC	Low Energy Constant

Chapter 1

The Standard Model

This thesis presents a calculation of the $B^*B\pi$ coupling, which is directly related to the leading order low-energy interaction constant, g_b, of heavy meson chiral perturbation theory (HMχPT). This is the effective theory that describes the interactions of light pseudoscalar mesons (π, κ, η) with heavy-light mesons, such as the B and the B^*. The main relevance of this work is that HMχPT can be used to describe the chiral behaviour of heavy meson matrix elements calculated on the lattice and link them to quantities at physical light-quark masses, rather that the unphysically large masses at which lattice computations are typically performed. By fixing the unknown coupling constant, g_b, we can decrease the systematic uncertainties that are introduced into lattice calculations when performing extrapolations guided by the theory.

Some of the strongest tests of the Standard Model come from flavour physics and specifically the B-meson sector. These tests rely on having both accurate experimental results and precise theoretical input. Currently, for a number of interesting processes, the lattice input is the limiting factor. Some examples of these processes are discussed at the end of this chapter.

One of the main difficulties in Lattice QCD calculations is dealing with the large range of quark masses that we observe in nature. The small masses of the light quarks can cause a critical slow-down in the numerical algorithms, and the masses of heavy quarks can lie above the UV cut-off introduced by discretising the theory. In this thesis the calculations are performed using a non-perturbatively tuned relativistic action for the heavy b-quarks. This allows us to perform simulations directly at the the b-quark mass, rather than in the infinite mass limit, or by using much lighter charm quarks, as in all previous similar calculations. Furthermore, we utilise the domain wall fermion action to simulate light quarks. This provides favourable chiral properties and is automatically $\mathcal{O}(a)$ improved, hence reducing cut-off effects, albeit at extra computational cost.

This thesis is set out as follows: in the rest of this chapter I will introduce the Standard Model (SM) of particle physics and go on to discuss the relevance of heavy-quark physics as a means to test the theory. Chapter 2 is dedicated to effective theories, with

its main aim being to introduce HMχPT. In Chapter 3 I will give an overview of Lattice QCD and describe the methods used in this work. Finally, Chapter 4 contains the focus of this thesis — the determination of the $B^*B\pi$ coupling. This includes extrapolating to physical light quark masses and taking the continuum limit, as well as an in depth discussion of all the uncertainties present in the calculation.

The Standard Model (SM) of particle physics represents our best current understanding of fundamental particles and their interactions. Although it cannot claim to be a complete theory, one glaring omission being its inability to incorporate General Relativity, it is highly successful and continues to make accurate predictions within the realm of its applicability. The matter content of the theory is grouped into three families with equivalent properties, but increasing mass. In each family there are two quarks, one of 'up-type' and one of 'down-type', known as *up*, *down*, *strange*, *charm*, *top* and *bottom*. Each family also contains two leptons, an *electron-type* and a *neutrino-type*. These are the *electron*, *neutrino*, *muon*, *muon-neutrino*, *tau*, and *tau-neutrino*. All of these particles are considered fundamental, meaning they have no internal sub-structure. The particles all have mass in the SM, except the neutrinos. This contradictory to modern experimental evidence [4], and although many extensions to the theory tackle this issue, none of these have yet been validated.

The interactions between the particles are mediated by the exchange of gauge-bosons, integer-spin particles that arise due to the local symmetries of the theory. There are four types of gauge-boson. The photon, W and Z-bosons are the force-carriers of the electroweak sector, and the gluons are the force-carriers of QCD. Of these, only the W and Z-bosons have mass.

The final piece of the jigsaw is a particle that has proved particularly elusive. The Higgs boson, or perhaps more diplomatically, the Standard Model Scalar, is an integral ingredient of the electroweak theory. It appears as a result of the spontaneous symmetry breaking (SSB) of electroweak gauge symmetry by the Higgs potential and provides a mechanism to give particles mass in a gauge invariant way. At the time of writing the discovery of the SM Higgs is all but confirmed by the ATLAS and CMS experiments at the LHC [5, 6]. A resonance has been seen near 125 GeV in both detectors, with a significance of more than 5-sigma, and the most current data [7, 8] also points to agreement with the spin-parity ($J^P = 0^+$) predictions of the SM.

This chapter introduces the two main components of the Standard Model, Quantum Chromodynamics and the Electroweak theory, before discussing the phenomenology of B-mesons, an area of particular relevance to this thesis.

1.1 QCD

Quantum Chromodynamics (QCD) is the theory that describes the strong interaction between quarks and gluons. The quarks carry an internal symmetry known as colour which transforms under the fundamental representation of $SU(3)_c$. The promotion of this symmetry to a local (gauge) symmetry demands the introduction of eight gluon fields corresponding to the eight generators of the $SU(3)_c$ algebra. The QCD Lagrangian is

$$\mathcal{L}_{QCD} = -\frac{1}{4} F^a_{\mu\nu} F^{a\,\mu\nu} + \sum_f \bar{q}_f \left(i \not{D} - m_f \right) q_f, \tag{1.1}$$

with f labeling the six quark flavours. The covariant derivative is given by

$$D_\mu = \partial_\mu + igT^a A^a_\mu, \tag{1.2}$$

where the T^a are the eight generators of the Lie algebra. The gluon fields necessarily transform in the adjoint representation to ensure that the covariant derivative maintains the same transformation properties as the quark fields. The field strength tensor $F^a_{\mu\nu}$, contains the generators, and due to the non-abelian nature of $SU(3)$, the structure constants f^{abc} also appear.

$$F^a_{\mu\nu} = \partial_\mu A^a_\nu - \partial_\nu A^a_\mu - g f^{abc} A^b_\mu A^c_\nu \tag{1.3}$$

This gives rise to gluon-gluon interactions and hence the highly non-linear nature of QCD. The QCD coupling constant g is observed to be large at hadronic scales, which means that perturbation theory is not applicable in this regime. In fact, under renormalisation the coupling has been shown to *run*, meaning at low energies, or large distances, the coupling grows. This provides an explanation for quark confinement — the observation that quarks and gluons only appear in bound states. The failure of perturbation theory to be a useful calculational tool at low energy scales means other techniques are needed to explain the complex pattern of hadronic phenomena in terms of QCD. The most powerful of such techniques is Lattice QCD, which I will introduce in Chapter 3.

1.1.1 Other Symmetries of QCD

The Lagrangian of QCD possesses a number of symmetries on top of the $SU(3)_C$ gauge symmetry on which the theory is based. Some of these symmetries continue to hold at the quantum level and some are only present in the classical Lagrangian. As is always the case with symmetries, they provide powerful predictive tools for theorists.

1.1.1.1 Chiral Symmetry

In the limit of vanishing quark masses the QCD Lagrangian is entirely chiral. This means it can be divided into separate left and right-handed sectors that transform independently under $SU(3)_{L,R}$ flavour. In reality, of course, the quarks are not massless, but considered against $\Lambda_{QCD} \sim 200$ MeV, the dynamically generated scale of the theory, the approximation is good for the light flavours (u, d, s). A consequence of this symmetry should be that the nucleon and its negative parity partner the N^* have degenerate masses. No such degeneracy is seen, and the mass splitting is far too large to be explained by the explicit symmetry breaking due to the small quark masses. The explanation is that the chiral symmetry is spontaneously broken. This idea is explored more in Chapter 2 when we discuss Chiral Perturbation Theory.

1.1.1.2 Discrete Symmetries

Parity A parity transformation is the reflection of all position space components of a particle, this reverses the momentum without changing its spin. The transformation of a quark field under parity is given by

$$P\psi(t, \bar{x})P^\dagger = \eta_a \gamma^0 \psi(t, -\bar{x}) \tag{1.4}$$

where η_a is some complex phase. Bosons are eigenstates of parity, but fermions are not. We can however form parity eigenstates by combining quark fields into Dirac bilinears. The eigenstates of these operators are shown in Table 1.1. These prove useful as interpolating operators to produce states with specific quantum numbers in Lattice QCD simulations.

Charge Charge conjugation is the exchange of a particle with its antiparticle. In terms of a unitary operator, C, the transformation acts on a quark field as

$$C\psi C^\dagger = -i(\bar{\psi}\gamma^0\gamma^2)^T. \tag{1.5}$$

Again, although a quark field is not an eigenstate of charge, we can form Dirac bilinears which are. From the properties in Table 1.1 we can see that QCD is completely invariant under C, P and a combined CP transformation. There is a third symmetry worth mentioning — time reversal. Again QCD is invariant separately under T and combined CPT, furthermore any local and Lorentz-covariant quantum field theory is invariant under CPT [9, 10] and no evidence has been seen to contradict this. In contrast, CP is known to be broken by the electroweak sector of the SM.

	J^{PC}	Dirac Bilinears
Scalar	0^{++}	$\bar{\psi}\psi,\ \bar{\psi}\gamma_0\psi$
Pseudo-scalar	0^{-+}	$\bar{\psi}\gamma_5\psi,\ \bar{\psi}\gamma_0\gamma_5\psi$
Vector	1^{--}	$\bar{\psi}\gamma_i\psi,\ \bar{\psi}\gamma_0\gamma_i\psi$
Axial-vector	1^{++}	$\bar{\psi}\gamma_i\gamma_5\psi$
Tensor	1^{+-}	$\bar{\psi}\gamma_i\gamma_j\psi$

Table 1.1: Quantum numbers of the Dirac bilinears in the form J^{PC}, where P represents the eigenvalue of parity (± 1), C charge and J is the total spin. Euclidean versions of these bilinears are commonly used in Lattice QCD as *interpolating* operators to produce states of the required quantum numbers.

1.1.2 Strong CP

There is one caveat to the previous statement that QCD is invariant under CP. If we allow all the terms permitted by gauge invariance in the QCD Lagrangian there is one more that we have not previously mentioned:

$$\mathcal{L}_\theta = \theta \frac{g^2}{32\pi^2} F^a_{\mu\nu} \tilde{F}^{\mu\nu a} \tag{1.6}$$

where the dual field strength tensor, $\tilde{F}^a_{\mu\nu}$, is defined as

$$\tilde{F}^a_{\mu\nu} = \frac{1}{2}\epsilon_{\mu\nu\rho\sigma} F^{\rho\sigma a} \tag{1.7}$$

This term can be written as a total derivative so you expect that it would not contribute to the action. However, t'Hooft [11, 12] showed than non-trivial gauge configurations are possible where the surface integral does not vanish. This is important to explain the large mass of the η' meson, because if this term vanished it would imply a conserved $U(1)_A$ symmetry (see Section 2.1). This term explicitly breaks CP, however experimentally no CP breaking is seen in the QCD sector. This means the coefficient θ must be vanishingly small. Furthermore, when weak interactions are included, the quark mass matrix is in general complex. This has the effect that when diagonalising to get to the physical mass matrix (see Section 1.2) the coefficient θ gains an extra term:

$$\theta \to \theta + \text{Arg det} M \tag{1.8}$$

where M is the quark mass matrix. The lack of explanation for the smallness of the θ term is known as the strong CP problem. For a more detailed explanation, and a discussion of proposed solutions see [13].

1.2 Electroweak Theory

The electroweak theory of Salam, Glashow and Weinberg [14, 15, 16] unifies the electromagnetic and weak interactions into a single gauge theory. The matter content of the SM is packaged into left-handed doublets and right-handed singlets of the gauge group $SU(2)_L$.

$$\begin{pmatrix} \nu \\ e \end{pmatrix}_L, \begin{pmatrix} u \\ \tilde{d} \end{pmatrix}_L, \begin{pmatrix} \nu_\mu \\ \mu \end{pmatrix}_L, \begin{pmatrix} s \\ \tilde{c} \end{pmatrix}_L, \begin{pmatrix} \nu_\tau \\ \tau \end{pmatrix}_L, \begin{pmatrix} t \\ \tilde{b} \end{pmatrix}_L, \tag{1.9}$$

$$e_R,\ u_R,\ d_R,\ \mu_R,\ s_R,\ c_R,\ \tau_R,\ t_R,\ b_R \tag{1.10}$$

The tilde on the 'down-type' quarks indicate that these are the weak, rather than mass, eigenstates. The full gauge group of the electroweak theory is $SU(2)_L \times U(1)_Y$, where the Y stands for hypercharge. All matter transforms under $U(1)_Y$, with the representation given by the hypercharge. For instance,

$$e_R \to e'_R = e^{-\omega Y(e_R)} e_R, \text{ with } Y(e_R) = -1 \tag{1.11}$$

In the unbroken theory there are four gauge bosons, three W^a_μ corresponding to the

	u_L	d_L	u_R	d_R	e_L	e_R	ν_L
Q	2/3	-1/3	2/3	-1/3	-1	-1	0
T_3	1/2	-1/2	0	0	-1/2	0	1/2
Y	1/3	1/3	4/3	-2/3	-1	-2	-1

Table 1.2: The Standard Model matter content of the first generation, and each particle's electric charge Q, third component of weak iso-spin T_3 and hypercharge Y.

generators of $SU(2)$ and a B_μ from the $U(1)_Y$ which is related to the photon of electromagnetism. The final ingredient is the Higgs doublet which has weak quantum numbers $(2, \frac{1}{2})$ and a symmetry breaking potential

$$V(\Phi) = -\mu^2 \Phi_i^\dagger \Phi^i + \lambda \left(\Phi_i^\dagger \Phi^i \right)^2 \tag{1.12}$$

that gives rise to a non-zero vacuum expectation value (VEV)

$$\langle \Phi \rangle = \begin{pmatrix} 0 \\ v \end{pmatrix}. \tag{1.13}$$

The breaking of the electroweak gauge group $SU(2)_L \times U(1)_Y \to U(1)_Q$ produces three Goldstone bosons that provide the longitudinal component to the gauge bosons, effectively giving them a mass. The zeroth component W^0_μ mixes with the B_μ, therefore we

diagonalise by introducing the combinations

$$\begin{aligned} Z_\mu &= \cos\theta_w W_\mu^0 - \sin\theta_w B_\mu \\ A_\mu &= \sin\theta_w W_\mu^0 + \cos\theta_w B_\mu, \end{aligned} \tag{1.14}$$

where θ_w is known as the Weinberg angle. This produces a massive vector boson Z_μ and a massless photon A_μ. The charged $W_\mu^\pm = (W_\mu^1 \pm W_\mu^2)/\sqrt{2}$ acquire masses proportional to v, as well as the Higgs itself becoming massive. The mixing angle θ_w gives a relationship between the masses of the W and Z bosons

$$\cos\theta_w = \frac{m_W}{m_Z} \tag{1.15}$$

which can be used to determine the angle experimentally. It is not possible to add explicit mass terms to the Lagrangian, as this would mix the left and right handed components, and break the gauge symmetry. Instead we introduce Yukawa interactions between left and right-handed components and the Higgs doublet. For instance,

$$\mathcal{L}_{Yukawa} = -\lambda_e \bar{l}_L \cdot \Phi e_R + h.c. \tag{1.16}$$

which gives a mass to the electron when the Higgs field gets a VEV, and introduces a three-point interaction $\bar{e}He$. The upper component of the lepton doublet (the neutrino) does not acquire a mass. A similar technique is used to generate quark masses, except now it is necessary to introduce an second term to provide masses to the up-quarks. There are no symmetry constraints to disallow Yukawa terms that mix quarks from different generations, therefore we must consider the couplings λ^{ij} as matrices in flavour space.

$$\mathcal{L}_{Yukawa} = -\lambda_d^{ij} \bar{q}_{iL} \cdot \Phi d_{jR} - \lambda_u^{ij} \epsilon_{ab} \bar{q}_{iL}^a \Phi^{\dagger b} u_{jR} + h.c. \tag{1.17}$$

Physical quarks correspond to a basis were the mass matrix is diagonal, which can be found through bi-unitary transformations

$$D_u = U_u^\dagger \lambda_u W_u, \quad D_d = U_d^\dagger \lambda_d W_d. \tag{1.18}$$

To achieve this we also make the relevant rotations to the quark fields,

$$\begin{aligned} u_R^i &\to W_u^{ij} u_R^j, \\ d_R^i &\to W_d^{ij} d_R^j, \\ u_L^i &\to U_u^{ij} u_L^j, \\ d_L^i &\to U_d^{ij} d_L^j, \end{aligned} \tag{1.19}$$

This has no physical effect on the quark kinetic terms, which are diagonal in flavour space so the rotation matrices cancel. The same is true for the neutral current interactions involving photons, or the Z boson. The interesting effect involves the charged interactions which are mediated by a $W^\pm$ boson. Here the transformation matrices no

longer cancel. For instance,

$$-\frac{g}{2\sqrt{2}}\bar{\tilde{u}}^i_L\gamma^\mu\tilde{d}^i_L W^-_\mu \rightarrow -\frac{1}{2\sqrt{2}}\bar{u}^i_L\gamma^\mu(U^\dagger_u U_d)^{ij}d^j_L W^-_\mu . \tag{1.20}$$

The charged current interactions therefore mix flavour states. The matrix

$$V = U^\dagger_u U_d \tag{1.21}$$

is known as the CKM mixing matrix, from its originators Cabibbo, Kobayashi and Maskawa [17, 18], and characterises the amount of mixing between different generations.

1.3 The CKM matrix

The CKM matrix relates the physical mass eigenstates to the weak flavour eigenstates.

$$\begin{pmatrix} \tilde{d} \\ \tilde{s} \\ \tilde{b} \end{pmatrix} = \begin{pmatrix} V_{ud} & V_{us} & V_{ub} \\ V_{cd} & V_{cs} & V_{cb} \\ V_{td} & V_{ts} & V_{tb} \end{pmatrix} \begin{pmatrix} d \\ s \\ b \end{pmatrix} \tag{1.22}$$

It is a 3×3 unitary matrix and as such has nine free parameters, three rotation angles and six phases. Of the complex phases we can absorb five into re-definitions of the quark fields, but one must remain. The standard parameterisation [19] uses three angles θ_{12}, θ_{23} θ_{13} and a phase δ_{13}.

$$V = \begin{pmatrix} c_{12}c_{13} & s_{12}c_{13} & s_{13}e^{-i\delta_{13}} \\ -s_{12}c_{23} - c_{12}s_{23}s_{13}e^{-i\delta_{13}} & c_{12}c_{23} - s_{12}s_{23}s_{13}e^{-i\delta_{13}} & s_{23}c_{13} \\ s_{12}s_{23} - c_{12}c_{23}s_{13}e^{-i\delta_{13}} & -c_{12}c_{23} - s_{12}s_{23}s_{13}e^{-i\delta_{13}} & c_{23}c_{13} \end{pmatrix} \tag{1.23}$$

In the above matrix $s_{12} = \sin\theta_{12}$ and $c_{23} = \cos\theta_{23}$ etc. The complex phase is of particular significance as this is the only place[1] where CP violation can enter into the Standard Model. A central property of the CKM matrix is its unitarity. This provides the constraints

$$\sum_j V_{ij}V^*_{kj} = 0. \tag{1.24}$$

For each choice of i and k this defines a triangle, each with a different shape but a common area, related to the CP-violating phase. The most common of these so called *unitarity triangles* is

$$V_{ud}V^*_{ub} + V_{cd}V^*_{cb} + V_{td}V^*_{tb} = 0 \tag{1.25}$$

which is commonly divided by the best known of the elements $V_{cd}V^*_{cb}$ to create a triangle in the complex plane with vertices at $(0,0)$, $(1,0)$ and $(\bar{\rho},\bar{\eta})$.

[1] Except through the QCD strong CP term, however experimental evidence overwhelmingly points to this being zero.

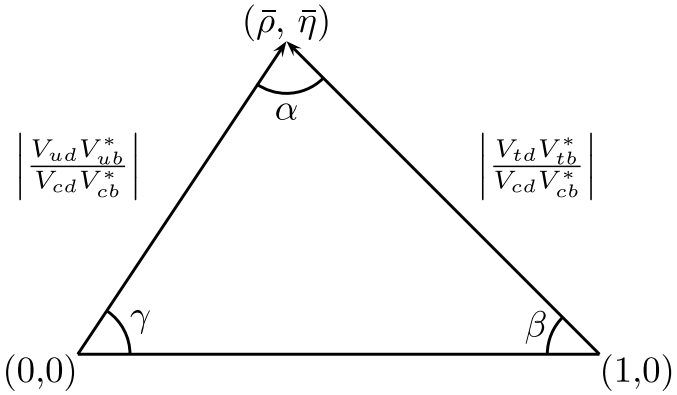

Figure 1.1: The unitarity triangle.

1.3.1 CP violation

The violation of CP symmetry is of particular importance for our understanding of nature. If CP were conserved the laws of physics would be identical for matter and antimatter. This would cause difficulties explaining the abundance of matter that we observe in the universe [20]. As it stands, we do have evidence of CP violation, coming from such processes as rare kaon decays [21], $\bar{K}^0 - K^0$ mixing [22, 23, 24], $\bar{B}^0 - B^0$ mixing [25, 26] and more recently in charged B decays [27]. As mentioned in the previous section, the only possible source of CP violation in the SM is through the complex phase that appears in the CKM matrix, although this source of CP violation is thought to be too small to explain the matter/antimatter asymmetry by itself. Interestingly, the third generation of quarks was originally postulated to help explain CP violation, because a two dimensional analogue of the CKM matrix has only one parameter, the Cabbibo angle θ_c and no imaginary components. An important test of the SM is to measure the CKM components and test whether their values are consistent with the CP violation we observe experimentally.

1.4 B-Physics

An area of phenomenology that is particularly important to constrain the CKM matrix, investigate CP violation and search for hints of new physics, is the b-quark sector. With a plethora of experimental data available from the dedicated B-factories of BaBar, Belle and LHCb, as well as the general purpose experiments ATLAS and CMS, it is important for theorists to be able to provide the necessary input to apply these results to test the Standard Model. The rest of this section discusses two processes that are currently being investigated as part of the RBC/UKQCD B-physics program.

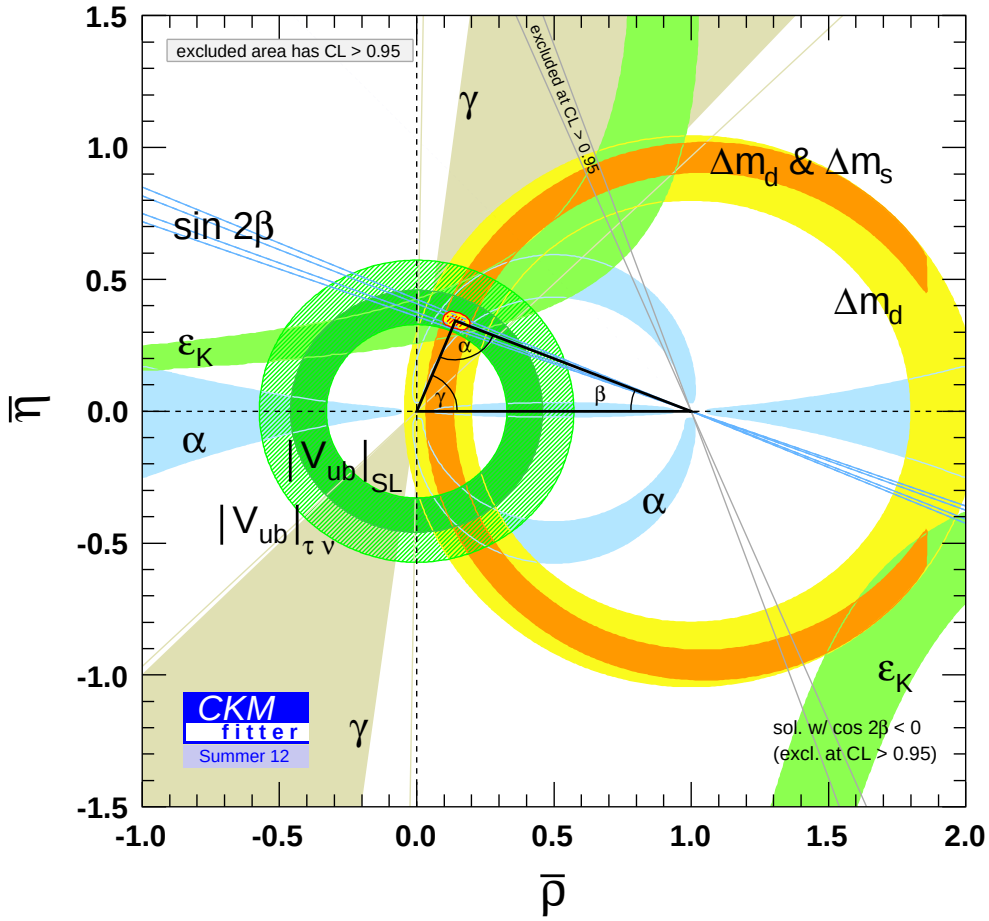

Figure 1.2: The unitarity triangle showing the constraints provided by neutral B-meson mixing (Δm_d & Δm_s) and $|V_{ub}|$ from $B \to \pi l \nu$. Plot courtesy of the CKM fitter group [1].

1.4.1 $B^0 - \bar{B}^0$ mixing

One tight constraint on the apex on CKM unitarity triangle comes from neutral B-meson mixing, which can give information on the ratio of CKM elements $|V_{ts}|^2/|V_{td}|^2$. The standard parameterisation of the experimentally accessible $B^0 - \bar{B}^0$ mass difference [28] is

$$\Delta m_q = \frac{G_F^2 m_W^2}{6\pi^2} \eta_B S_0 m_{B_q} f_{B_q}^2 B_{B_q} |V_{tq}^* V_{tb}|^2, \tag{1.26}$$

where q labels the flavour of the light quark in the B-meson. The coefficient η_B, and the Inami-Lim function S_0 [29] are both accessible using perturbation theory, whereas the combination of the decay constant and the bag parameter $f_{B_q}^2 B_{B_q}$ must be computed

non-perturbatively using Lattice QCD. By taking a ratio of mass differences

$$\frac{\Delta m_s}{\Delta m_d} = \frac{m_{B_s}}{m_{B_d}} \xi^2 \frac{|V_{ts}|^2}{|V_{td}|^2} \tag{1.27}$$

we get a particularly tight constraint on the CKM matrix elements $|V_{ts}|^2/|V_{td}|^2$ due to the cancelling of many uncertainties in the SU(3) breaking ratio

$$\xi = \frac{f_{B_s}\sqrt{B_{B_s}}}{f_{B_d}\sqrt{B_{B_d}}}. \tag{1.28}$$

One uncertainty that does not cancel, however, comes from the extrapolation to physical quark masses. Experimentally, the mass-splittings Δm_d and Δm_s are known to $\sim$1% [30], however the precision of the lattice calculations are currently only at $\sim$3% [31, 32]. A major source of uncertainties in all previous calculations arises from difficulties performing lattice simulations with physical light quark masses, and hence the chiral extrapolation from simulated masses down to the physical point. Theoretical insight from HMχPT, which we will discuss in more detail in Section 2.3, can guide this extrapolation, but lack of knowledge of the LEC of the theory introduces unwanted uncertainties. At NLO in HMχPT the running of f_{B_d} and B_{B_d} in the light quark mass is given by

$$\begin{aligned} f_{B_d} &= F\left(1 + \frac{3}{4}(1+3g_b^2)\frac{m_\pi^2}{(4\pi f_\pi)^2}\log(m_\pi^2/\mu^2)\right) + \cdots \\ B_{B_d} &= B\left(1 + \frac{3}{4}(1-3g_b^2)\frac{m_\pi^2}{(4\pi f_\pi)^2}\log(m_\pi^2/\mu^2)\right) + \cdots, \end{aligned} \tag{1.29}$$

where g_b is the leading order LEC of the theory. This is directly related to the strong coupling $g_{B^*B\pi}$, the calculation of which is the main focus of this thesis and is described in Chapter 4.

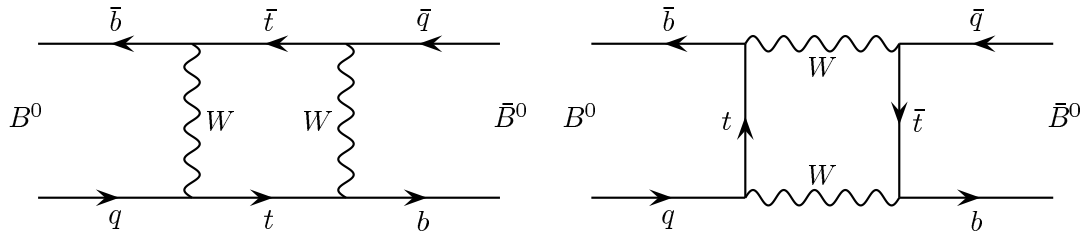

Figure 1.3: $B^0 - \bar{B}^0$ mixing proceeds mainly through box diagrams with a top quark in the loop. Being a highly suppressed next-to-leading-order process it is particularly sensitive to new physics [2].

1.4.2 $B \to \pi l \nu$

Another interesting process is the semi-leptonic decay $B \to \pi l \nu$, which can be used to determine the CKM element $|V_{ub}|$. Recently there has been a 3σ tension between $|V_{ub}|$

determined exclusively from $B \to \pi l\nu$ and inclusively from $B \to X_u l\nu$ where X_u is any hadronic final state [33]. Furthermore, determinations of $|V_{ub}|$ from the branching ratio $\mathrm{BR}(B \to \tau\nu)$ disagree with the average of the inclusive and exclusive semi-leptonic decays by more than 2σ [34]. The most recent measurements of $\mathrm{BR}(B \to \tau\nu)$ by Belle [35] do seem to be more compatible, although the errors are large.
Experimentally, the $B \to \pi l\nu$ decay is accessed by measuring the differential decay-rate, which can be parameterised in the Standard Model by

$$\frac{d\Gamma(B \to \pi l\nu)}{dq^2} = \frac{G_F^2 |V_{ub}|^2}{192\pi^2 m_B^3} \left[(m_B^2 + m_\pi^2 - q^2)^2 - 4m_B^2 m_\pi^2\right]^{3/2} |f_+(q^2)|^2. \tag{1.30}$$

On the right-hand side of (1.30) the form-factor $|f_+(q^2)|^2$ has to be calculated using Lattice QCD to be able to access the CKM element $|V_{ub}|^2$. Currently work is in progress within the RBC/UKQCD collaboration to calculate the form-factor $|f_+(q^2)|^2$ [36]. This will require chiral extrapolations, guided by HMχPT, that also rely on knowledge of the coupling $g_{B^*B\pi}$.

Chapter 2

Effective Field Theories

The Standard Model is an incredibly complex theory, which in principle is capable of explaining all natural phenomena short of gravity. However, the full theory is not always the correct tool for the job. In principle you could predict the weather using quantum mechanics, but you would be a fool to try. A classical approach would be more relevant on the scale of the atmosphere. Similarly, there are certain regimes where a simplified field theory is more applicable than the full SM. Constructing an effective field theory (EFT) begins with choosing the correct variables to describe the problem at hand. A more rigorous statement would be that the irrelevant degrees of freedom are integrated out of the problem, in the sense of Wilson's picture of renormalisation [37, 38], leaving their effect present in the couplings of the remaining terms. The symmetries of the EFT constrain which terms can be present, hopefully leaving only a small number of relevant interactions. The relevant couplings are the unknowns of the theory, and need to be found by experiment or matched to theory at a different scale. A sensible EFT has a small number of unknowns that when determined allow a large number of predictions. A final requirement of a successful EFT is some scheme to order the terms by relevance, allowing the approximation that the theory inherently introduces to be controlled systematically. For chiral perturbation theory, which I discuss in Section 2.1, the terms are ordered in powers of momentum. For heavy meson chiral perturbation theory there is a further expansion in inverse powers of the heavy quark mass.
This section aims to introduce heavy meson chiral perturbation theory (HMχPT) which deals with the low energy interactions of light pseudo-scalar and heavy-light mesons. To tackle this goal first I introduce Chiral Perturbation theory, which by itself is highly useful, and a particularly important tool in the field of lattice QCD. Finally, in Section 2.4, I provide a brief overview of the Symanzik improvement program. This is an effective field theory based approach to improve the continuum limit of lattice QCD that will prove useful when discussing systematic uncertainties in Chapter 4. The derivations in this chapter largely follow the reviews and lecture notes in the following references [39, 40, 41, 42, 43].

2.1 Chiral Perturbation Theory

The Lagrangian of QCD can be decomposed into left and right-handed quark fields that in the absence of a mass term decouple into independent fields.

$$\mathcal{L}_{QCD} = \bar{q}_R \not{D} q_R + \bar{q}_L \not{D} q_L \tag{2.1}$$

The Lagrangian then remains invariant under separate global $SU(3)$ flavour transformations. The massless approximation, as it turns out, is good. The masses of the quarks are conveniently split into two regimes,

$$\begin{array}{ccccccc} m_u, & m_d, & m_s & < \Lambda_{QCD} < & m_c, & m_b, & m_t \\ 1.7MeV & 4.1MeV & 101MeV & 400MeV & 1.5GeV & 4.5GeV & 173GeV \end{array} \tag{2.2}$$

where the three lightest quarks lie well below Λ_{QCD} and the heavy quarks lie well above. The energy scale of the interaction within mesons is of the order Λ_{QCD}, so treating the light quarks as approximately massless seems reasonable. The significance of the heavy quark masses is discussed in section 2.2. The full symmetry group in the chiral limit is $SU(3)_L \times SU(3)_R \times U(1)_L \times U(1)_R$. The $U(1)_V$ is trivially realized as baryon number conservation, and the $U(1)_A$ is only a good symmetry classically. The $U(1)_A$ is broken on quantisation of the theory, and this breaking is known as the axial anomaly. The current that corresponds to $U(1)_A$ has a non-trivial divergence that is equal to the right hand side of equation (1.6). Introducing degenerate masses for the quarks breaks the $SU(3)_L \times SU(3)_R$ symmetry to its subgroup $SU(3)_V$, and allowing for non-degenerate masses leaves only a remaining symmetry of $U(1)_V \times U(1)_V \times \cdots \times U(1)_V$ (n_f factors). Experimentally it has long been noticed that there exists an octet of light pseudoscalar mesons that can be conveniently catagorised in terms of an approximate flavour $SU(3)$.

$$\pi = \frac{1}{\sqrt{2}} \begin{pmatrix} \frac{1}{\sqrt{2}}\pi^0 + \frac{1}{\sqrt{6}}\eta & \pi^+ & K^+ \\ \pi^- & -\frac{1}{\sqrt{2}}\pi^0 + \frac{1}{\sqrt{6}}\eta & K^0 \\ K^- & \bar{K}^0 & -\frac{2}{\sqrt{6}}\eta \end{pmatrix} \sim \begin{pmatrix} u\bar{u} & u\bar{d} & u\bar{s} \\ d\bar{u} & d\bar{d} & d\bar{s} \\ s\bar{u} & s\bar{d} & s\bar{s} \end{pmatrix} \tag{2.3}$$

This octet transforms under a flavour $SU(3)$ that can clearly be identified with the diagonal subgroup $SU(3)_V$ of the full QCD symmetry group. The lightness of these mesons and the absence of parity partners with equal mass suggest that the full group $SU(3)_L \times SU(3)_R$ is not realised in nature, despite the symmetry in the Lagrangian, but is spontaneously broken to the subgroup $SU(3)_V$. The pattern of symmetry breaking allows us to interpret the lightness of the octet of pseudoscalar mesons as due to their nature as the Nambu-Goldstone bosons corresponding to the broken generators of $SU(3)_L \times SU(3)_R \to SU(3)_V$. Of course in the symmetry limit of exactly vanishing quark masses these particles would be massless, but outside of the chiral limit they are massive and referred to as pseudo-Goldstone bosons.

To make the previous statement more concrete we consider the Noether currents associated with the chiral group

$$J_V^{a\mu} = \bar{q}\gamma_\mu \frac{\lambda^a}{2} q, \quad J_A^{a\mu} = \bar{q}\gamma_5\gamma_\mu \frac{\lambda^a}{2} q \tag{2.4}$$

where the λ^a are the generators of $SU(3)$. Let us consider one of the associated charges Q and postulate the existence of an operator $\mathcal{O}$ such that

$$\langle 0|[Q, \mathcal{O}]|0\rangle \neq 0. \tag{2.5}$$

This is clearly not possible if the charge Q annihilates the vacuum. Therefore, by Goldstone's theorem [44] we know there exists a massless state $|G\rangle$ such that

$$\langle 0|J^0|G\rangle\langle G|\mathcal{O}|0\rangle \neq 0 \tag{2.6}$$

The Goldstone bosons correspond to the eight broken generators of the axial charges Q_A^a, so there must be eight Goldstone states $|G^a\rangle$. The operators must be pseudoscalars, the simplest choice being $\mathcal{O}^a = \bar{q}\gamma_5\lambda^a q$, which satisfy

$$\langle 0|[Q_A^a, \bar{q}\gamma_5\lambda^b q]|0\rangle = -\frac{1}{2}\langle 0|\bar{q}\{\lambda^a, \lambda^b\}q|0\rangle = -\frac{2}{3}\delta_{ab}\langle 0|\bar{q}q|0\rangle. \tag{2.7}$$

This defines the quark condensate that is the order parameter for Spontaneous Chiral Symmetry Breaking.

$$\langle 0|\bar{u}u|0\rangle = \langle 0|\bar{d}d|0\rangle = \langle 0|\bar{s}s|0\rangle \neq 0 \tag{2.8}$$

2.1.1 The CCWZ Formalism

We have identified that low-energy QCD has an approximate chiral symmetry that is spontaneously broken by the vacuum. In this low energy regime the relevant degrees of freedom are the Goldstone bosons. It should be possible to construct an effective theory, in terms of the Goldstone fields, that incorporates the full symmetries of the Lagrangian. Callan, Coleman, Wess and Zumino [45, 46] set out a general method for writing effective Lagrangians in the case of spontaneously broken symmetries. The NGB fields are fluctuations around the standard vacuum configuration in the space of the broken generators. We can write these fields in terms of a local transformation matrix $\Xi(x) \in G$, that acts on the vacuum. For instance,

$$\phi(x) = \Xi(x) \begin{pmatrix} 0 \\ 0 \\ \vdots \\ v \end{pmatrix}. \tag{2.9}$$

Here we note that we could also describe the same fields by $\Xi(x)h(x)$, where $h \in H$, the subgroup of G that leaves the vacuum invariant. To define the EFT solely in terms of the NGBs field (otherwise you would need to integrate out the massive fields later), CCWZ take the broken generators X^a and write

$$\Xi(x) = e^{iX^a\pi^a(x)}. \tag{2.10}$$

It is necessary that an effective Lagrangian written in terms of the $\Xi(x)$ fields is invariant under the full symmetry group G, however it is not clear how $\Xi(x)$ transforms under an arbitrary global transformation $g \in G$, as $\Xi(x)$ does not span the entire group. It is however possible to write an arbitrary transformation as

$$g\Xi(x) = \Xi'(x)h \tag{2.11}$$

where $h \in H$ is in general non-trivial and a function of both g and Ξ. This allows the definition of a global transformation rule for $\Xi(x)$ under G

$$\Xi(x) \to g\Xi(x)h^{-1}(g, \Xi(x)). \tag{2.12}$$

2.1.2 The Chiral Lagrangian

Applying the CCZW formalism to QCD we pick as the broken generators $X^a = T^a_L - T^a_R$. A general $SU(3)_L \times SU(3)_R$ transformation can be written in block diagonal form

$$g = \begin{bmatrix} L & 0 \\ 0 & R \end{bmatrix} \tag{2.13}$$

and then a transformation h from the subgroup $SU(3)_V$ is diagonal

$$h = \begin{bmatrix} U & 0 \\ 0 & U \end{bmatrix} \tag{2.14}$$

The $\Xi(x)$ field using the definition above is given by

$$\Xi(x) = \exp i \begin{bmatrix} T^a\pi^a(x) & 0 \\ 0 & -T^a\pi^a(x) \end{bmatrix} = \begin{bmatrix} \xi(x) & 0 \\ 0 & \xi^\dagger(x) \end{bmatrix} \tag{2.15}$$

where

$$\xi(x) = e^{iT^a\pi^a(x)} \tag{2.16}$$

The transformation rule for Ξ, using the formalism of the previous section is

$$\begin{bmatrix} \xi(x) & 0 \\ 0 & \xi^\dagger(x) \end{bmatrix} \to \begin{bmatrix} L & 0 \\ 0 & R \end{bmatrix} \begin{bmatrix} \xi(x) & 0 \\ 0 & \xi^\dagger(x) \end{bmatrix} \begin{bmatrix} U^{-1} & 0 \\ 0 & U^{-1} \end{bmatrix}, \tag{2.17}$$

and hence,

$$\xi^\dagger(x) \to R\xi^\dagger U^{-1}(x) \tag{2.18}$$

$$\xi(x) \to L\xi U^{-1}(x) = U(x)\xi(x)R^\dagger \tag{2.19}$$

A further simplification can be made by choosing another basis, where we take

$$\Sigma(x) = \xi^2(x). \tag{2.20}$$

and then the transformation law reduces to the purely global form

$$\Sigma(x) \to L\Sigma(x)R^\dagger. \tag{2.21}$$

To give the boson field the canonical mass dimension of a scalar field it is conventional to write

$$\Sigma(x) = e^{2i\boldsymbol{\pi}/f}, \tag{2.22}$$

where f can be identified with the pion decay constant, and $\boldsymbol{\pi} = T^a\pi^a$ has the form given in equation 2.3. To write the most general Lagrangian invariant under the chiral symmetry we first consider terms like $\mathrm{Tr}\Sigma\Sigma^\dagger$. These are invariant under the chiral group, but $\Sigma\Sigma^\dagger = 1$. This means the Lagrangian would be independent of π. Instead consider terms like $\partial_\mu\Sigma\partial^\mu\Sigma^\dagger$, in this case the Lagrangian is independent of π when π is constant, corresponding to a configuration equivalent to the vacuum. The NGBs will be derivatively coupled meaning interactions will vanish as $p \to 0$. The most most general Lagrangian, to leading order is

$$\mathcal{L}^{(2)} = \frac{f^2}{4}\mathrm{Tr}\left[\partial_\mu\Sigma\partial^\mu\Sigma^\dagger\right]. \tag{2.23}$$

where the prefactor is to give the correct normalisation of the standard kinetic term.

$$\mathcal{L}^{(2)} = \mathrm{Tr}\partial_\mu\pi\partial^\mu\pi + \frac{1}{3f^2}\mathrm{Tr}[\pi, \partial_\mu\pi]^2 + \cdots \tag{2.24}$$

From this Lagrangian it is possible to determine all $\pi - \pi$ scattering amplitudes to order p^2 in terms of a single LEC f.

2.1.3 Quark Masses

The non-zero quark masses of QCD explicitly break chiral symmetry. This can be accounted for in the chiral Lagrangian if we consider a mass term that itself transforms under $SU(3)_L \times SU(3)_R$, such that QCD would still be invariant.

$$M \to LMR^\dagger \tag{2.25}$$

where

$$M = \begin{bmatrix} m_u & 0 & 0 \\ 0 & m_d & 0 \\ 0 & 0 & m_s \end{bmatrix}. \tag{2.26}$$

With this definition we construct the most general Lagrangian with the requisite symmetry properties. To lowest order the symmetry breaking term is

$$\mathcal{L}_{sb}^{(2)} = \frac{f^2 B_0}{2} \mathrm{Tr}[M\Sigma^\dagger + \Sigma M^\dagger]. \tag{2.27}$$

where B_0 is a new LEC. This term breaks the degeneracy of the vacuum by picking out a particular direction in Σ. Expanding the trace in 2.27, gives to first order a prediction for the NGB masses due to the explicit symmetry breaking of quark masses.

$$M_{\pi^\pm}^2 = B_0(m_u + m_d) + \cdots \tag{2.28}$$

$$M_{K^\pm}^2 = B_0(m_u + m_s) + \cdots \tag{2.29}$$

$$M_{K_0,\bar{K}_0}^2 = B_0(m_d + m_s) + \cdots \tag{2.30}$$

2.2 Heavy Quark Effective Theory

A heavy-light meson consists of one heavy quark, one light quark and any amount of gluons and virtual quarks. As we have previously mentioned the mass of the heavy quarks (c, b, t) are much greater than the typical interaction scale of QCD inside a meson. It is therefore not unreasonable to consider the heavy quark to be approximately on-shell, meaning in its rest frame it is just a static source of gluons. For interactions of $\mathcal{O}(\Lambda_{QCD})$ the heavy quark's momentum only changes by Λ_{QCD}/m_Q, therefore in the $m_Q \to \infty$ limit velocity is conserved. The heavy quark just sits there and doesn't affect the dynamics of the problem. The system can then be completely described by the quantum numbers of the light degrees of freedom. The interactions inside the heavy-light meson are $\sim \Lambda_{QCD}$, meaning the amount by which the heavy quark is off-shell is of this order. Calling this quantity k_μ, the heavy quark's momentum is

$$P_\mu = m_Q v_\mu + k_\mu. \tag{2.31}$$

For a quark with Lagrangian $\mathcal{L}_{QCD} = \bar{Q}(i\not{D} - m_Q)Q$, and tree level propagator

$$S = \frac{i}{\not{P} - m_Q}, \tag{2.32}$$

we can insert Equation (2.31) and expand in $1/m_Q$.

$$S = i\left(\frac{1+\not{v}}{2}\right)\frac{1}{v\cdot k} + \mathcal{O}\left(\frac{\Lambda_{QCD}}{m_Q}\right) \tag{2.33}$$

This propagator is reproduced, to leading order, by the Lagrangian

$$\mathcal{L}_{LO}^{HQET} = \bar{Q}_v(iv \cdot D)Q_v, \tag{2.34}$$

where the heavy quark field Q_v obeys

$$\left(\frac{1+\not{v}}{2}\right) Q_v = Q_v. \tag{2.35}$$

This is the leading order Heavy Quark Effective Theory (HQET) Lagrangian. We notice that there is no mass term and no gamma-matrices, corresponding to a spin-flavour symmetry. A more rigorous derivation is needed to obtain the higher order spin and mass dependent terms that are suppressed by powers of the heavy quark mass.

We can write the total angular momentum of the heavy meson as

$$\mathbf{J} = \mathbf{L} + \mathbf{S} \tag{2.36}$$

where $\mathbf{L}$ is the angular momentum of the light degrees of freedom and $\mathbf{S}$ is the angular momentum of the heavy quark. Considering a state with $l = 1/2$, we can have $J = 0$ and $J = 1$, corresponding to a degenerate pseudoscalar and vector meson. This could be the B and B^* or the D and D^*. We can see already how powerful this picture is by considering the mass splitting between the vector and pseudoscalar B-mesons, and the equivalents in the charm sector

$$\frac{m_{D^*} - m_D}{m_D} \approx 8\% \qquad \frac{m_{B^*} - m_B}{m_B} \approx 0.9\%. \tag{2.37}$$

Clearly, for the heavy quarks the splitting is smaller. We expect the splittings to be of of the form $m_{P^*} - m_P \approx a/m_Q$. This allows us to make a better prediction $m_{D^*}^2 - m_D^2 \approx m_{B^*}^2 - m_D^2$, which agrees very well with the experimental data [30]

$$m_{D^*}^2 - m_D^2 = 0.55\text{GeV}^2 \qquad m_{B^*}^2 - m_B^2 = 0.48\text{GeV}^2. \tag{2.38}$$

It is conventional to package these two mesons together into a single field

$$H = \frac{1+\not{v}}{2}\left[B_\mu^* \gamma^\mu - B\gamma_5\right], \tag{2.39}$$

where the B and B^* are column vectors with entries corresponding to $b\bar{u}$, $b\bar{d}$, $b\bar{s}$. The heavy meson fields transform under the spin S_Q and flavour $SU(3)$ symmetry U as

$$H \to S_Q H U^\dagger \tag{2.40}$$

With these ingredients in place we can combine the light pseudoscalar mesons of chiral perturbation theory with the heavy-light mesons of HQET.

2.3 Heavy Meson Chiral Perturbation Theory

The most general Lagrangian we can write in terms of the H fields and the light pseudoscalars, that obeys both the light-flavour symmetries and the symmetries of HQET, is

$$\mathcal{L}_{HM\chi PT} = \mathrm{Tr}\left[\bar{H}(iv\cdot D)H\right] + g\mathrm{Tr}\left[\bar{H}H\gamma^\mu\gamma_5\mathcal{A}_\mu\right] \tag{2.41}$$

combined with the light pseudo-scalar kinetic and mass terms (2.23), (2.27).

$$D^\mu H = \partial^\mu H + \mathcal{V}^\mu H \tag{2.42}$$

defines a covariant derivative for $SU(3)$ flavour to ensure that the H field transforms correctly under the unbroken symmetry group.

$$\begin{aligned}\mathcal{A}^\mu &= \frac{i}{2}\left(\xi\partial^\mu\xi^\dagger - \xi^\dagger\partial^\mu\xi\right)\\ \mathcal{V}^\mu &= \frac{i}{2}\left(\xi\partial^\mu\xi^\dagger + \xi^\dagger\partial^\mu\xi\right)\end{aligned} \tag{2.43}$$

At this order there is a single LEC g that governs the strength of the interactions. If we take the H fields to be made up of B and B^* mesons, as in Equation (2.39), then we will call the coupling g_b. For a theory with D mesons everything is the same except we make the replacement $g_b \to g_c$.

2.3.1 $g_{B^*B\pi}$

The $B^*B\pi$ coupling is defined by the strong matrix element [47]

$$\langle B(p)\pi(q)|B^*(p',\lambda)\rangle = -g_{B^*B\pi}(q^2)q\cdot\epsilon^\lambda(p), \tag{2.44}$$

where λ labels the polarisation of the vector meson. This is an unphysical matrix element, as the decay is forbidden by lack of phase space. However, the equivalent quantity in the charm sector is allowed, and has been measured by the CLEO experiment [48]

$$g_{D^*D\pi} = 17.9 \pm 0.3 \pm 1.9 \tag{2.45}$$

The same matrix element, at leading order in HMχPT is given by

$$\langle B(p)\pi(q)|B^*(p',\lambda)\rangle = -g_b\frac{2m_B}{f_\pi}q\cdot\epsilon^\lambda(p). \tag{2.46}$$

leading to the relation

$$g_{B^*B\pi} = \frac{2m_B}{f_\pi}g_b \tag{2.47}$$

This allows the low energy constant to be accessed directly through a strong decay amplitude.

2.4 Symanzik Improvement Program

The Symanzik improvement program [49, 50] is a technique to systematically improve the continuum limit of a lattice gauge theory using a continuum effective theory. Lattice QCD will be introduced in Chapter 3, but for the following discussion it is sufficient to consider Lattice QCD as QCD with some ultra-violet cut-off a. Symanzik's idea was to demand equality between the lattice theory and a renormalised continuum effective theory.

$$\mathcal{L}_{\text{Lat}} \doteq \mathcal{L}_{\text{Sym}} \tag{2.48}$$

The dotted equality means that both sides produce the same physics. The central idea is that the Symanzik side of the equality can be written as QCD plus higher order ($\dim\mathcal{O} > 4$) operators.

$$\mathcal{L}_{\text{Sym}} = \mathcal{L}_{QCD} + \sum_{\mathcal{O}} a^{\dim\mathcal{O}-4} C_{\mathcal{O}}(g^2; ma; \mu a)\mathcal{O}_R(\mu) \tag{2.49}$$

The dimensionless coefficients $C_{\mathcal{O}}$ contain all dependence on short-distances and the operators $\mathcal{O}_R$ encode the long-distance physics. The coefficients depend on all couplings of the lattice action, and for fixed values (of g^2, ma etc) they encode information about the cut-off effects of the lattice theory. The application of the Symanzik theory is to subtract (discretised versions of) these higher-order terms from the lattice action to improve the continuum limit. In theory, this can be performed order-by-order, thus the technique is known as Symanzik improvement program.
It is possible to make field redefinitions to $\mathcal{L}_{QCD}$ that will not change on-shell matrix elements. For instance

$$q \to q + a^{\dim X}\epsilon_X X q, \quad \bar{q} \to \bar{q} + a^{\dim X}\bar{\epsilon}_X \bar{q} X \tag{2.50}$$

for any gauge covariant operator X and any choice of the parameters ϵ_X and $\bar{\epsilon}_X$. At each order these substitutions will change the higher order terms. Inserting (2.50) into $\mathcal{L}_{QCD}$ creates new terms like

$$\sum_X a^{\dim X}\left[\bar{\epsilon}_X \bar{q} X(\not{D} + m_q)q + \epsilon_X \bar{q}(-\overleftarrow{\not{D}} + m_q)Xq\right], \tag{2.51}$$

which just amount to a change of the coefficients of higher order terms. The field redefinitions are arbitrary and do not affect the physics, meaning the terms like (2.51) must be redundant. At dimension five there are five possible operators that obey the symmetries of QCD (see 1.1.1), of which only two are linearly independent or cannot be directly absorbed by redefinitions of the couplings,

$$\mathcal{O}_5 = i\bar{q}\sigma_{\mu\nu}F^{\mu\nu}q, \quad \mathcal{O}_5' = 2\bar{q}D^2 q. \tag{2.52}$$

The second of these can be rewritten as

$$\mathcal{O}' = 2\bar{q}\not{D}(\not{D} + m)q - 2m\bar{q}\not{D}q, \tag{2.53}$$

a redundant part and a piece that can be absorbed into the field normalisation. Therefore at dimension five there is only one additional operator to consider, the so called Sheikholeslami-Wohlert term [51] $\mathcal{O}_5 = i\bar{q}\sigma_{\mu\nu}F^{\mu\nu}q$. This tells us that by subtracting $\mathcal{O}_5$ with the correct coefficient from our lattice theory we have equality with QCD up to terms proportional to a^2 [1] It is important to note that $\mathcal{O}_5$ is a continuum operator, to improve $\mathcal{L}_{\text{Lat}}$ it is necessary to subtract a discretised version of the operator. For a specific discretisation of the Sheikholeslami-Wohlert term see (3.47). Improving the action is all that is necessary to improve on-shell quantities [52], however for other quantities it is also necessary to improve the lattice operators that we take expectation values of. In this work, however, we will only be calculating matrix elements of domain wall fermion light quark operators (see Section 3.3.2 and 4.5) and as such we will not require any explicit operator improvement. Various approaches have been used to tune the coefficient of the lattice Sheikholeslami-Wohlert term, including perturbation theory [51, 53] and so called *tadpole improvement* [54]. For the work in this thesis a lattice action with a non-perturbatively tuned Sheikholeslami-Wohlert term is used. This is discussed in section 3.4.4.

[1] In lattice QCD a will be a short-distance that we will aim to take to zero.

Chapter 3

Lattice QCD

Lattice Quantum Chromodynamics (LQCD) is the Euclidean space, discrete, finite volume version of QCD. By putting QCD on a hyper-cubic lattice we regularise the theory and at the same time make it amenable to numerical simulations. In the low-energy regime of QCD, which includes most interesting hadronic phenomena, the QCD coupling is large and perturbation theory breaks down. This is where LQCD becomes invaluable. This chapter will introduce the QCD path integral on which the LQCD is based, followed by a description of the various lattice actions used in this work. Finally, the chapter will finish with a discussion of the numerical techniques necessary to make real lattice computations.

3.1 Path Integrals

Observables in QCD can be calculated as vacuum expectation values of quark and gluon operators using a path integral approach.

$$\langle \mathcal{O}(\bar{\psi}, \psi, A) \rangle = \frac{1}{Z} \int D[\bar{\psi}] D[\psi] D[A] \; \mathcal{O}(\bar{\psi}, \psi, A) \; e^{-S_g[A] - S_f[\bar{\psi}, \psi, A]} \tag{3.1}$$

$$Z = \int D[\bar{\psi}] D[\psi] D[A] \; e^{-S_g[A] - S_f[\bar{\psi}, \psi, A]} \tag{3.2}$$

In the equation above the action has been separated into two parts, a purely gauge part and the fermion action. In the above all flavour indices have been suppressed. The fermion fields are represented by anti-commuting Grassman numbers which would prove difficult to represent on a computer, however the fermionic part of the action is quadratic in the quark fields, meaning we can use the standard Gaussian formula to integrate out the fermions.

$$Z = \int D[\bar{\psi}] D[\psi] D[A] \; e^{-S_g[A] - \bar{\psi} D(A) \psi} = \int D[A] \; \det[D(A)] e^{-S_g[A]} \tag{3.3}$$

In the above expression the fermion action is written as some Dirac operator which is dependent on the gauge fields through a covariant derivative. Historically lattice calculations were carried out setting the fermion determinant to unity, known as the quenched approximation. This corresponds to neglecting sea-quark loop effects. Current simulations use fully dynamical sea quarks (i.e. calculating the determinant) and we see the old approximation was surprisingly good, nonetheless it was an uncontrolled approximation and needs to be removed. If the determinant is positive definite, which it will be in the case of two degenerate flavours, we can treat the product of the determinant and the exponential as a probability weight. Once space and time have been discretised, and the integral rendered finite dimensional, we can use importance sampling to approximate the integral. The quark fields under the path integral can be Wick contracted to be re-expressed as a product of fermion propagators.

$$S(A;x,y) = D^{-1}(A;x,y) \tag{3.4}$$

The propagators themselves are functions of the gauge fields. If we can correctly sample the space of all gauge fields and calculate the propagators on each field configuration the integral can be approximated by a sum over N field configurations

$$\langle \mathcal{O}(\bar{\psi},\psi,A)\rangle = \sum_{i}^{N} Tr\left[S(A;x,y)S(A;y,z)\cdots\right] + \mathcal{O}\left(\frac{1}{\sqrt{N}}\right), \tag{3.5}$$

where the trace runs over spin and colour indices. With an increasing number of samples this will converge to the correct correlation function, and due to the central limit theorem the sample mean will belong to a Gaussian distribution. Due to the exponential weight factor (3.3), the distribution is narrow and only a small part of the integration space makes the dominant contribution to the integral. To generate the sample gauge configurations a Markov chain is used. This is a random walk through configuration space that is constructed such that at equilibrium it is the desired distribution. A sufficient condition to acheive the desired distribution is to demand that the transition probability from state U to U', $T(U'|U)$ obeys

$$T(U'|U)P(U) = T(U|U')P(U'), \tag{3.6}$$

which is known as the detailed balance equation. The transition probability must also be postive for all pairs of U and U' with $\sum_{U'} T(U'|U) = 1$. It is usually necessary to run the Markov process for a large number of steps before equilibrium is reached, this is known as thermalisation. Furthermore, each trajectory (step in the chain) is closely related to the last. This is known as auto-correlation. Usually measurements are only carried out on trajectories that are well separated, hence reducing auto-correlation, however this must still be taken into account during the data analysis (see Section 3.5.3). There are a number of algorithms available to generate the Markov chain, such as Heat Bath [55], Over-relaxation [56] and Hybrid Monte-Carlo (HMC) [57]. The configurations used in

this thesis were generated with the Rational Hybrid Monte-Carlo algorithm (RHMC) [58]. This is an improved version of HMC that allows simulations with an odd number of sea-quarks, where the product of fermion determinants is not automatically positive definite. The process of generating gauge configurations is the most expensive part of a lattice QCD calculation. Typically, the configurations are generated as a collaborative effort and reused in a number of different physics analyses.

Next we shall discuss how to put the theory onto a lattice. The two most important criteria any discretised gauge theory must meet are gauge invariance and a well defined continuum limit. Therefore, first we will consider how to introduce a discretised covariant derivative. If we place the fermion fields at the lattice vertices the obvious choice for a derivative is a symmetric difference

$$\partial_\mu \psi(x) \to \frac{1}{2a}\left(\psi(n+\hat{\mu}) - \psi(n-\hat{\mu})\right), \tag{3.7}$$

where $\hat{\mu}$ is a unit vector that points in either of the four lattice dimensions. Using this definition we can make a first attempt at a massless free fermion action.

$$S_F^0[\bar{\psi},\psi] = a^4 \sum_{n\in\Lambda} \bar{\psi}(n) \left(\sum_{\mu=1}^{4} \gamma_\mu \frac{\psi(n+\hat{\mu}) - \psi(n-\hat{\mu})}{2a} \right) \tag{3.8}$$

Here μ runs over the four dimensions of the lattice, a is the lattice spacing and Λ represents the spatial extent of the lattice. To maintain gauge invariance we have to make sure the action is invariant under the unitary local transformations

$$\psi(n) \to \psi' = \Omega(n)\psi(n), \quad \bar{\psi}(n) \to \bar{\psi}' = \bar{\psi}(n)\Omega(n)^\dagger. \tag{3.9}$$

where $\Omega(n)$ is an $SU(3)$ gauge matrix at site n. Clearly, terms with non-matching lattice indices will not be invariant under these transformations. For instance,

$$\bar{\psi}(n)\psi(n-\hat{\mu}) \to \bar{\psi}(n)\Omega(n)^\dagger\Omega(n-\hat{\mu})\psi(n-\hat{\mu}) \tag{3.10}$$

To restore gauge invariance we introduce fields $U_\mu(n)$ which are group elements of $SU(3)$ and live on the links. The index μ refers to it being the link between n and its nearest neighbour in the μ-direction, at position $n + a\hat{\mu}$. We also use the relation $U_{-\mu}(n) \equiv U_\mu(n-\hat{\mu})$. These *gauge links* have the transformation properties

$$U_\mu(n) \to U'_\mu = \Omega(n)U_\mu(n)\Omega(n+\hat{\mu})^\dagger \tag{3.11}$$

With this ingredient in place, we can rewrite Equation 3.8 in a gauge invariant form

$$S_F^0[\bar{\psi},\psi] = a^4 \sum_{n\in\Lambda} \bar{\psi}(n) \left(\sum_{\mu=1}^{4} \gamma_\mu \frac{U_\mu(n)\psi(n+\hat{\mu}) - U_{-\mu}(n)\psi(n-\hat{\mu})}{2a} \right). \tag{3.12}$$

The link variables are related to the continuum gauge fields through the expression

$$U_\mu(n) = \exp(iaA_\mu(n)), \tag{3.13}$$

meaning that elements of the group $SU(3)$, rather than generators, become the fundamental variables that we deal with in the lattice formulation and the gauge links act as parallel transporters for the gauge transformations.

3.2 Gauge Actions

To construct an action out of the link variables we must identify how to make gauge invariant objects. Any transformation matrices will cancel from within a string of gauge links, but the matrices at either end will not. Therefore, we consider closed loops of gauge links, the simplest of which is the plaquette. This is a one-by-one square of gauge links

$$U_{\mu\nu} = U_\mu(n)U_\nu(n+\hat{\mu})U_{-\mu}(n+\hat{\mu}+\hat{\nu})U_{-\nu}(n+\hat{\nu}), \tag{3.14}$$

the trace of which is invariant under a gauge transformation. From this we have the necessary ingredients to write down Wilson's gauge action [59].

$$S_g[U] = \frac{2}{g^2}\sum_{n\in\Lambda}\sum_{\mu<\nu}\text{Re tr}\left[\mathbb{1} - U_{\mu\nu}(n)\right] \tag{3.15}$$

The continuum limit of Equation 3.15 can be found by inserting the definition of the gauge link from Equation 3.13, applying the Baker-Campbell-Hausdorff formula and Taylor expanding for small a.

$$S_g[U] = \frac{a^4}{2g^2}\sum_{n\in\Lambda}\sum_{\mu<\nu}\text{tr}\left[F_{\mu\nu}(n)^2 + \mathcal{O}(a^2)\right] \tag{3.16}$$

3.2.1 Improved Gauge Actions

We have shown that the Wilson gauge action reproduces the continuum gauge action to $\mathcal{O}(a^2)$, but we could also add higher dimensional operators to the lattice action that would have no effect in the continuum, but possibly cancel higher powers of a. This is the basis for *improvement programs*, which we discussed more thoroughly in Section 2.4. Any additional operators must be gauge invariant, so the obvious choices are larger loops of gauge links, such as the one-by-two rectangle. This lattice operator can be added to the Wilson gauge action,

$$S_g[U]^{improved} = \frac{2}{g^2}\sum_{n\in\Lambda}\sum_{\mu<\nu}\text{Re tr}\left[\mathbb{1} - c_0U_{\mu\nu}^{plaq}(n) - c_1U_{\mu\nu}^{rect}\right], \tag{3.17}$$

with the restriction that $c_0 + 8c_1 = 1$ to ensure that $F_{\mu\nu}F_{\mu\nu}$ is normalised to unity. A variety of techniques, both perturbative and non perturbative, have been employed to tune the improvement coefficients, such as:

Lüscher-Weiz [60, 61, 52]	$c_1 = -1/12$
Iwasaki [62, 63]	$c_1 = -0.331$
DBW2 [64]	$c_1 = 1.4069.$

As well as improving the continuum limit, it has been shown that these improved actions can improve the chiral properties of simulations [65] when used in conjunction with domain wall fermions (see section 3.3.2). The work described in this thesis is carried out on configurations produced by the RBC/UKQCD collaboration using the Iwasaki gauge action.

3.3 Fermion Actions

Starting from Equation 3.12 our first attempt at a fermion action is

$$S_F^0[\bar{\psi},\psi] = a^4 \sum_{n\in\Lambda} \bar{\psi}(n) \left(\sum_{\mu=1}^{4} \gamma_\mu \frac{U_\mu(n)\psi(n+\hat{\mu}) - U_{-\mu}(n)\psi(n-\hat{\mu})}{2a} + m\psi(n) \right). \quad (3.18)$$

To see where this fails we calculate the propagator, with trivial gauge fields, by performing a Fourier transform on the lattice Dirac operator and finding its inverse.

$$S(p) = \frac{m - ia^{-1}\sum_\mu \gamma_\mu \sin(p_\mu a)}{m^2 + a^{-2}\sum_\mu \sin(p_\mu a)^2} \quad (3.19)$$

We can easily check that this has the correct continuum limit. Setting the mass to zero we retrieve the continuum propagator.

$$S(p)|_{m=0} = \frac{-ia^{-1}\sum_\mu \gamma_\mu \sin(p_\mu a)}{a^{-2}\sum_\mu \sin(p_\mu a)^2} \overset{a\to 0}{\to} \frac{-i\sum_\mu \gamma_\mu p_\mu}{p^2} \quad (3.20)$$

The continuum propagator has a single pole at $p = (0,0,0,0)$, however, the lattice version also has poles at $ap = (\pi,0,0,0), (0,\pi,0,0), \cdots, (\pi,\pi,\pi,\pi)$. These 15 unphysical poles correspond to 15 unwanted particles known as doublers. This is clearly a problem.

3.3.1 Wilson Fermions

A sensible lattice theory of fermions will only have one pole at $ap = (0, 0, 0, 0)$, corresponding to a single physical particle. One way this can be achieved is by giving each of the doublers a large mass, of the order of the cut-off, which goes to infinity and decouples the doublers in the continuum limit. This was the approach first suggested by Wilson. In momentum space, an extra term is added to the Dirac operator

$$D(p) = m + \frac{i}{a}\sum_{\mu}\gamma_\mu \sin(p_\mu a) + \frac{1}{a}(1 - \cos(p_\mu a)), \tag{3.21}$$

and hence each doubler has a mass $m + 2/a$. The free propagator calculated from this operator is free of the unwanted modes. The Wilson term itself is a discretisation of the negative Laplacian, meaning the Wilson-Dirac operator can be written in the succinct form

$$D(n, m)^{\alpha\beta}_{ab} = \left(m + \frac{4}{a}\right)\delta_{\alpha\beta}\delta_{ab}\delta_{nm} - \frac{1}{2a}\sum_{\mu=\pm1}^{\pm4}(1 - \gamma_\mu)_{\alpha\beta}U_\mu(n)_{ab}\delta_{n+\hat{\mu},m} \tag{3.22}$$

In the above equation the Greek indices label spin, the Roman indices label colour, and the definition $\gamma_{-\mu} \equiv -\gamma_\mu$ is used. The Wilson fermion action successfully removes the doubler modes, and in the continuum limit restores all the relevant symmetries of QCD. However, at finite lattice spacing the chiral symmetry is explicitly broken by the Wilson term which acts like a mass term, even for zero quark mass. Having a lattice action that violates chiral symmetry has many disadvantages, both theoretically and practically. A chiral action eases the problem of operator mixing when renormalising composite operators, making the problem more like the continuum. Another problem concerns so called exceptional configurations. The eigenvalues of a lattice Dirac operator $D[U]$, with bare quark mass m, can be written

$$m + \lambda_i[U]. \tag{3.23}$$

In general $\lambda_i[U]$ is complex, but real negative values are possible. For small m the fluctuating values of $\lambda[U]$ can cause the eigenvalues of $D[U]$ to become very small, meaning numerical inversions become impractical. The only way around this is to use larger quark masses, often far from the physical point. This is not a problem however for chiral fermion actions for which the spectrum of the Dirac operator lies in a circle on the complex plane of radius $1/a$, centred at $m + 1/a$. This is a consequence of the Ginsparg-Wilson equation which is introduced in the next section.

3.3.2 Domain Wall Fermions

An important theorem by Neilsen and Ninomiya [66] states that a local, translation invariant, real, bilinear lattice action, cannot be simultaneously free of doublers and chirally invariant. This was how things stood until a paper by Ginsparg and Wilson [67] was rediscovered. In their now famous work they suggested a modified form of chiral symmetry. Continuum chiral symmetry can be neatly summarised by demanding that the Dirac operator anti-commutes with the fifth gamma matrix, $\{D, \gamma_5\} = 0$, which was assumed as a condition by Neilson and Ninomiya. Ginsparg and Wilson extended this expression by including a cut-off dependent term on the right-hand side.

$$D\gamma_5 + \gamma_5 D = aD\gamma_5 D \tag{3.24}$$

This equation recovers continuum chiral symmetry for $a \to 0$, and for $a \neq 0$ allows an alternative definition of the usual chiral rotations

$$\psi \to e^{i\alpha\gamma_5\left(1+\frac{a}{2}D\right)}\psi \qquad \bar{\psi} \to \bar{\psi}e^{i\alpha\left(1+\frac{a}{2}D\right)\gamma_5}. \tag{3.25}$$

The Ginsparg-Wilson equation can be solved exactly by the overlap operator [68, 69, 70]

$$D_{ov} = \frac{1}{a}\left(1 + \gamma_5 \text{sign}[\gamma_5 A]\right), \tag{3.26}$$

where A is a suitable 'Kernel' Dirac operator. In practice the Wilson operator is usually chosen. Unfortunately, although the overlap operator possesses exact chiral symmetry, numerically it is extremely taxing to simulate, due to the matrix sign function. Chiral fermion actions did not gain any traction until Kaplan's seminal 1992 paper [71]. In this he showed how massive interacting fermions in $2n + 1$ dimensions can be used to simulate massless fermions in $2n$ dimensions. This is the origin of domain wall fermions (DWF). The standard DWF formulation introduces a finite fifth-dimension L_s, which when taken to infinity provides exact (Ginsparg-Wilson) chiral symmetry. In the modern viewpoint, the extra-dimension is merely a useful calculational tool, corresponding to an approximation of the overlap sign-function [72, 73]. It can be shown that for $L_s \to \infty$ the domain wall and overlap formulations are exactly equivalent. A further benefit of domain wall fermions, or any other chirally symmetric formulation, is that it is automatically $\mathcal{O}(a)$ improved. This can be most easily seen by considering the effect of adding an $\mathcal{O}(a)$ improving term, such as a lattice Sheikholeslami-Wohlert term (Section 2.4). Such an operator would no longer obey the Ginsparg-Wilson equation (3.24) so we must conclude that chiral actions are already improved to this order.

3.3.2.1 Continuum Formulation

The basis of Kaplan's idea was to write down a 5d Dirac operator, with a mass-term dependent on the extra dimension, s.

$$D_5 = \not{\partial} + \gamma_5 \partial_s + M(s) \tag{3.27}$$

The exact form of the mass term is unimportant, so long as $M(\infty) = M$, $M(0) = 0$ and $M(-\infty) = -M$. A step function is a convenient choice. A generic solution to the equations of motion can be written as

$$\psi = \phi(s) u(p) e^{i\vec{p}.\vec{x}}. \tag{3.28}$$

A specific solution is the massless case where $i\not{p} = 0$ and the spinor is a helicity eigenstate $\gamma_5 u(p) = \pm u(p)$.

$$\left[\gamma_5 \partial_s + M(s)\right] \phi_\pm(s) u_\pm = 0 \tag{3.29}$$

This gives two possible solutions for the s-dependent function.

$$\phi_\pm(s) = \exp\left[\mp \int_0^s M(s')ds'\right] \tag{3.30}$$

However, if we are to insist on only normalisable solutions, then $\phi_-(s)$ must be discarded. The interpretation is that a single massless chiral mode is bound to the domain wall, with a wave function falling off exponentially in the s-direction. If the opposite chirality is required all that is necessary is to interchange $m(s) \to -m(s)$. Furthermore, if the s-coordinate is made finite, for instance $0 < s < N_s$ with $M(s) = M$ Dirichlet boundary conditions, opposite chiral modes are found on the two domain walls.

3.3.2.2 Discretisation

To use this technology in lattice simulations it is necessary to discretise the operator D_5. A naive approach, as with regular fermion actions, falls foul of the doubling problem. To

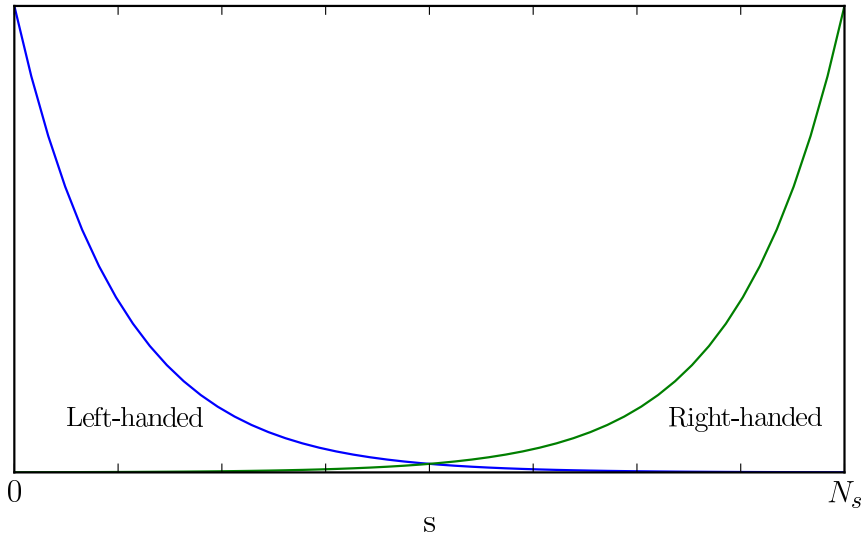

Figure 3.1: Chiral modes bound to the walls of the fifth dimension.

side-step these difficulties a five-dimensional Wilson term is introduced from the outset.

$$\begin{aligned} D_{DWF}(n,m;s,t) =& \frac{1}{2}\sum_{\mu=1}^{4}\gamma_\mu\left[U_\mu(n)\delta_{n,m+\mu} - U_\mu^\dagger(n)\delta_{n,m-\mu}\right]\delta_{s,t} + M_0\delta_{n,m}\delta_{s,t} \\ &- \sum_{\mu=1}^{4}\frac{1}{2}\left[U_\mu(n)\delta_{n,m+\mu} - 2\delta_{n,m} + U_\mu^\dagger(n)\delta_{n,m-\mu}\right]\delta_{s,t} \\ &+ \frac{1}{2}\gamma_5\left[\delta_{s,t+1} - \delta_{s,t-1}\right]\delta_{n,m} \\ &- \frac{1}{2}\left[\delta_{s,t+1} - 2\delta_{s,t} + \delta_{s,t-1}\right]\delta_{n,m} \end{aligned} \tag{3.31}$$

For simplicity we set the lattice spacing to unity. After performing a Fourier transform on the regular 4-coordinates the operator can be rewritten as

$$D_{DWF}(p;s,t) = i\not{p}\delta_{s,t} + \left[1 + M_0 - \sum_{\mu=1}^{4}(1-\cos p_\mu)\right]\delta_{s,t} - P_+\delta_{s,t-1} - P_-\delta_{s,t+1} \tag{3.32}$$

$$\not{p} = \sum_{\mu=1}^{4}\gamma_\mu \sin p_\mu. \tag{3.33}$$

Here $P_\pm = \frac{1}{2}(1\pm\gamma_5)$ are the usual chiral projectors. Taking the viewpoint that the extra dimension is simply a flavour label, the action can be further simplified by writing it in terms of a non-diagonal, p-dependent mass matrix.

$$S = \sum_{s,t}\sum_{p}\bar{\psi}_s(-p)\left[i\not{p}\delta_{st} + P_-M_{s,t} + P_+M_{s,t}^\dagger\right]\psi_t(p) \tag{3.34}$$

$$M_{s,t} = \begin{bmatrix} b(p) & -1 & 0 & \cdots & 0 \\ 0 & b(p) & -1 & 0 & \vdots \\ \vdots & 0 & b(p) & -1 & 0 \\ \vdots & \ddots & 0 & b(p) & -1 \\ m & \cdots & \cdots & 0 & b(p) \end{bmatrix} \tag{3.35}$$

$$b(p) = 1 + M - \sum_{\mu=1}^{4} (1 - \cos p_\mu) \tag{3.36}$$

To give the quarks mass we add a parameter m in the bottom left-hand corner of (3.35). We now expect to find light modes bound to the oppposite walls with heavy modes living in the middle of the flavour space. To investigate this we can calculate the eigenvectors and eigenvalues of the mass matrix. Following [74, 75] we look at the eigenvectors of $(MM^\dagger)_{s,t}$ in the zero momentum limit, where $b_0 = 1 + M$.

$$(MM^\dagger)_{s,t} = \begin{bmatrix} b_0^2 + 1 & -b_0 & 0 & \cdots & bm \\ -b_0 & b_0^2 + 1 & -b_0 & 0 & \vdots \\ 0 & -b_0 & b_0^2 + 1 & -b_0 & 0 \\ \vdots & 0 & -b_0 & b_0^2 + 1 & -b_0 \\ bm & \cdots & 0 & -b_0 & b_0^2 + m^2 \end{bmatrix} \tag{3.37}$$

From the eigenvalue equation we find three constraints

$$(b_0^2 + 1 - \lambda_i^2)\phi_1^- - b_0\phi_2^- + b_0 m\phi_{N_s}^- = 0 \tag{3.38}$$

$$-b_0\phi_{s-1}^- + (b_0^2 + 1 - \lambda_i^2)\phi_s^- - b_0\phi_{s+1}^- = 0 \tag{3.39}$$

$$b_0 m\phi_1^- - b_0\phi_{N_s-1}^- + (b_0^2 - m^2 - \lambda_i^2)\phi_{N_s}^- = 0 \tag{3.40}$$

and similarly for the ϕ^+. These equations can be solved using the ansatz $\phi = Ae^{\alpha s} + Be^{-\alpha s}$, and for $0 < b_0 < 1$

$$\cosh(\alpha_i) = \frac{1 + b_0^2 - \lambda_i^2}{b_0}. \tag{3.41}$$

The lowest eigenvalue is shown in [76, 77, 74] to be

$$\begin{aligned} \lambda_1^2 &= m^2(1 - b_0)^2 + \mathcal{O}(m^4) + \mathcal{O}(b_0^{N_s}) \\ &= m^2 M^2 (2 - M)^2 + \mathcal{O}(m^4) + \mathcal{O}((1 - M)^{N_s}) \end{aligned} \tag{3.42}$$

with corresponding eigenvector

$$\phi_s^{(1)} = \sqrt{1 - b_0^2} e^{\alpha_i (s-1)} (\text{sign } b_0)^{s-1}. \tag{3.43}$$

We interperate this to mean the lightest mode is bound to the domain wall and falls of exponentially with s (with the opposite handed mode on the other boundary). Its mass

is given by λ_1 and is proportional to m, except with an additve renormalisation that falls off as $N_s \to \infty$ for $0 < M < 2$. This is refered to as the residual mass and originates from the left and right-handed modes mixing in the middle of the fifth-dimension. The rest of eigenmodes have ocillatory behaviour coming from α becoming imaginary and correspond to heavy modes living in the fifth-dimensional bulk.

$$\phi_s^{(i)} = \frac{2}{N_s} \sin\left(\frac{\pi(i-1)}{N_s}\left[N_s + 1 - s\right]\right) \quad i \neq 1 \tag{3.44}$$

To remove these modes we add an extra term to the action

$$S = \bar{\psi} D_{DWF} \psi + \bar{\phi} D_{PV} \phi. \tag{3.45}$$

These fields are pseudo-fermions, meaning they have all the same quantum numbers as the fermion fields, but are not Grassman valued. On integration of the action $\det[D_{PV}]$ appears downstairs, allowing it to be chosen such that it exactly cancels the bulk mode contribution to $\det[D_{DWF}]$. Vranas showed in [77] that a suitable choice is $D_{PV} = D_{DWF}(m = 1)$.

3.4 Heavy Quark Actions

In principle we can use any fermion action to simulate heavy quarks, however in practice there is an important restriction that the mass of the heavy quark should not be larger that the inverse lattice spacing.

$$ma \ll 1 \tag{3.46}$$

Current lattice simulations use inverse lattice spacings in the range $a^{-1} = 2$–4 GeV. Comparing this to the mass of a b-quark ($m_b \approx 4.5$GeV) we see that a naive approach is doomed to failure. For charm quarks ($m_c \approx 1.3$ GeV) it is not so cut-and-dried. As it is currently not feasible to reduce the lattice spacing sufficiently to simulate safely, instead an alternative discretisation is usually used. The idea is that simulating quarks with $ma \gg 1$ results in uncontrolled discretisation errors, so by choosing a suitably improved action and operators (see Section 2.4) it is possible to control these effects. Most techniques are based upon HQET. Usually the procedure is to use an alternative action for the heavy valence quarks, and simulate on a regular gauge background. The effects of heavy quarks are suppressed in loops, so neglecting them makes a negligible difference. It should be added that lattice spacings in some modern dynamical simulations are getting small enough that charm quarks can be simulated with the same action as light quarks. For example, the European Twisted Mass Collaboration (ETMC) have begun simulating with dynamical charm quarks [78, 79, 80], in so called $2+1+1$ flavour simulations.

3.4.1 Static Action

The static quark action, originally introduced by Eichten and Hill [81], is a lattice discretisation of the leading order HQET action. In this formulation the quarks are infinitely heavy and hence do not propagate in space. A propagator for a static quark reduces to the trace of the product of gauge matrices in the temporal direction. Numerically, static simulations are very simple to implement as it it is not necessary to perform an inversion of the Dirac matrix. The main problem with the static approach is that the signal to noise ratio can be poor, making it difficult to extract the desired observables. The standard approach to mitigate these problems is to apply smearing such as APE [82] or HYP [83] to the gauge matrices in the propagator. This reduces the short distance fluctuations in the gauge backgrounds and improves the signal to noise ratio. Despite the limitations of static quark simulations it has proved to be an effective and popular method for investigating heavy quark physics on the lattice. A number of calculations of $g_{B^*B\pi}$ have been performed in the static limit which will be discussed in Chapter 4.

3.4.2 Non-relativistic QCD

Non-relativistic QCD [84] is an effective theory most applicable to heavy quarkonium. Essentially it is HQET, but by using a power counting more suitable to heavy quark-anti-quark pairs the higher order terms are instead ordered by powers of v/c. Numerically the theory works very well, but has the disadvantage that no continuum limit is possible.

3.4.3 Relativistic Heavy Quark Action

The relativistic heavy quark (RHQ) action is an anisotropic Wilson action, with a Sheikholeslami-Wohlert term [51]. It is able to describe quarks in the region where $ma \ll 1$ and $ma \geq 1$, meaning it can be used for both heavy and light quarks. By breaking axis-interchange symmetry the RHQ action takes advantage of the fact that for heavy quarks, although the mass is large, the spatial derivative or momentum is not necessarily so. The action can be written as

$$S_{RHQ} = a^4 \sum_{x,y} \bar{\psi}(y) \Bigg(m_0 + \gamma_0 D_0 + \xi \vec{\gamma} \cdot \vec{D} - \frac{a}{2}(D_0)^2 - \frac{a}{2}\xi(\vec{D})^2 + \sum_{\mu\nu} \frac{ia}{4} c_p \sigma_{\mu\nu} F_{\mu\nu} \Bigg)_{y,x} \psi(x), \tag{3.47}$$

$$D_\mu \psi(x) = \frac{1}{2a} \left[U_\mu(x)\psi(x+\hat{\mu}) - U_\mu^\dagger(x-\hat{\mu})\psi(x-\hat{\mu}) \right], \tag{3.48}$$

$$D_\mu^2 \psi(x) = \frac{1}{a^2} \left[U_\mu(x)\psi(x+\hat{\mu}) + U_\mu^\dagger(x-\hat{\mu})\psi(x-\hat{\mu}) - 2\psi(x) \right], \tag{3.49}$$

$$F_{\mu\nu}\psi(x) = \frac{1}{8a^2}\sum_{s,s'=\pm 1} ss' \left[U_{s\mu}(x)U_{s'\nu}(x+s\hat{\mu})U^{\dagger}_{s\mu}(x+s'\hat{\nu})U^{\dagger}_{s'\nu}(x) - \text{h.c.}\right]\psi(x), \quad (3.50)$$

where m_0 is the bare quark mass, ξ is the anisotropy parameter and c_P is the coefficient for the isotropic Sheikholeslami-Wohlert term. The RHQ method was originally proposed independently by groups at Fermilab [85] and Tsukuba [86], but later Christ and Lin [87] showed that it could be written in the form of Equation (3.47) with only three unknown parameters. This is in contrast to the original formulation where six parameters were needed. Furthermore, they also showed that the three parameters (m_0, ξ, c_P) could be determined non-perturbatively. Once the action is tuned it is accurate to order $(ma)^n$ for all n and to first order in $|\bar{p}a|$. The tuning of the RHQ parameters has been completed for b-quarks [3] on the RBC/UKQCD configurations that are used in this thesis. In the next section we will briefly describe the tuning method from [3]. The lattice action is not Lorentz invariant, so mesons receive corrections to their energy-momentum dispersion relation due to lattice artifacts:

$$(aE)^2 = (aM_1)^2 + \left(\frac{M_1}{M_2}\right)(a\vec{p})^2 + \mathcal{O}([a\vec{p}]^4). \quad (3.51)$$

where

$$M_1 = E(\vec{p} = 0) \quad (3.52)$$

and

$$M_2 = M_1 \times \left(\frac{\partial E^2}{\partial P_i^2}\right)^{-1}_{\vec{p}=0} \quad (3.53)$$

are known as the rest mass and kinetic mass respectively.

3.4.4 RHQ parameter tuning

The tuning of the RHQ parameters was achieved by matching non-perturbative lattice calculations to experimental values. To fix the three unknown parameters three quantities are required. The chosen quantities are the spin-averaged B_s meson mass,

$$\overline{M}_{B_s} = \frac{1}{4}(M^*_{B_s} + 3M_{B_s}) \quad (3.54)$$

the hyperfine splitting,

$$\Delta M_{B_s} = M_{B^*_s} - M_{B_s} \quad (3.55)$$

and the requirement that the B_s meson rest (3.52) and kinetic masses (3.53) are equal such that they obey a continuum dispersion relation.

$$\frac{M_1^{B_s}}{M_2^{B_s}} = 1 \quad (3.56)$$

The B_s system was used as it contains no valence light quarks that require extrapolating to physical mass. The observables, in general, have a non-linear relationship with the parameters, but if a small enough range is chosen a linear approximation may be made. The tuning proceeds by choosing a box of parameters around a central point of size $\sigma_{\{m_0,\xi,c_P\}}$. The seven parameter sets are

$$\begin{gathered}\begin{bmatrix} m_0a \\ c_p \\ \xi \end{bmatrix}, \begin{bmatrix} m_0a - \sigma_{m0a} \\ c_p \\ \xi \end{bmatrix}, \begin{bmatrix} m_0a + \sigma_{m0a} \\ c_p \\ \xi \end{bmatrix}, \\ \begin{bmatrix} m_0a \\ c_p - \sigma_{c_p} \\ \xi \end{bmatrix}, \begin{bmatrix} m_0a \\ c_p + \sigma_{c_p} \\ \xi \end{bmatrix}, \begin{bmatrix} m_0a \\ c_p \\ \xi - \sigma_\xi \end{bmatrix}, \begin{bmatrix} m_0a \\ c_p \\ \xi + \sigma_\xi \end{bmatrix}.\end{gathered} \tag{3.57}$$

The observables are calculated on each set and then checks are made that the observables dependence on the parameters are indeed linear in this region. If so, the tuned parameter set can be calculated from the linear model

$$Y = J \begin{bmatrix} m_0a \\ \xi \\ c_p \end{bmatrix} + A \tag{3.58}$$

where Y is the vector of observables

$$Y = \begin{bmatrix} \bar{M}_{B_s} \\ \Delta M_{B_s} \\ \frac{M_1^{B_s}}{M_2^{B_s}} \end{bmatrix}. \tag{3.59}$$

The vector J is a finite difference approximation of the derivatives from the observables Y_i calculated on the ith parameter set (3.57).

$$J = \begin{bmatrix} \frac{Y_3 - Y_2}{2\sigma_{m_0a}}, & \frac{Y_5 - Y_4}{2\sigma_{c_P}} & \frac{Y_7 - Y_6}{2\sigma_\xi} \end{bmatrix} \tag{3.60}$$

$$A = Y_1 - J \times [m_0a, c_P, \xi]^T \tag{3.61}$$

We can then find the tuned parameters

$$\begin{bmatrix} m_0a \\ \xi \\ c_P \end{bmatrix}^{\text{RHQ}} = J^{-1} \times \left(\begin{bmatrix} \bar{M}_{B_s} \\ \Delta M_{B_s} \\ \frac{M_1^{B_s}}{M_2^{B_s}} \end{bmatrix}^{\text{PDG}} - A \right), \tag{3.62}$$

where the vector of observables are the experimental values from the PDG. The procedure ends when the tuned values on the left-hand side of (3.62) lie with the box of parameters defined by (3.57). This condition ensures that the tuned values are found by

interpolation, rather than extrapolation. If the parameters are not found to lie within the box, the box is moved and the process repeated.

3.5 Lattice Methods

3.5.1 Correlation Functions

We saw in section 3.1 that the observables that we wish to calculate in Lattice QCD are the vacuum expectation values of time ordered products of quark and gluon operators. Let us investigate in more detail the left hand side of (3.1). We will assume the simple case of two operators, $\mathcal{O}^\dagger$ and $\mathcal{O}$, which have the correct quantum numbers to create and destroy a pion from the vacuum. These can be constructed by selecting the correct Dirac bilinear from table 1.1, for instance, for a π^- we would choose

$$\mathcal{O}(x) = \bar{d}(x)\gamma_5 u(x). \tag{3.63}$$

The two-point correlation function is then

$$C(\vec{p}, t) = \sum_{\vec{x}} e^{i\vec{p}\cdot\vec{x}} \langle 0|\mathcal{O}(\vec{x}, t)\mathcal{O}^\dagger(\vec{0}, 0)|0\rangle, \tag{3.64}$$

where we have Fourier transformed to a definite momentum $\vec{p}$. Next, using the time translation operator

$$\hat{\mathcal{O}}(t) = e^{t\hat{H}}\hat{\mathcal{O}(}0)e^{-t\hat{H}} \tag{3.65}$$

we can move the operator at $\vec{x}$ back to the origin in time and insert a complete set of states:

$$C(\vec{p}, t) = \sum_{x} e^{i\vec{p}\cdot\vec{x}} \langle 0|\mathcal{O}(\vec{x}, 0)\frac{|n\rangle\langle n|}{2E_n}\mathcal{O}^\dagger(\vec{0}, 0)|0\rangle e^{-tE_n}. \tag{3.66}$$

The operators we chose have the quantum numbers of a pion, so only pions and their excited states will overlap. Setting the momentum to zero

$$C(t) = |\langle\pi|\mathcal{O}^\dagger|0\rangle|^2 e^{-m_\pi t} + |\langle\pi'|\mathcal{O}^\dagger|0\rangle|^2 e^{-m_{\pi'} t} + \cdots, \tag{3.67}$$

where π' refers to an excited pion state. If we wait for a large enough t the excited states will be sufficiently suppressed that we can access the ground-state pion's mass and the matrix element squared. Equation (3.67) is not completely correct as the pion states may also propagate backwards in time. Therefore, due to the periodicity of the lattice, the time dependence is actually cosh-like,

$$C(t) \propto e^{-mt} + e^{-m(T-t)} = 2e^{-mT/2}\cosh(m(T/2 - t)) \tag{3.68}$$

where T labels the time extent of the lattice.
As explained in Section 3.1 the correlator (3.64) is evaluated using the QCD path integral. First the fermionic part of the integral is performed and all the quark fields are contracted using Wick's theorem. Then the resulting gauge integral is performed by averaging over the gauge configurations (3.5). The Wick contraction of a pair of quark fields is given by the fermion propagator

$$\overbrace{q(x)\bar{q}(y)} = S(x,y), \tag{3.69}$$

which is evaluated by inverting the Dirac operator

$$D(x,z)S(z,y) = \delta(x,y), \tag{3.70}$$

typically using an iterative method such as Conjugate Gradient (see Section 3.5.6). For the example of a π^- in (3.66) the Wick contractions evaluate to

$$\begin{aligned} C(t) &= \mathrm{Tr}\left[S(\vec{x},t;\vec{0},0)\gamma_5 S(\vec{0},0;\vec{x},t)\gamma_5\right] \\ &= \mathrm{Tr}\left[S(\vec{x},t;\vec{0},0)S^\dagger(\vec{x},t;\vec{0},0)\right] \end{aligned} \tag{3.71}$$

where we have assumed degenerate light quarks, such that $S = S_u = S_d$, and in the last line utilised γ_5-hermiticity (3.79). For an iso-singlet operator,

$$\mathcal{O}_1 = \frac{1}{\sqrt{2}}\left(\bar{u}(x)\gamma_5 u(x) + \bar{d}(x)\gamma_5 d(x)\right), \tag{3.72}$$

there is an added complication. After performing the Wick contractions we get two contributions, a connected term, the same as (3.71), and a disconnected term

$$-2D(t) = -2\mathrm{Tr}\Big[S(\vec{x},t;\vec{x},t)\Big]\,\mathrm{Tr}\Big[S(\vec{0},0;\vec{0},0)\Big]. \tag{3.73}$$

The disconnected term is dominated by noise and difficult to evaluate numerically.

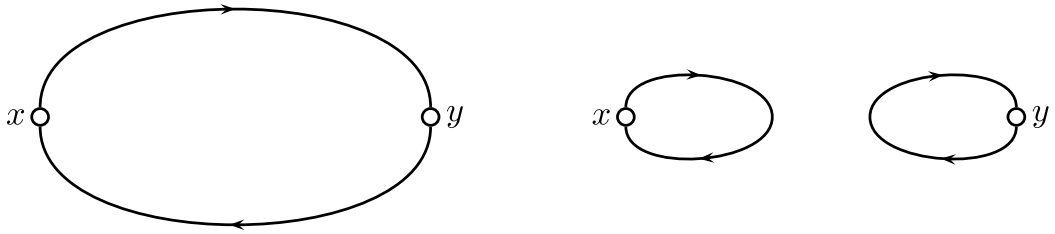

Figure 3.2: Connected (left) and disconnected contributions (right).

3.5.2 Effective Mass

To determine at what point the excited states have sufficiently decayed it is common to examine a quantity known as the *effective mass*, most-simply defined as he ratio of the correlator at successive time points

$$m_{\text{eff}}(t+\frac{1}{2}) = -\ln\frac{C(t)}{C(t+1)}. \tag{3.74}$$

When the exponentials coming from the excited states have decayed sufficiently $m_{\text{eff}} \approx m$. There are various definitions of the effective mass in use, however in this work we use the version above. If it is important to take into account the backwards propagating components, for instance light particles on a lattice with a small temporal extent, then construct

$$\frac{C(t)}{C(t+1)} = \frac{\cosh(m_{\text{eff}}(T/2-t))}{\cosh(m_{\text{eff}}(T/2-t+1))} \tag{3.75}$$

and solve for m_{eff} at every t. Figure 3.3 shows an effective mass plot for the B-meson two-point function. On the left-hand side the correlator is polluted by excited states, towards the middle, indicated by the blue band, there is a plateau where $m_{\text{eff}} \approx m$ holds, finally on the right-hand side the correlator becomes too noisy to see any signal. The effective mass plot show the region where the correlator can be fitted to extract the mass. Typically the mass is extracted from a fit to the correlator itself, rather than to the effective mass.

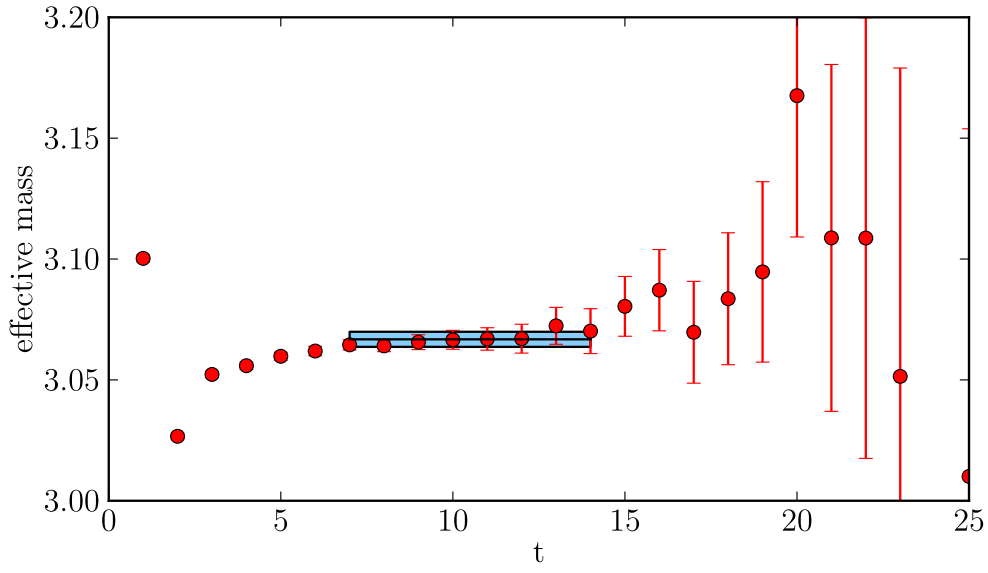

Figure 3.3: An effective mass plot of the B-meson correlator. The blue region shows the region where the correlator has been fitted.

3.5.3 Jack-Knife Analysis

In Monte-Carlo simulations it is necessary to calculate error estimates of expectation values coming from measurements that may be correlated. This arises because new gauge configurations are generated by updating the previous. Although measurements are not usually made on consecutive configurations, residual auto-correlations can still survive. Correlated measurements can cause error estimates to be underestimated. Furthermore, it is often necessary to calculate the error on some function of one or more, possibly related, expectation values. Here it is important to remember that generally $\langle f(x)\rangle \neq f(\langle x\rangle)$. The standard techniques to deal with these situations are known as *resampling methods*, consisting of jack-knife and bootstrap. The work conducted in this thesis relies on a single-elimination jack-knife technique [88] to estimate and propagate statistical errors.

For a quantity x that is evaluated on an ensemble of N configurations the jth jack-knife sample is defined as

$$\tilde{x}^j = \frac{1}{N-1}\sum_{i\neq j} x_i, \tag{3.76}$$

an average of all samples with one removed. To deal with the case where consecutive measurements are correlated, it is common to divide the data into blocks. In this case the jth sample has one block of size b removed and $N = n_x/b$. The standard error is then given in terms of the jack-knife samples

$$S.E. = \sqrt{N-1}\sigma = \sqrt{\frac{N-1}{N}\sum_j \left(\tilde{x}_j - \langle\tilde{x}\rangle\right)^2} \tag{3.77}$$

The size of the jack-knife blocks should be progressively increased, which will decrease correlations between blocks. If this process does not effect the errors, you can be happy that there are no significant correlations. In this work, to reduce correlations, consecutive measurements were performed on configurations translated by a random 4-vector (see Section 4.4), this allowed us to use jack-knife blocks of a single configuration. To correctly calculate errors from a function of different observables, such as in Section 4.4, the function is evaluated on each configuration and then the jack-knife is performed.

3.5.4 Point Sources

To evaluate the right-hand side of (3.1) in Lattice QCD it is necessary to calculate propagators for each gauge configuration in the sum of (3.5). This involves inverting the lattice Dirac operator ((3.31) for DWF), which is a very large and sparse matrix. For the lattices used in this thesis it has $\mathcal{O}(10^{17})$ elements, although many are zero. To calculate the complete inverse is not feasible, instead the standard technique is to

perform a *point inversion* by solving the equation

$$D(x,y)^{\alpha\beta}_{ab} S(y,0)^{\beta\beta_0}_{bb_0} = \delta_{x,y_0}\delta_{\alpha,\beta_0}\delta_{a,b_0}, \tag{3.78}$$

where the roman indices label colour and the greek indices label spin. This finds a single column of the inverse Dirac operator which gives a propagator from one space/spin/-colour point on the lattice to all others. Typically this inversion is completed twelve times, once for each spin-colour combination. The point-to-all propagator is more useful than it may at first seem due to a property called γ_5-hermiticity

$$\gamma_5 S(x,y)\gamma_5 = S^\dagger(y,x), \tag{3.79}$$

where the dagger applies to the spin and colour indices. This means if we calculate a propagator from one point on the lattice to all others, we can get the backward running propagator for free.

3.5.5 Extended Sources

A state created on the lattice using a local operator, such as from Table 1.1, may only have a small overlap with a physical meson, as this is an extended object. As finer lattices are used you will get less and less overlap with the physical meson states. To counteract this problem extended sources are introduced. This means we replace point-like interpolating operators with extended objects

$$\mathcal{O}(x) = \bar{\psi}^{(s)}(\vec{x},x_0)^a_\alpha \Gamma_{\alpha,\beta}\psi^{(s)}(\vec{x},x_o)^a_\beta \tag{3.80}$$

where the superscript s on the quark fields stands for smeared. The smeared fields are related to the point fields through

$$\psi^{(s)}(\vec{x},x_o)^a_\alpha = \sum_{\vec{y}} \mathcal{S}(\vec{x},\vec{y})^{ab}_{\alpha\beta}\psi(\vec{y},x_0)^b_\beta. \tag{3.81}$$

There are many possible choices of S available, some of which are gauge invariant, some of which are not. A popular choice is the wall source

$$\mathcal{S}(\vec{x},\vec{y})^{ab}_{\alpha\beta} = \mathbb{1}\delta_{ab}\delta_{\alpha,\beta}, \tag{3.82}$$

which is equivalent to a 'wall' of point sources on a single time slice. However, to use wall sources it is first necessary to fix the gauge. This is because the gauge average of a non-gauge invariant quantity is always zero. In this work we use a smearing motivated by the attractive idea that the meson wave function should be approximately Gaussian [89, 90]. This can be implemented on the lattice in a gauge invariant manner with a

smearing function

$$\mathcal{S}(\sigma, n_\sigma; \vec{x}, \vec{y})^{ab}_{\alpha\beta} = \left(1 + \frac{\sigma^2}{2n_\sigma}\Delta(x,y)\right)^{n_\sigma} \delta_{ab}\delta_{\alpha,\beta}, \tag{3.83}$$

where $\Delta(x,y)$ is the lattice Laplacian

$$\Delta(x,y) = \sum_{\mu=1}^{3} \left(U_\mu(x)\delta_{x+\hat{\mu},y} + U^\dagger_\mu(x-\hat{\mu})\delta_{x-\hat{\mu},y} - 2\delta_{x,y}\right). \tag{3.84}$$

The smearing has two parameters σ and n_σ which correspond to the Gaussian radius and the number iterations used to approximate the exponential. It should be noted that smearing can be applied at either end of a propagator. For a smeared source the propagator is inverted using a smearing function as the source term, whereas for a smeared sink the smearing can be applied afterwards.

3.5.6 Conjugate Gradient

Equation (3.70) can be solved iteratively using an algorithm such as Conjugate Gradient. Conjugate Gradient solves $Ax = b$ for hermitian positive-definite A by minimising the quadratic form $f(x) = x^T b - x^T Ax$. At each step the algorithm searches for the minimum along a direction A-orthogonal to the last search direction. As the algorithm progresses through iterative applications of the matrix A it is ideally suited for large sparse problems where direct methods are impractical. Although the method relies on a hermitian matrix A, which often is not the case for lattice Dirac operators, the problem can easily be rephrased in terms of the normal equations $A^\dagger Ab = A^\dagger x$.

Figure 3.4: The conjugate gradient algorithm

$d_0 = r_0 = b - Ax_0$
loop
  $\alpha_i = \frac{r_i^T r_i}{d_i^T A d_i}$
  $x_{i+1} = x_i + \alpha_i d_i$
  $r_{i+1} = r_i + \alpha_i A d_i$
  if $r_{i+1} < \epsilon$ **then**
    exit
  end if
  $\beta_{i+1} = \frac{r_{i+1}^T r_{i+1}}{r_i^T r_i}$
  $d_{i+1} = r_{i+1} + \beta_{i+1} d_i$
end loop

The rate of convergence of Conjugate Gradient is proportional to the square-root of the condition number of the matrix, which, for a normal matrix, is equal to the ratio of the largest to smallest eigenvalue. For lattice simulations with small quark masses the Dirac

operator becomes extremely ill-conditioned and this is one of the reasons why simulating with physical quark masses proves challenging [1].

3.5.7 Preconditioning

For badly conditioned matrices it is often possible solve a related system that has a better condition number. Generally, this means solving

$$P^{-1}APx = P^{-1}b, \tag{3.85}$$

for a choice of P such that $P^{-1}AP$ has a smaller condition number that A. A specific type of preconditioning that works well with the domain wall fermion Dirac operator is even-odd preconditioning. This involves decomposing the Dirac operator into even and odd sites, where $(x_1 + x_2 + x_3 + x_4)$ is even or odd[2], and performing an Schur decomposition

$$\begin{aligned} D_{DWF} &= \begin{pmatrix} M_{ee} & M_{eo} \\ M_{oe} & M_{oo} \end{pmatrix} \\ &= \begin{pmatrix} 1 & 0 \\ M_{oe} & M_{ee}^{-1} \end{pmatrix} \begin{pmatrix} M_{ee} & 0 \\ 0 & D_{oo} \end{pmatrix} \begin{pmatrix} 1 & M_{ee}^{-1}M_{eo} \\ 0 & 1 \end{pmatrix} \\ &= LDU, \end{aligned} \tag{3.86}$$

where

$$D_{oo} = M_{oo} - M_{oe}M_{ee}^{-1}M_{eo}. \tag{3.87}$$

We wish to solve the equation

$$\begin{aligned} D_{DWF}\psi &= \eta \\ LDU\psi &= \eta \\ DU\psi &= L^{-1}\eta, \end{aligned} \tag{3.88}$$

which, in terms of even and odd vectors is

$$\begin{pmatrix} M_{ee} & M_{eo} \\ 0 & D_{oo} \end{pmatrix} \begin{pmatrix} \psi_e \\ \psi_o \end{pmatrix} = \begin{pmatrix} 1 & 0 \\ -M_{oe}M_{ee}^{-1} & 1 \end{pmatrix} \begin{pmatrix} \eta_e \\ \eta_o \end{pmatrix} \tag{3.89}$$

$$\begin{pmatrix} M_{ee}\psi_e + M_{eo}\psi_o \\ D_{oo}\psi_o \end{pmatrix} = \begin{pmatrix} \eta_e \\ \eta_o - M_{oe}M_{ee}^{1}\eta_e \end{pmatrix}. \tag{3.90}$$

[1] The other main reason is that for lighter quarks it is necessary to have a larger physical volume because lighter particles tend to propagate further and thus finite volume effects can become large if the volume is too small.

[2] This is called 4D preconditioning. An alternative is 5D preconditioning where the definition of even or odd sites is based upon $(x_1 + x_2 + x_3 + x_4 + x_5)$

We can then iteratively solve

$$D_{oo}\psi_o = \eta_o - M_{oe}M_{ee}^1\eta_e = \eta'_o \tag{3.91}$$

and reconstruct the even part of the solution using

$$\psi_e = M_{ee}^{-1}(\eta_e - M_{eo}\psi_o). \tag{3.92}$$

The matrix D_{oo} has a smaller condition number that D_{DWF} and hence reduces the number of CG iterations by about a factor of two. This method relies on the fact that for domain wall fermions the inverse M_{ee}^{-1} is trivial to find. Another effective method of preconditioning is *deflation* — this is discussed in the next section.

3.5.8 Low mode averaging

It has been observed that meson correlations functions, at small quark masses and large temporal separations, are dominated by the eigenmodes of the Dirac operator with the smallest eigenvalues [91]. This observation suggests that by calculating a small number of the lowest eigenmodes and forming a spectral decomposition of the Dirac operator in the subspace spanned by the low-modes we can calculate the dominant part of the propagator exactly.

$$D(x,y)i(y) = \lambda_i i(x) \tag{3.93}$$

$$S(x,y) = \sum_i^N \frac{1}{\lambda_i} i(x) \otimes i^\dagger(y) + S_{\text{high}}(x,y) \tag{3.94}$$

The low mode part of the propagator is all-to-all, meaning it is possible to take advantage of the translation invariance of the theory to obtain a volume average. For instance, returning to the pion correlator in (3.71), we could instead calculate

$$C(t) = \frac{1}{VT}\sum_{\vec{x},\vec{y},\tau} \text{Tr}\left[S(\vec{x},\tau+t;\vec{y},\tau)\gamma_5 S(\vec{y},\tau;\vec{x},\tau+t)\gamma_5\right], \tag{3.95}$$

where V is the volume, and T is the spatial extent of the lattice. This correlator has a smaller variance than (3.71) and makes better use of the information present in each configuration. Furthermore, all-to-all propagators make the evaluation of disconnected contributions (3.73) feasible. The eigenvectors can be calculated using an algorithm such as Implicitly Restarted Arnouldi Method (IRAM) [92], or the Kalkreuter-Simma method [93].

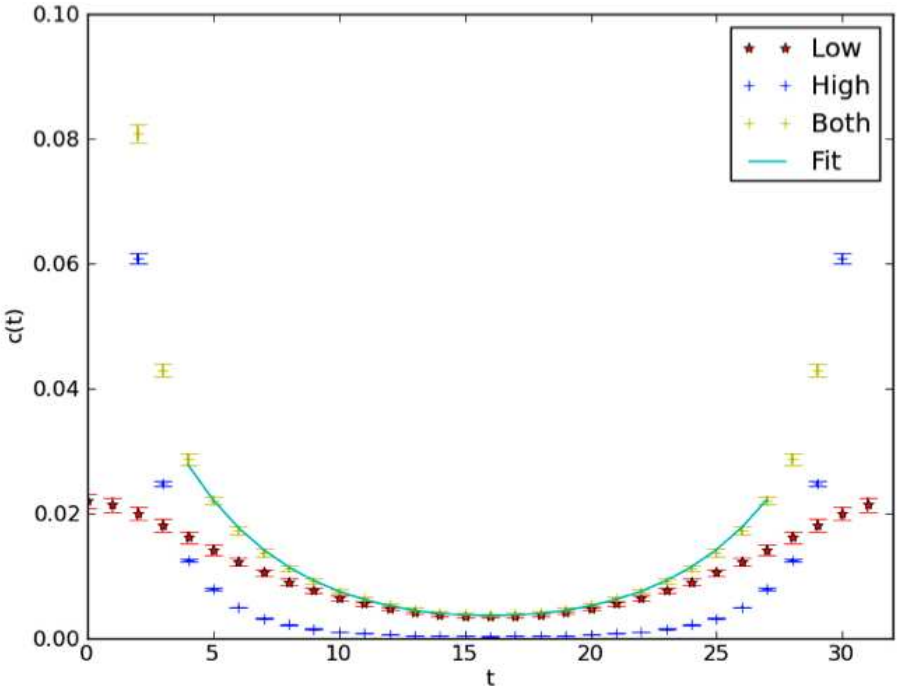

Figure 3.5: Pion correlator constructed using 20 eigenmodes and 64 stochastic sources.

3.5.9 Stochastic sources

It is still necessary to estimate the contribution to the propagator S_{high} in the subspace orthogonal to the eigenmodes. One way this can be achieved, which also permits volume averaging, is by using stochastic sources [94, 95]. The general idea is to generate a set of random vectors with the property

$$\sum_{r}^{N_r} \frac{1}{N_r} \eta^r(x) \otimes \eta^{r\dagger}(y) \approx \delta(x,y), \tag{3.96}$$

where in the limit $N_r \to \infty$ the equality becomes exact. This can be achieved, for example, by filling every component of the vector with complex $\mathbb{Z}(2) \otimes \mathbb{Z}(2)$ noise, a choice that provides good variance reduction [96]. To construct the all-to-all propagator it is necessary to solve the equation

$$D(x,y)\psi^r(y) = \eta^r(x) \tag{3.97}$$

for each source vector. The approximate propagator can then be written as the sum

$$S(x,y) \approx \sum_{r}^{N_r} \frac{1}{N_r} \psi^r(x) \otimes \eta^{r\dagger}(y). \tag{3.98}$$

To find only the high-mode part of the propagator the Dirac operator is projected into the high-mode subspace before solving (3.97):

$$P_h D(x,y) P_h \psi^r(y) = \eta^r(x) \tag{3.99}$$

where

$$P_h = 1 - P_l = 1 - \sum_i^N i(x) \otimes i^\dagger(y). \tag{3.100}$$

This has the added benefit that the Dirac operator operator's condition number is improved, and is known as deflation. This can be easily seen by considering the condition number as the ratio of the operator's largest to smallest eigenvalue. Figure 3.6 shows the effect of deflation on the number of matrix-vector products necessary to solve (3.99).

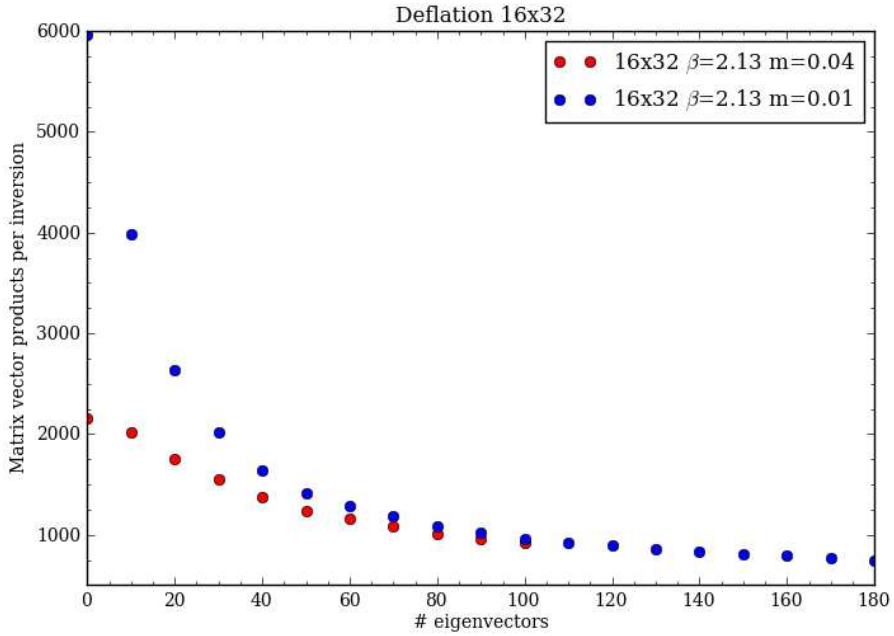

Figure 3.6: The effect of deflation for two different quark masses. For lighter quark masses the Dirac operator is worse conditioned and deflation has a larger effect.

3.5.10 The one-end trick

The method of low mode averaging (LMA) with stochastic sources, described above, is particularly suitable for evaluating disconnected contributions, however for connected correlators a better method is the *one-end trick* [97, 98]. Consider a zero-momentum

meson two-point function averaged over the lattice volume:

$$\begin{aligned} C(t) &= \frac{1}{V}\sum_{\vec{x},\vec{y}} \mathrm{Tr}\Big[S(x,y)\Gamma_1 S(y,x)\Gamma_2\Big] \\ &= \frac{1}{V}\sum_{\vec{x},\vec{y}} \mathrm{Tr}\Big[S(x,y)\Gamma_1\gamma_5 S^\dagger(x,y)\gamma_5\Gamma_2\Big]. \end{aligned} \tag{3.101}$$

Then generate a set of stochastic wall sources,

$$\eta(\vec{x},\tau) = \begin{cases} \mathbb{Z}(2)\otimes\mathbb{Z}(2) & \text{if } t_x = \tau \\ 0 & \text{if } t_x \neq \tau \end{cases} \tag{3.102}$$

that can be used to approximate a delta function

$$\frac{1}{N_r}\sum_{r}^{N_r} |\eta^r(\vec{x},\tau)\rangle\langle\eta^r(\vec{y},\tau)| \approx \delta(\vec{x},\vec{y})\delta(t,\tau). \tag{3.103}$$

The we insert the above delta function into equation (3.101)

$$C(t) = \frac{1}{VN_r}\sum_{\vec{x},\vec{y},\vec{z},r} \mathrm{Tr}\Big[S(x,y)|\eta^r(y)\rangle\langle\eta^r(z)|\Gamma_1\gamma_5 S^\dagger(x,z)\gamma_5\Gamma_2\Big]. \tag{3.104}$$

giving

$$C(t) = \frac{1}{VN_r}\sum_{\vec{y},r} \mathrm{Tr}\Big[\langle\psi^r_\Gamma(y)|\gamma_5\Gamma_2|\psi^r(y)\rangle\Big] \tag{3.105}$$

$$|\psi^r(y)\rangle = S(y,x)|\eta^r(x)\rangle \tag{3.106}$$

$$|\psi^r_\Gamma(y)\rangle = S(y,x)(\Gamma_1\gamma_5)^\dagger|\eta^r(x)\rangle. \tag{3.107}$$

In the definition of ψ_Γ (3.107) we see that the product $\Gamma_1\gamma_5$ appears. For $\Gamma_1 = \gamma_5$ this gives the identity and $\psi_\Gamma = \psi$, meaning only one propagator inversion is needed. For other gamma-matrices it is possible to calculate the spin components separately and construct the different ψ_Γ explicitly. The one-end trick has an advantage over the stochastic method described in Section 3.5.8 because only one stochastic delta function is introduced, meaning less noise. However, it cannot be used for disconnected quantities.

Chapter 4

The $B^*B\pi$ coupling

In this chapter I describe a calculation of the $B^*B\pi$ coupling. The coupling is directly related to the LEC g_b of HMχPT as described in section 2.2. The coupling is relevant to improving the accuracy of the chiral extrapolations necessary in the RBC/UKQCD collaboration's ongoing B-physics program. This includes calculations of $B_0 - \bar{B}_0$ mixing and the form-factor $f_+(q^2)$ from $B \to \pi l \nu$ decay which were both discussed in Chapter 1.

There has long been interest in fixing the value of the coupling g. The first estimates were made using non-relativistic quark models [99] which gave a value of $g = 1$. Later relativistic models revised the estimate down to $g = 1/3$ [100]. A number of calculations have been made using QCD sum rules [101, 102, 103, 104], which predict a wide spread of values from $g = 0.09 - 0.55$. In the D system the decay $D^* \to D\pi$ has sufficient phase space to occur and has been measured by the CLEO [105] giving a value of $g_{D^*D\pi} = 17.9 \pm 0.3 \pm 1.9$, and hence $g_c = 0.59 \pm 0.01 \pm 0.07$. More recently a preliminary result has come from the BaBar experiment at SLAC of $g_c = 0.76 \pm 0.01$. The first lattice study of the coupling was a quenched calculation on a $a^{-1} = 1.1$ GeV lattice by UKQCD [106]. The simulation was performed in the static limit using the action of Eichten and Hill [81] and clover improved light-quarks. They calculated a value of $g_\infty = 0.42 \pm 0.04 \pm 0.08$. This result agrees well with previous theoretical determinations, but was only considered a proof-of-concept study due to large uncertainties from the chiral extrapolation and uncontrolled errors arising from the quenched approximation. In 2002 Abada et al. [107] performed another quenched calculation with clover improved quarks which they extrapolated up to the charm mass. Later they combined this calculation with another on the same lattice, but with static heavy-quarks allowing an interpolation to the b-quark mass. The results from the two studies are $g_c = 0.67 \pm 0.08 \pm 0.06$, $g_b = 0.58 \pm 0.06 \pm 0.10$ and $g_\infty = 0.48 \pm 0.03 \pm 0.11$. The first fully dynamical $n_f = 2$ study was performed by Ohki et al., again in the static limit. They applied low mode averaging (see Section 3.5.8) to achieve very small statistical errors, and made a chiral extrapolation using both a linear and chiral log formula. For their final result they quote

$g_\infty = 0.516 \pm 0.005 \pm 0.033 \pm 0.028 \pm 0.028$, where the sources of errors are statistical, chiral, pertubative and discretisation respectively. In the last year we have for the first time seen studies considering all sources of systematic error. Detmold, Lin and Meinel [108] calculated the static coupling on RBC/UKQCD $2+1$ flavour gauge configurations (as used in this work) and considered all sources of systematics. In a companion paper [109] they derived an NLO expression in HMχPT for the axial vector current matrix element that allowed them to take a theoretically guided extrapolation to the chiral limit. Their final quoted value is $g_\infty = 0.449 \pm 0.047 \pm 0.019$. Furthermore, Becirevic and Sanfilippo [110] recently made a calculation using the twisted mass action of the coupling g_c. They used configurations with a small lattice spacing and $\mathcal{O}(a)$ improved quarks to simulate directly at the charm mass. Calculations on multiple lattices confirmed that they had discretisation effects under control. Their final result is $g_c = 0.54 \pm 0.03 \pm 0.03$. The only missing piece in the jigsaw is a calculation of the coupling directly with physical b-quarks. Moreover, this is arguably a more important quantity as it is not directly accesible through experiment. This is the aim of the calculation performed here.

This chapter is organised as follows. In section 4.1 we show how the $B^*B\pi$ matrix element can be described by a form factor decomposition and discuss which form factors are of interest. In section 4.2 the focus will be on how best to perform the lattice QCD calculation, where we will compare a number of different approaches and their relative costs. Sections 4.3 and 4.4 will introduce the necessary correlation functions and define ratios which will allow us to extract the quantities of interest, and in Section 4.5 we will describe the renormalisation of the axial vector current that is used. Section 4.6 will describe the details of the calculation and then we will finish with results (section 4.7), an in-depth investigation of the systematic errors (section 4.8) and finally conclusions (section **??**).

4.1 Form Factors

As outlined in section 2.3.1 the coupling $g_{B^*B\pi}$ is defined by the strong matrix element

$$\langle B(p)\pi(q)|B^*(p',\lambda)\rangle = -g_{B^*B\pi}\, q\cdot\epsilon^\lambda(p'). \tag{4.1}$$

To transform this matrix element into a vacuum expectation value of fields we perform an LSZ reduction on equation (4.1)

$$g_{B^*B\pi}\, q\cdot\epsilon^\lambda(p') = i(m_\pi^2 - q^2)\int d^4x\; e^{iq\cdot x}\langle B(p)|\pi(x)|B^*(p',\lambda)\rangle. \tag{4.2}$$

where $\pi(x)$ is an interpolating operator for the pion. By applying the partially-conserved axial current relation (PCAC)

$$\pi(x) = \frac{1}{m_\pi^2 f_\pi}\partial^\mu A_\mu(x), \tag{4.3}$$

we can then write the matrix element of equation (4.1) in a form more amenable to lattice simulation

$$g_{B^*B\pi}(q^2)\epsilon^\lambda \cdot q = \frac{m_\pi^2 - q^2}{f_\pi m_\pi^2}\int d^4x\; e^{iq\cdot x}\langle B(p)|q_\mu A^\mu(x)|B^*(p',\lambda)\rangle \tag{4.4}$$

where $A^\mu = \bar{q}\gamma^\mu\gamma_5 q$ is the light-quark axial vector current. If we parameterise the axial current matrix element in term of form factors

$$\begin{aligned}\langle B(p)|A^\mu|B^*(p',\lambda)\rangle = {} & 2m_{B^*}A_0(q^2)\frac{\epsilon\cdot q}{q^2}q^\mu \\ & + (m_{B^*}+m_B)A_1(q^2)\left[\epsilon^\mu - \frac{\epsilon\cdot q}{q^2}q^\mu\right] \\ & + A_2(q^2)\frac{\epsilon\cdot q}{m_{B^*}+m_B}\left[p^\mu + p'^\mu - \frac{m_{B^*}^2 - m_B^2}{q^2}q^\mu\right],\end{aligned} \tag{4.5}$$

we see by taking the divergence of equation (4.5) that at $q^2 = 0$

$$g_{B^*B\pi} = \frac{2m_{B^*}A_0(0)}{f_\pi}. \tag{4.6}$$

We cannot simulate exactly at $q^2 = 0$ in lattice QCD as the finite extent of the lattice means we can only access discrete momenta. The smallest non-zero momentum available is $\pi/L \approx 220$ MeV, on the lattices used in this study. This compares to $m_{B^*} - m_B \approx 45$ MeV [30] which gives a measure of the tuning of the B-mesons' momenta that would be needed to set $q^2 = 0$. One possible technique to simulate at q^2=0 would be using twisted boundary conditions [111, 112]. Furthermore, from equations (4.5) and (4.4) we also see the form factor A_0 contains the pion pole, so it will be difficult to extrapolate. However, the form factor decomposition in equation (4.5) must be free of unphysical poles, which allows us to obtain the relation

$$2m_{B^*}A_0(0) = (m_{B^*}+m_B)A_1(0) + (m_{B^*}-m_B)A_2(0), \tag{4.7}$$

and hence

$$g_{B^*B\pi} = \frac{1}{f_\pi}\left[(m_{B^*}+m_B)A_1(0) + (m_{B^*}-m_B)A_2(0)\right]. \tag{4.8}$$

Similarly, we have

$$g_b = \frac{1}{2m_B}\left[(m_{B^*}+m_B)A_1(0) + (m_{B^*}-m_B)A_2(0)\right], \tag{4.9}$$

by using the relation in (2.47). Furthermore, we will see that the q^2 dependence of A_1 and A_2 is mild, so an extrapolation to $q^2 = 0$ is not a problem. The splitting between the vector and the pseudoscalar B-meson masses is a percent level effect, therefore the dominant contribution to the coupling comes from the form factor A_1. For infinite heavy-quark mass the B and the B^* become degenerate and we get the simplified relation

$$g_\infty = A_1(0). \tag{4.10}$$

4.2 Calculational Strategy

To determine the form factors in Eq. (4.9), we need to calculate the matrix element $\langle B(p)|A^\mu|B^*(p',\lambda)\rangle$. This can be accessed through a lattice three-point correlation function of a light-quark axial vector current and interpolating operators for a B and a B^*-meson. We have chosen to calculate the light-quark using the domain-wall action and the heavy-quark propagators using the tuned RHQ action. As we are dealing with a light axial vector current we do not need to consider improvement of any operators containing b-quarks. Furthermore, we can make use of the light axial vetor current renormalisation constant that has been non-pertubatively calculated by the RBC-UKQCD collaboration. We will discuss this in more detail in Section 4.5. Due to the extra-dimension used in the domain-wall formulation, and the fact the Dirac matrix is poorly conditioned for light-quarks, the DWF inversions are far more costly that the heavy-quark inversions. Table 4.1 shows a comparison of the times for each inversion on 32 nodes of the University of Southampton Iridis 3 cluster for the RBC-UKQCD 24^3 x 64, $m_{ud} = 0.005$, $\beta = 2.13$ configurations. As can be seen the cost of an RHQ inversion is insignificant versus a DWF inversion, so it is preferable to limit the number of light-quark propagators calculated. Furthermore, the RBC-UKQCD collaboration have precalculated DWF propagators stored on disk which could be reused wherever possible. We considered three different approaches to organise the calculation.

Propagator	Time
DWF $m_{ud} = 0.005$	14721 seconds
RHQ $m = 7.8$	11 seconds

Table 4.1: Propagator calculation time using 32 nodes of Iridis 3 on the RBC-UKQCD 24^3 x 64, $m_{ud} = 0.005$, $\beta = 2.13$ configurations.

4.2.1 Method I

The B^*-meson is created at the origin using a smeared interpolator, and destroyed at fixed time t_y. The spatial position of the B-meson interpolator can be summed to Fourier transform it to zero momenta. Potentially, partially twisted boundary conditions could

be used to tune the momentum of the B^*-meson such that $q^2 = 0$. The signal can be searched for by varying the time t_z. This approach would involve calculating a heavy propagator from the origin and a light sequential propagator from t_y. The precalculated propagators could be reused for the light-quark propagator from the origin to t_z. This method would require a minimum of one DWF inversion, and more if twisted boundary conditions were used.

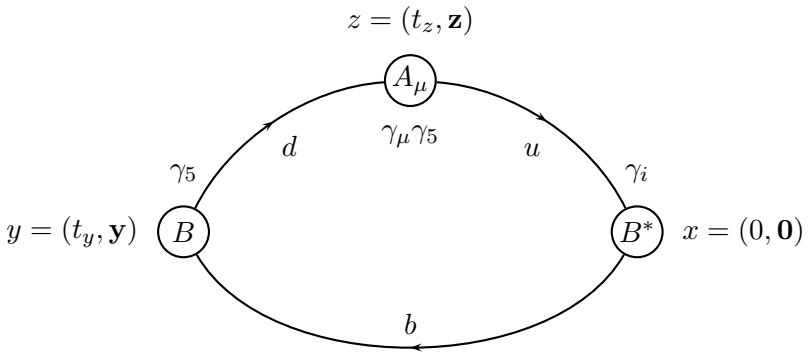

Figure 4.1: Quark flow diagram for the $\langle B(p)|A_\mu(q)|B^*(p')\rangle$ three-point function with Gaussian smeared source and sink.

4.2.2 Method II

To try to achieve a cleaner signal we could use a stochastic source for the B^*-meson [96, 113], or more specifically employ the one-end trick [98]. This involves using a vector of $\mathbb{Z}_2$ noise in every spatial component of a single time slice as a propagator source (see Section 3.5.10). The idea being to cheaply get a *volume average*, better utilise the information in the configurations, and achieve smaller statistical errors. Using this method we would not be able to reuse the saved DWF propagators and a minimum of two light inversions would be necessary.

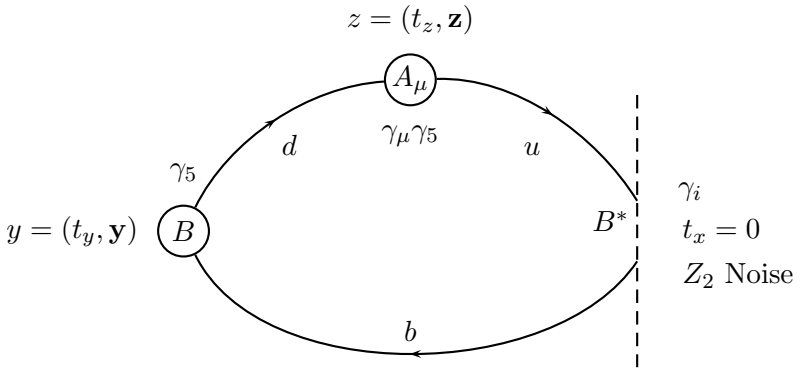

Figure 4.2: Quark flow diagram for the $\langle B(p)|A_\mu(q)|B^*(p')\rangle$ three-point function using a stochastic wall source

4.2.3 Method III

To maximise the benefit of having precalculated DWF propagators we could rearrange the calculation such that the axial vector current is at the origin. This means that we can use precalculated propagators for both light-quarks. This is a different technique to how three-point functions are typically calculated [114]. Usually the position of the creation and anhilation operators are fixed and the other operator is scanned between them. Instead we could fix the axial vector current at the origin and scan the position of the B^* creation operator to find the signal. As the axial current is placed at the origin we would need to employ the periodicity of the lattice to create the B^* at a large time and propagate it across the origin. The B-meson could then be destroyed at some small time. Using this method no light inversions are needed. It is however necessary to perform a number of heavy-quark inversions to tune the optimal place to destroy the B-meson. These inversions are cheap and will not significantly affect the cost of this method

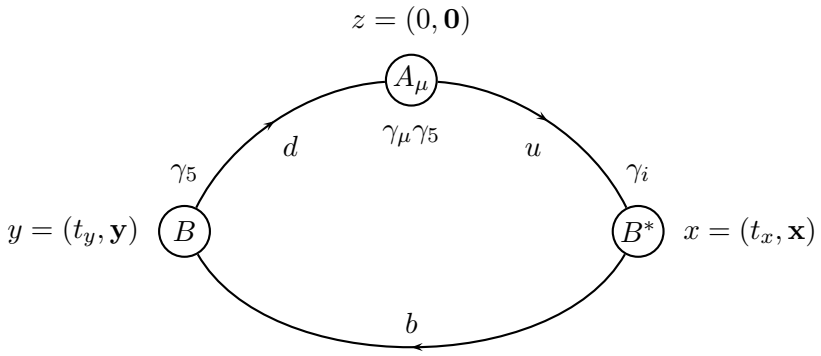

Figure 4.3: Quark flow diagram for the $\langle B(p)|A_\mu(q)|B^*(p')\rangle$ with the operators arranged such that precalculated propagators can be used.

It was decided to pursue the calculation using method III. We would be able to see after a small amount of computation if it was possible to achieve a clean signal for the correlation functions.

4.3 Correlation Functions

To access the matrix element in equation (4.4) we calculate the lattice three-point function:

$$\begin{aligned} C^{(3)}_{\mu\nu}\left(t_x, t_y; \bar{p}, \bar{p}'\right) &= \sum_{\bar{x}\bar{y}} e^{-\imath\bar{p}\cdot\bar{x}} e^{-\imath\bar{p}'\cdot\bar{y}} \langle B(y) A_\nu(0) \overline{B^*_\mu}(x)\rangle_{t_x<0<t_y} \\ &\approx \sum_\lambda \frac{Z_B^{1/2} Z_{B^*}^{1/2}}{2E_B 2E_{B^*}} \langle B(p')|A_\nu|B^*(p,\lambda)\rangle (\epsilon^\lambda)_\mu e^{-E_B t_y} e^{-E_{B^*}(T-t_x)}. \end{aligned} \tag{4.11}$$

and the vector and pseudoscalar two-point functions:

$$C^{(2)}_{BB}\left(t;\bar{p}\right) = \sum_{\bar{x}} e^{-\imath\bar{p}\cdot\bar{x}}\langle B(x)\overline{B}(0)\rangle \approx Z_B \frac{e^{-E_B t}}{2E_B} \tag{4.12}$$

$$C^{(2)}_{B^*_\mu B^*_\nu}\left(t;\bar{p}\right) = \sum_{\bar{x}} e^{-\imath\bar{p}\cdot\bar{x}}\langle B^*_\nu(x)\overline{B^*}_\mu(0)\rangle \approx Z_{B^*} \frac{e^{-E_{B^*} t}}{2E_{B^*}} \left(\delta_{\mu\nu} - \frac{p_\mu p_\nu}{p^2},\right) \tag{4.13}$$

Here, Z_B and Z_{B^*} correspond to the pseudoscalar and vector matrix elements respectively, and λ labels the vector meson's polarisation state. In the RHS of equation (4.13), the polarisation states have been summed over. The (local) interpolating operators used in equations (4.11, 4.12, 4.13) are given by

$$B(x) = \bar{d}(x)\gamma_5 b(x), \quad B^*_\mu(x) = \bar{u}(x)\gamma_i b(x), \quad A_\nu(x) = \bar{u}(x)\gamma_\mu\gamma_5 d(x). \tag{4.14}$$

The approximate equalities in equations (4.11, 4.12, 4.13) are due to the excited B and B^*-meson states that the interpolators also produce. For $t \to \infty$ the excited states are suppressed and the equalities become exact.

4.3.1 Three-point correlation function

The necessary trace to calculate the three-point function in figure 4.3 and equation (4.11) is

$$\begin{aligned} C^{(3)}_{\mu\nu}\left(t_x, t_y; \bar{p}, \bar{p}'\right) &= \sum_{\bar{x}\bar{y}} e^{-\imath\bar{p}\cdot\bar{x}} e^{-\imath\bar{p}'\cdot\bar{y}} \left\langle \bar{d}(y)\gamma_5 b(y)\bar{u}(0)\gamma_\mu\gamma_5 d(0)\bar{b}(x)\gamma_\nu u(x)\right\rangle \\ &= \sum_{\bar{x}\bar{y}} e^{-\imath\bar{p}\cdot\bar{x}} e^{-\imath\bar{p}'\cdot\bar{y}} \ \mathrm{Tr}\Big[S_l\left(0,y\right)\gamma_5 S_h\left(y,x\right)\gamma_\nu S_l\left(x,0\right)\gamma_\mu\gamma_5\Big]. \end{aligned} \tag{4.15}$$

where we have avoided a possible disconnected contribution by not using the iso-singlet π^0. In the second line we have used isospin symmetry to set $S_u = S_d = S_l$. We can use pre-calculated point source light-quark propagators $S_l\left(x,0\right)$, where

$$D_{DWF}\left(y,z\right) S_l\left(z,0\right) = \delta\left(y\right) \tag{4.16}$$

$$D^{-1}_{DWF}\left(x,y\right) D_{DWF}\left(y,z\right) S_l\left(z,0\right) = D^{-1}_{DWF}\left(x,y\right)\delta\left(y\right) \tag{4.17}$$

$$S_l\left(x,0\right) = D^{-1}_{DWF}\left(x,y\right)\delta\left(y\right). \tag{4.18}$$

We solve the equation

$$D_{RHQ}\left(y,x\right)\Sigma\left(x,0\right) = \gamma_5 S_l\left(y,0\right)\gamma_5 e^{i\vec{p}'\cdot\vec{y}}\delta_{y_0,t_y} \tag{4.19}$$

to give the sequential propagator, defined as:

$$\Sigma\left(x,0\right)=\sum_{\vec{y}}e^{i\vec{p}'\cdot\vec{y}}S_h\left(x,y\right)\gamma_5 S_l\left(y,0\right)\gamma_5. \tag{4.20}$$

Using γ_5-hermiticity

$$\gamma_5\Sigma^\dagger\left(x,0\right)\gamma_5=\sum_{\vec{y}}e^{i\vec{p}'\cdot\vec{y}}\gamma_5 S_l\left(0,y\right)\gamma_5 S_h\left(y,x\right), \tag{4.21}$$

which is the quantity needed in (4.15)

$$C^{(3)}_{\mu\nu}\left(t_x,t_y;\bar{p},\bar{p}'\right)=\sum_{\bar{x}\bar{y}}e^{-\imath\bar{p}\cdot\bar{x}}\ \mathrm{Tr}\left[\gamma_5\Sigma^\dagger\left(x,0\right)\gamma_5\gamma_\nu S_l\left(x,0\right)\gamma_\mu\right] \tag{4.22}$$

$$=\sum_{\bar{x}\bar{y}}e^{-\imath\bar{p}\cdot\bar{x}}e^{-\imath\bar{p}'\cdot\bar{y}}\ \mathrm{Tr}\Big[S_l\left(0,y\right)\gamma_5 S_h\left(y,x\right)\gamma_\nu S_l\left(x,0\right)\gamma_\mu\gamma_5\Big] \tag{4.23}$$

We pick multiple choices of t_y in the first half of the lattice, and then look at t_x in the second half of the lattice.

4.3.2 Two-point correlation function

Again, by Wick contracting the two-point functions in (4.12) and (4.13) we arrive at the following traces

$$\begin{aligned}C^{(2)}_{BB}\left(t;\bar{p}\right)&=\sum_{\bar{x}}e^{-\imath\bar{p}\cdot\bar{x}}\ \mathrm{Tr}[\gamma_5 S_h(x,0)\gamma_5 S_l(0,x)]\\&=\sum_{\bar{x}}e^{-\imath\bar{p}\cdot\bar{x}}\ \mathrm{Tr}[S_h(x,0)S_l^\dagger(x,0)]\end{aligned} \tag{4.24}$$

$$\begin{aligned}C^{(2)}_{B^*_\mu B^*_\nu}\left(t;\bar{p}\right)&=\sum_{\bar{x}}e^{-\imath\bar{p}\cdot\bar{x}}\ \mathrm{Tr}[\gamma_\mu S_h(x,0)\gamma_\nu S_l(0,x)]\\&=\sum_{\bar{x}}e^{-\imath\bar{p}\cdot\bar{x}}\ \mathrm{Tr}[\gamma_\mu S_h(x,0)\gamma_\nu\gamma_5 S_l^\dagger(x,0)\gamma_5]\end{aligned} \tag{4.25}$$

These can be evaluated using the precalculated light-quark propagators so only a single heavy-quark inversion is needed.

4.4 Correlator Ratios

To extract the required matrix element from (4.11) we form a ratio of the three-point correlator and both two-point correlators. The vector meson matrix element in the three-point correlator can be written as a numerical factor times a polarisation vector

$$\langle B^*(p',\lambda)|B^*_\mu(0)|0\rangle=Z^{1/2}_{B^*}\epsilon^\lambda_\mu. \tag{4.26}$$

We can then perform polarisation-sums over this vector, and the polarisation vectors that appear in the form factor decomposition. In Euclidean space the formula for polarisation sums is

$$\sum_{\lambda} \epsilon_{\mu}^{\lambda} \epsilon_{\nu}^{\lambda} = \delta_{\mu\nu} - \frac{p_{\mu} p_{\nu}}{p^2}. \tag{4.27}$$

If we set both the vector and pseudoscalar momenta to zero in equation (4.11), such that $\bar{q} = \bar{p} = \bar{p}' = 0$ and $q^2 = q_0^2 = (m_{B^*} - m_B)^2 \approx 0$, we can see from equation 4.5 that the only form factor accessible is A_1. Therefore we form the ratio:

$$R_1 = \frac{C^{(3)}_{i,i}\left(t_x, t_y; \bar{p} = 0, \bar{p}' = 0\right) Z_B^{1/2} Z_{B^*}^{1/2}}{C^{(2)}_{BB}\left(t_y; \bar{p} = 0\right) C^{(2)}_{B^*{}_i B^*{}_i}\left(T - t_x; \bar{p} = 0\right)} = (m_{B^*} + m_B) A_1(q_0^2) \tag{4.28}$$

which is valid for $i = 1, 2, 3$ meaning we can average on i. To access the other form factors we need to inject a unit of momentum, such that $\bar{q} = \bar{p} = (1, 0, 0) \times 2\pi/L$ and $\bar{p}' = 0$. Following the notation from [107], we define the ratios

$$R_2 = \frac{C^{(3)}_{1,0}\left(t_x, t_y; \bar{p} \neq 0, \bar{p}' = 0\right) Z_B^{1/2} Z_{B^*}^{1/2}}{C^{(2)}_{BB}\left(t_y; \bar{p} = 0\right) C^{(2)}_{B^*{}_2 B^*{}_2}\left(T - t_x; \bar{p} \neq 0\right)} = \sum_{\lambda} \langle B(p'|A_0|B^*(p,\lambda)\rangle \epsilon_1^{\lambda} \tag{4.29}$$

$$R_3 = \frac{C^{(3)}_{1,1}\left(t_x, t_y; \bar{p} \neq 0, \bar{p}' = 0\right) Z_B^{1/2} Z_{B^*}^{1/2}}{C^{(2)}_{BB}\left(t_y; \bar{p} = 0\right) C^{(2)}_{B^*{}_2 B^*{}_2}\left(T - t_x; \bar{p} \neq 0\right)} = \sum_{\lambda} \langle B(p'|A_1|B^*(p,\lambda)\rangle \epsilon_1^{\lambda} \tag{4.30}$$

where the polarisation vectors shown come from the vector matrix elements Z_{B^*}. The result of the polarisation sums is complicated and given in detail in Appendix A. Finally, we define

$$\begin{aligned} R_4 &= \frac{C^{(3)}_{2,2}\left(t_x, t_y; \bar{p} \neq 0, \bar{p}' = 0\right) Z_B^{1/2} Z_{B^*}^{1/2}}{C^{(2)}_{BB}\left(t_y; \bar{p} = 0\right) C^{(2)}_{B^*{}_2 B^*{}_2}\left(T - t_x; \bar{p} \neq 0\right)} = \sum_{\lambda} \langle B(p'|A_2|B^*(p,\lambda)\rangle \epsilon_2^{\lambda} \\ &= (m_{B^*} + m_B) A_1(q^2). \end{aligned} \tag{4.31}$$

which is equivalent to R_1 but for larger q^2. These ratios allow access to the form factor A_2 through

$$\frac{A_2}{A_1} = \frac{(m_{B^*} + m_B)^2}{2 m_B^2 q_1^2} \left[-q_1^2 + E_{B^*}(E_{B^*} - m_B) - \frac{m_{B^*}^2 (E_{B^*} - m_B)}{E_{B^*}} \frac{R_3}{R_4} - i \frac{m_{B^*}^2 q_1}{E_{B^*}} \frac{R_2}{R_4} \right]. \tag{4.32}$$

The ratio in equation (4.32) is obtained at a non-zero value of q^2 and needs to be extrapolated. However, this only contributes to the coupling suppressed by the ratio $(m_{B^*} - m_B)/(m_{B^*} + m_B)$, so any uncertainty this introduces should be small. The form factor A_1 is also obtained at a non-zero q^2, but is significantly closer to zero. If we define

functions G_1 and G_2

$$\begin{aligned} G_1(q^2) &= (m_{B^*} + m_B)A_1(q^2), \\ G_2(q^2) &= (m_{B^*} - m_B)A_2(q^2), \end{aligned} \tag{4.33}$$

we can write the coupling as $G_1(0)$ plus a small correction from the ratio G_2/G_1.

$$g_{B^*B\pi} = \frac{Z_A}{f_\pi} G_1(0) \left(1 + \frac{G_2(0)}{G_1(0)}\right) \tag{4.34}$$

$$g_b = \frac{Z_A}{2m_B} G_1(0) \left(1 + \frac{G_2(0)}{G_1(0)}\right) \tag{4.35}$$

The factor Z_A in equations (4.34, 4.35) is the local axial vector current renormalisation factor, which arises because we do not work with the full DWF conserved current.

4.5 Axial Current Renormalisation

For domain wall fermions there is a single unique vector transformation that gives rise to a conserved 4d vector current

$$\mathcal{V}^a_\mu(x) = \sum_{s=0}^{L_s-1} j^a_\mu(x,s), \tag{4.36}$$

where

$$j^a_\mu(x,s) = \frac{1}{2}\left[\bar\psi(x+\hat\mu,s)(1+\gamma_\mu)U^\dagger_{x,\mu}t^a\psi(x,s) - \bar\psi(x,s)(1-\gamma_\mu)U_{x,\mu}t^a\psi(x+\hat\mu,s)\right]. \tag{4.37}$$

Furthermore, there are a number of equivalent transformations that produce the conserved 4d axial vector current

$$\mathcal{A}^a_\mu(x) = \sum_{s=0}^{L_s-1} \mathrm{sgn}\left(s - \frac{L_s-1}{2}\right) j^a_\mu(x,s). \tag{4.38}$$

These both reduce to the standard continuum forms for $a \to 0$. For practical purposes these conserved currents are unwieldy to work with, so instead it is normal to use local versions of the currents

$$A_\mu(x) = \bar q(x)t^a\gamma_\mu\gamma_5 q(x), \quad V^a_\mu(x) = \bar q(x)t^a\gamma_\mu q(x) \tag{4.39}$$

which are related to (4.36) and (4.38) by multiplicative renormalisation factors.

$$Z_A A^a_\mu = \mathcal{A}^a_\mu, \quad Z_V V^a_\mu = \mathcal{V}^a_\mu \tag{4.40}$$

In this work we use the local axial current and renormalise it using the factors calculated in [115]. These are obtained by looking at the ratio

$$Z_A = \frac{\sum_x \langle \mathcal{V}_4(x) P(0) \rangle}{\sum_x \langle V_4(x) P(0) \rangle}, \tag{4.41}$$

where $P(0)$ is a pseudoscalar interpolating operator. The ratio of the vector currents is used, but with exact chiral symmetry Z_A and Z_V are equal [116]. The values used are given in table 4.2.

Ensemble	a (fm)	Z_A
24^3	≈ 0.11	0.7019(26)
32^3	≈ 0.08	0.7396(17)

Table 4.2: Axial current renormalisation factors used in this work

4.6 Numerical Calculation

4.6.1 Ensemble Properties

We perform our calculation on RBC/UKQCD collaboration ensembles generated with the Iwasaki gauge action, and the 2+1 flavour domain wall fermion action [115, 117]. The configurations are generated with two degenerate light-quarks and a single near-physical mass strange quark. The use of the DWF and Iwasaki actions together gives good chiral properties and allows the tunnelling between topological sectors necessary to achieve good sampling during ensemble generation [118]. The configurations are generated with a domain wall height of $M_5 = 1.8$ and a fifth dimensional extent of $L_S = 16$. With these parameters the explicit chiral symmetry breaking is small, quantified by a residual mass of $m^{24}_{res}a = 0.003$ and $m^{32}_{res}a = 0.0007$ on the 24^3 and 32^3 ensembles respectively. The residual mass is the small additive mass renormalisation that appears due to the finite extent of the fifth dimension in the domain wall fermion formulation. We use ensembles with two different lattice spacings, but both with approximately equal spatial extent. The coarser ensembles have 24 points in the spatial directions, and 64 point in the temporal direction. The finer lattices have 32 points in the spatial directions and 64 points in the temporal direction. These have physical lattice spacings of $a \approx 0.11$fm and $a \approx 0.086$fm respectively. The availability of two lattice spacings will help us to take a continuum limit of physical quantities. Table 4.3 lists the details of the configurations used in this study. The coarser 24^3 ensembles have been generated with three different light sea quark masses of m_l=0.005, 0.010 and 0.020 in lattice units and the 32^3 ensembles at m_l=0.004, 0.006, 0.008. These correspond to pion masses down to approximately m_π=290 MeV. Both ensembles were generated with near-physical strange quark masses, we discuss the implications of the deviation from the physical values in section 4.8.8.

The lattice scale was set in [115] from the Ω mass and has also been set in [119] from the $\Upsilon(2S) - \Upsilon(1S)$ mass splitting. Both results are consistent and give a^{-1}=1.729(25) GeV on the 24^3 ensemble and a^{-1}=2.281(28) GeV on the 32^2 ensemble. On the 24^3 lattices we use a single source position for all our measurements, whereas on the 32^3 lattice, for which we have fewer gauge configurations, we make measurements at two source positions. On all ensembles we perform a random translation on the gauge field before performing a measurement. This allows us to make measurements on configurations separated by less trajectories, and reduce the effect of auto-correlations.

$L^3 \times T$	a(fm)	$m_l a$	$m_s a$	m_π(MeV)	#Configs	Sources
$24^3 \times 64$	0.11	0.005	0.04	329	1636	1
$24^3 \times 64$	0.11	0.010	0.04	422	1419	1
$24^3 \times 64$	0.11	0.020	0.04	558	345	1
$32^3 \times 64$	0.08	0.004	0.03	289	628	2
$32^3 \times 64$	0.08	0.006	0.03	345	889	2
$32^3 \times 64$	0.08	0.008	0.03	394	544	2

Table 4.3: Ensemble properties. All ensembles are generated using 2+1 flavours of Domain Wall Fermions and the Iwasaki gauge action. The fifth dimensional extent of both lattices is $L_S = 16$ and the domain wall height $M_5 = 1.8$, corresponding to a residual chiral symmetry breaking of $m_{res}^{24} a = 0.003$, $m_{res}^{32} a = 0.0007$.

4.6.2 Quark Sources

We apply Gaussian smearing to the heavy-quark propagators to improve overlap with the B and B^*-meson ground-states. As discussed in section 3.5.5, by using extended sources we can mimic the mesons' wave-functions and achieve better overlap with their groundstates. Following experience gained from the RHQ action tuning calculation [3], we use a gauge covariant Gaussian smearing function [89, 90], as defined in section 3.5.5, and the parameters listed in table 4.4. Here N is the number of smearing iterations and σ is related to the Gaussian's root-mean-squared radius by $r_{rms} \approx \sqrt{3}\sigma/2$ in the free-field case. We do not use smearing on the light-quark propagators, as these are precalculated with point sources. In figures 4.4 and 4.5 we show the effect of smearing on a test calculation of the B-meson effective mass, using 550 configurations from the 24^3, $m_l = 0.005$ ensemble. These plots clearly show that the longest plateau is seen when applying the smearing only to the heavy-propagator source. Therefore, in this work we chose to apply a smeared source and a point sink to all heavy-quark propagators.

4.6.3 Propagator Generation

The generation of all heavy-quark propagators and the calculation of traces was carried out using the Chroma software system [120] on the University of Southampton's Iridis

Ensembles	a (fm)	r_{rms} (fm)	σ	N
24^3	≈0.11	0.777	10.36	170
32^3	≈0.086	0.777	7.86	100

Table 4.4: Parameters used to apply covariant Gaussian smearing to all heavy-quark propagator sources calculated in this work

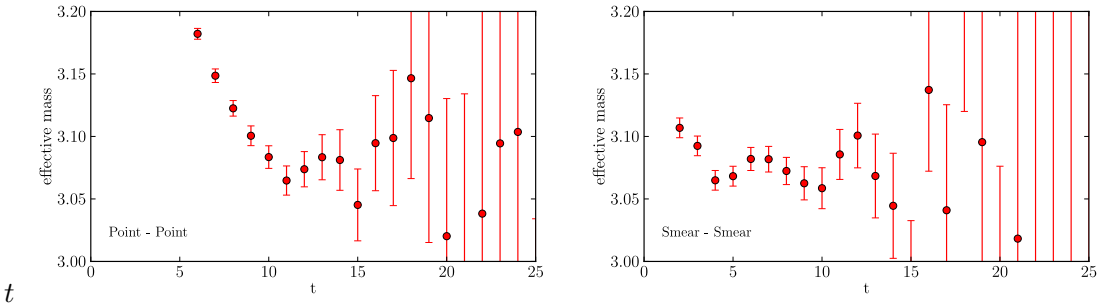

Figure 4.4: B-meson two-point functions with no smearing on the heavy propagator (left) and Gaussian smearing at both ends (right). In both cases the light-quark propagator has a point source and sink. Calculated using 550 configurations of the 24^3 $m_l = 0.005$ ensemble.

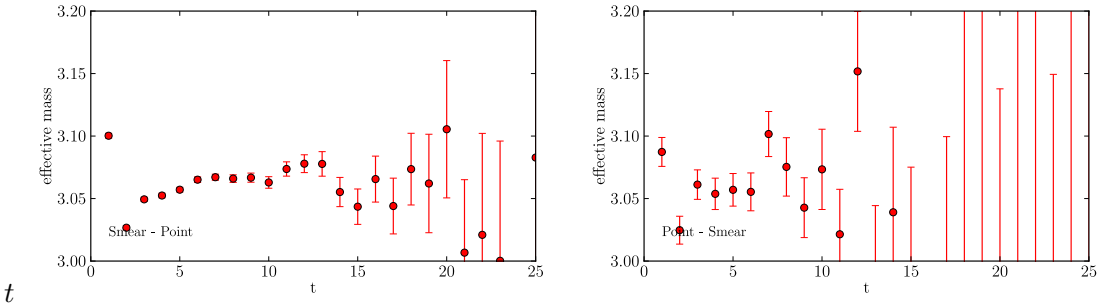

Figure 4.5: B-meson two-point functions with a smeared source and point sink on the heavy propagator (left) and point source and smeared sink (right). In both cases the light-quark propagator has a point source and sink. Calculated using 550 configurations of the 24^3 $m_l = 0.005$ ensemble.

3 Cluster, and the JPsi cluster at Fermi Lab. We calculated the propagators using the tuned vales of the RHQ parameters calculated in [3], and listed in table 4.5. The inversions were carried out using the conjugate gradient algorithm, running to a residual of 10^{-45}. We had concerns that because the heavy propagators become numerically very small for large times a standard CG stopping criterion might not sufficiently converge all elements. Therfore we ran tests using a time-slice-by-time-slice stoping criterion, and found that this was equivalent to demanding a smaller (10^{-45}) norm-squared residual.

	$m_o a$	c_p	ξ
a≈0.11 fm	8.45(6)(13)(50)(7)	5.8(1)(4)(4)(2)	3.10(7)(11)(9)(0)
a≈0.056 fm	3.99(3)(6)(18)(3)	3.57(7)(22)(19)(14)	1.93(4)(7)(3)(0)

Table 4.5: Tuned RHQ parameters for b-quarks and their uncertainties, these are statistical, heavy-quark discretisation effects, lattice scale uncertainty, and experimental uncertainties respectively [3].

4.7 Results

4.7.1 Three-Point Function

Figure 4.6 show the three-point correlators for two different values of t_y, the position of the B-meson interpolator. The plots show a cosh-like form, with a peak at $t_x = t_y$, corresponding to when the mesons are created and annihilated at the same lattice point. More curiously the cosh-like form of the correlators is translated in the x-axis by an amount equal to t_y. Naively, looking at the expected form for the three-point correlators in (4.11) we would expect the only effect of changing t_y to be a constant scaling of the correlator. This should not cause a translation along the x-axis. To solve this puzzle it is

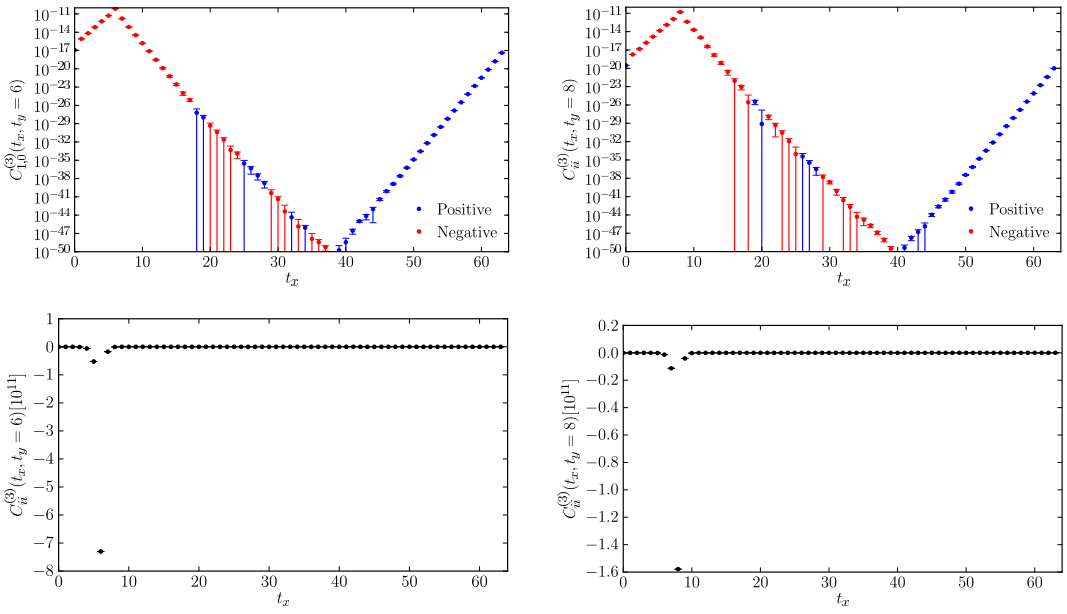

Figure 4.6: The three-point correlation functions summed over all spatial indices for $t_y = 6$ (left) and $t_y = 8$ (right). The top plots are on a log scale, whereas the lower plots are on a linear scale. The point where the correlation function blows-up is where the meson creation and annihilation operators are on the same lattice space.

necessary to consider all the possible contributions to the correlators that arise when you take into account the periodicity of the lattice. When one performs the Wick contraction

of the correlation function in equation (4.11) the result is equivalent to that from different orderings of the operators. For instance, when we consider the operator that produces a B^*-meson to be before the axial current in time, it can also be considered to be after the axial current. In figures 4.7 and 4.8 we show the different arrangements of operators that can contribute. These are separated into $t_x < t_y$ in figure 4.7 and $t_x \geq t_y$ in figure 4.8. There are, of course, even more arrangements if you consider $t+nT \; \forall \; n \in \mathbb{Z}$, but for increasing n these become more and more suppressed as the states propagate further in time. Each of the arrangements is labeled by a capital roman letter A–H and their time dependence is given by assuming immediate ground-state dominance. The arrangement that gives the desired matrix element is $C(t_x, t_y)$ in figure 4.7. To estimate how much each arrangement contributes to the matrix element we are looking for, we plot all the contributions by making the approximation that each matrix element is unity. We can then choose sensible values for the meson masses and sum the effect of each arrangement. The result closely matches what is seen for the real three-point function (see figure 4.6), a cosh-like shape shifted along the x-axis by t_y. We also see a large peak at $t_x = t_y$. This helps confirm the data that we have calculated makes sense, but we would also like to confirm that the desired matrix element can be accessed by looking at the correlator for large t_x. To ascertain this we have plotted the individual relative contributions to Fig. 4.9 separately. We can see in figure 4.10 that the contribution C dominates for large t_x. In fact, at t_x=50 (typical fit-ranges are 50–56) it is $\approx 10^{30}$ times larger than the next biggest contribution. This argument could be flawed if the matrix elements are extremely large for the other unwanted contributions, however this seems extremely unlikely. The next-largest contribution according to the time dependence corresponds to a pion decaying into a B and B^*-meson. The matrix element for this process must be vanishingly small.

4.7.2 Two-Point Functions

Figure 4.11 show effective mass plots for the vector and pseudoscalar mesons, along with a fit line and one sigma statistical error band. The fits are performed by minising an uncorrelated χ^2 function using the Minuit algorithm [121]. We show a constant fit to the effective mass for clarity, although the actual fits are performed to the raw correlators using an exponential fit function.

$$f(t; E, A) = \frac{A}{2E} e^{-Et} \tag{4.42}$$

Owing to the large masses the exponentials have a very fast fall off making it unnecessary to consider the backward propagating parts by using a cosh fit function. The two-point correlators are used both in direct fits using Eq. 4.42, to find the amplitudes Z_B and Z_{B^*}, and also to divide the three-point correlators to form the ratios R_1–R_4. The effective

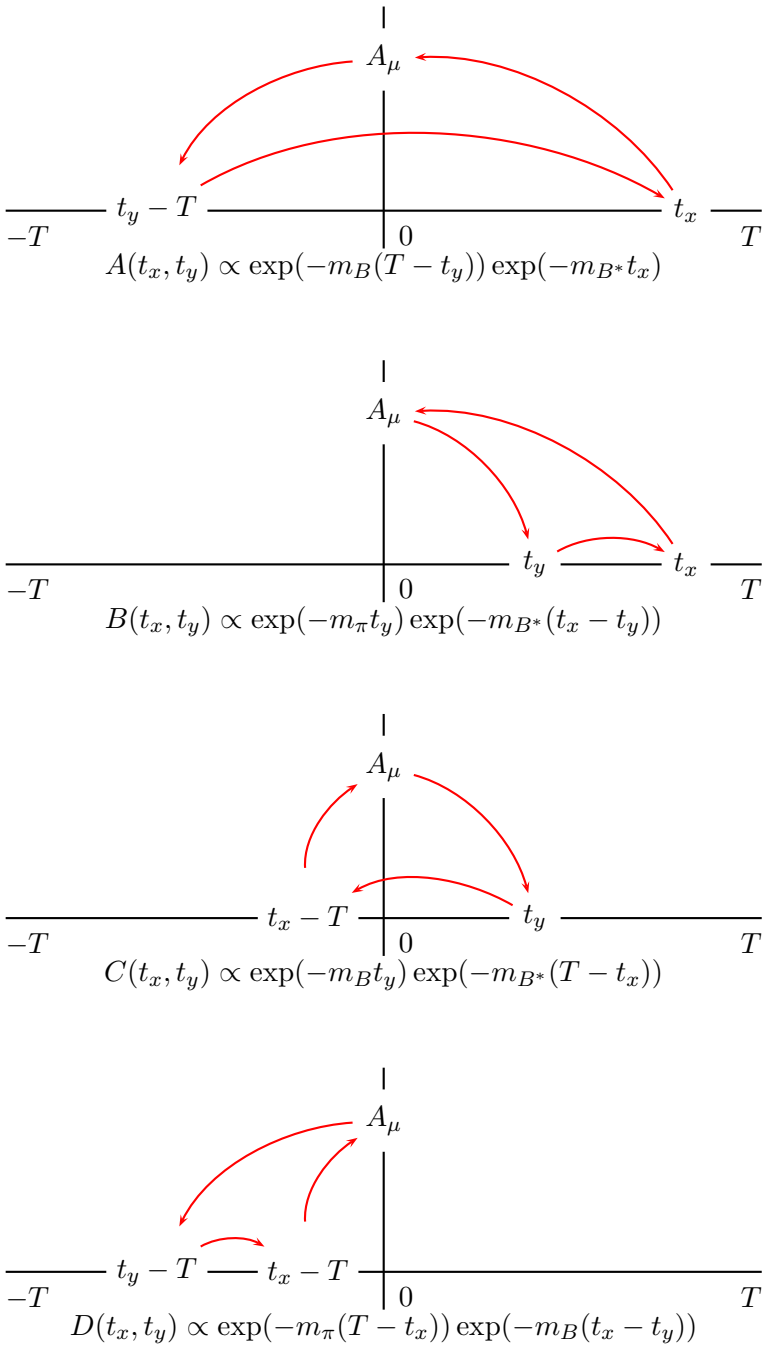

Figure 4.7: Contributions to the three-point correlator for $t_x > t_y$

mass plots at zero momentum, and the first non-zero momentum, on the 24^3, $m_l = 0.005$ and 32^3, $m_l = 0.006$ ensembles are shown in Figures 4.11, 4.12, 4.13 and 4.14.

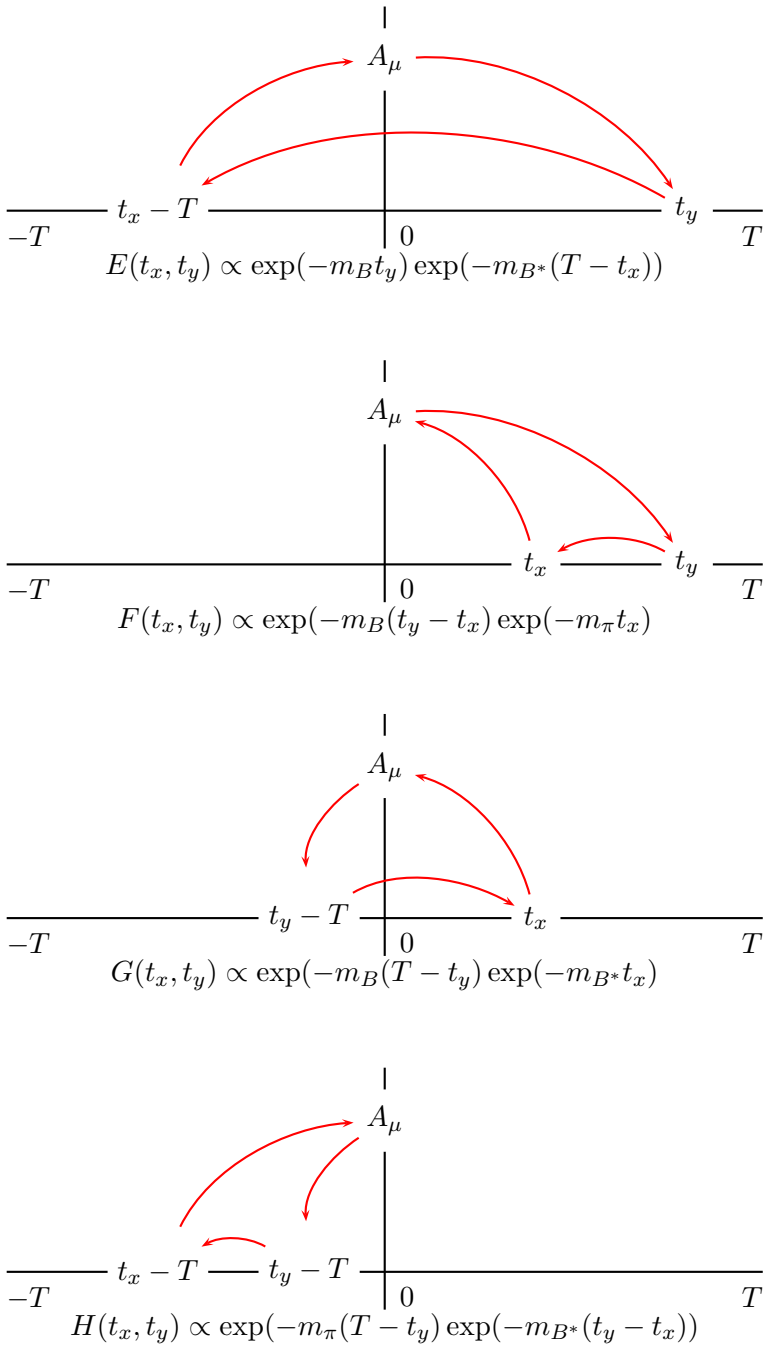

Figure 4.8: Contributions to the three-point correlator for $t_x \leq t_y$

4.7.3 Ratios

We evaluate the ratios in equations (4.28, 4.29, 4.30 and 4.31), and calculate g_b from equation (4.35) underneath a single elimination jack-knife. This correctly propagates the statistical errors from each correlator through the calculation, taking into account that each measurement is correlated. The configurations are each translated by a random

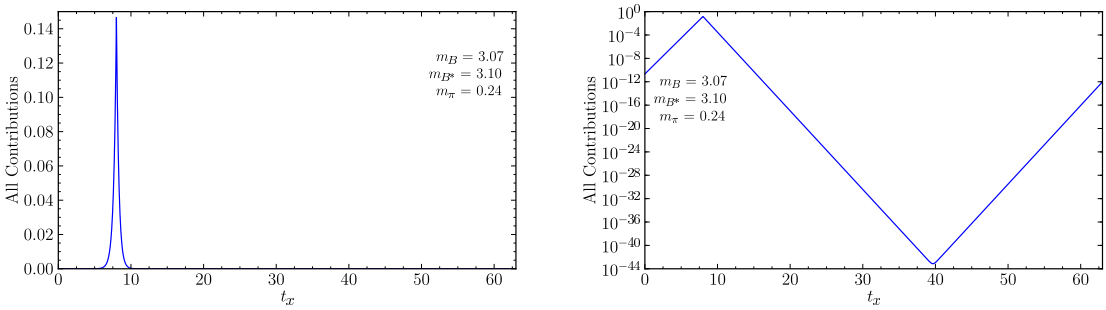

Figure 4.9: The sum of all contributions to the three-point correlator as shown in figures 4.7 and 4.8 assuming immediate ground-state dominance, and setting all the matrix elements to unity. The shape closely matches what is seen in the actual calculation of the three-point function (see Figure 4.6).

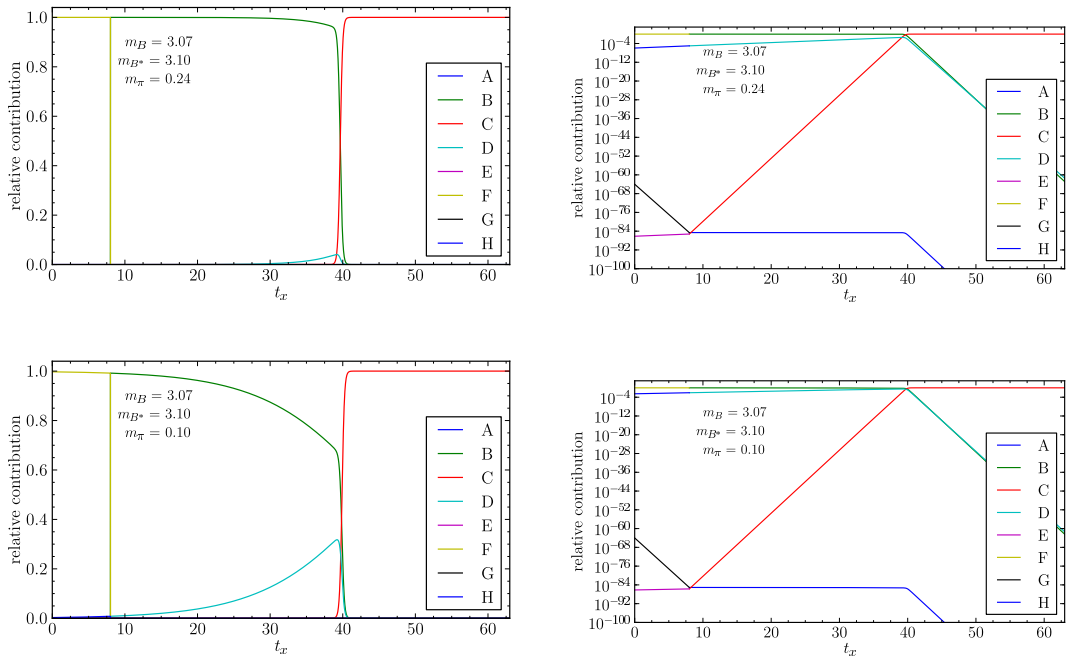

Figure 4.10: Relative size of the eight contributions to the three-point function arising due to the periodicity of the lattice. To extract the correct matrix element the contribution of interest is C. This contribution dominates for large t_x.

vector, minimising any auto-correlations between subsequent measurements. Figure 4.15 shows g_b from the lightest ensemble on each lattice plotted against the jack-knife bin size. There is no effect from varying the bin size on either ensemble so we conclude that the auto-correlation time is less than the separation of measurements and hence we use a block size of one in the jack-knife. On each jack-knife block we fit the two-point functions and extract the amplitudes Z_B and Z_{B^*} from Eqs (4.12) and (4.13). The three-point correlators are then averaged over any equivalent indices (for R_1 specifically) and

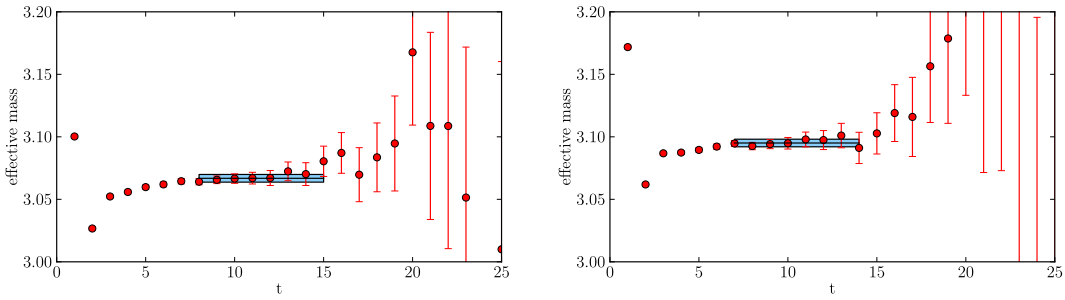

Figure 4.11: B-meson effective mass (left) at zero momentum and B^*-meson effective mass at zero momentum, both on the 24^3, $m_l = 0.005$ ensemble

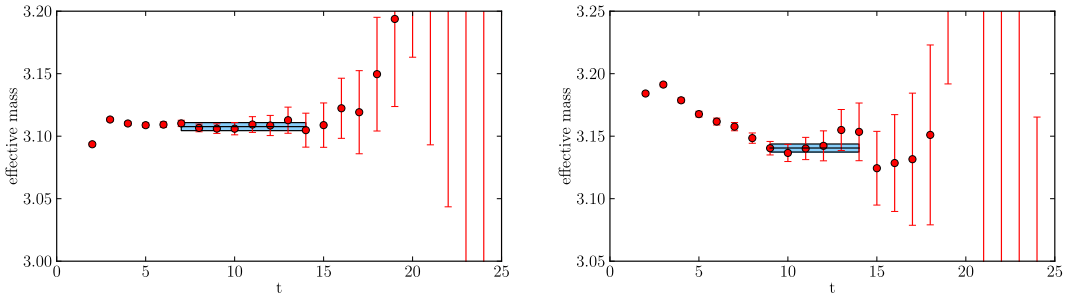

Figure 4.12: B^*-meson effective mass/energy (left) at the first non-zero momentum and B^*-meson effective mass/energy at the second non-zero momentum, both on the 24^3, $m_l = 0.005$ ensemble

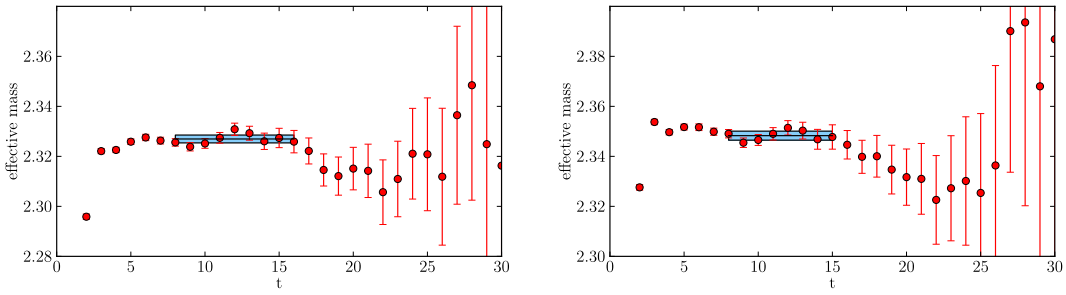

Figure 4.13: B-meson effective mass (left) at zero momentum and B^*-meson effective mass at zero momentum, both on the 32^3, $m_l = 0.006$ ensemble

divided by both two-point functions. The ratios are then multiplied by the amplitudes Z_B and Z_{B^*} with their statistical errors added in quadrature. Finally, we fit the resulting ratios to a constant by minimising a χ^2 function. This procedure is completed on each jack-knife block and then the ensemble average taken. The statistical error is calculated according to Eq. (3.77). We choose the fit ranges as consistently as possible over each lattice, meaning we apply the same fit-range for a particular ratio to every valence mass. We choose a different fit range for the fine and coarse ensembles. Examining the ratio R_1 for different choices of t_y on the 24^3, $m_l = 0.05$ ensemble (Figure 4.16) we see the best signal for $t_y = 6$. We therefore use this value for every 24^3 ensemble and choose $t_y = 8$ on the 32^3 ensemble as this corresponds to the same physical distance. Figure 4.17

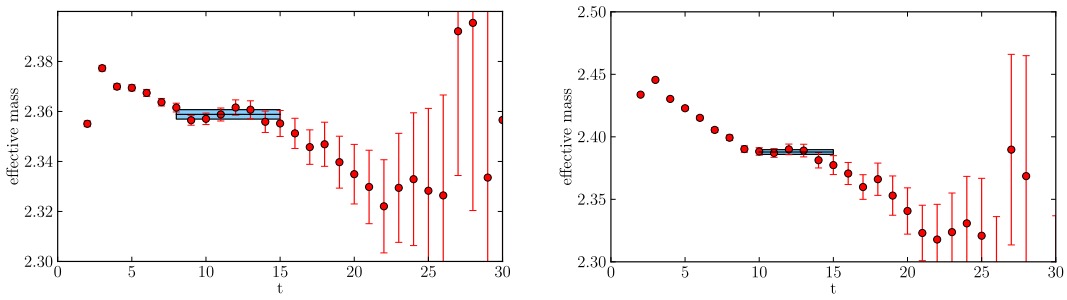

Figure 4.14: B^*-meson effective mass/energy (left) at the first non-zero momentum and B^*-meson effective mass/energy at the second non-zero momentum, both on the 32^3, $m_l = 0.006$ ensemble

shows the ratios R_1, R_2 and R_3 on the 24^3 m_l=0.005 ensemble with the best-fit and error band also shown. We need to calculate the form factor A_1 at $q^2 = 0$, however the ratio R_1 only gives us it at $q_0^2 = (m_{B^*} - m_B)^2$. We also calculate R_4 which also gives A_1, but at a larger q^2 (we calculate R_4 at two momenta). Figure 4.18 shows the q^2 dependence of the form factor. It shows that attempting to extrapolate to q^2=0 would not change $A_1(q^2)$ within statistical errors. Therefore we assume $A_1(q_0^2) = A_1(0)$. Also shown in figure 4.18 is the ratio $G_2/G_1(q^2)$. We perform a linear extrapolation of this quantity to $q^2 = 0$ using the two data points. The effect of the ratio $G_2/G_1(0)$ is to make a correction of <1% to g_b, therefore any uncertainty from the extrapolation should be negligible.

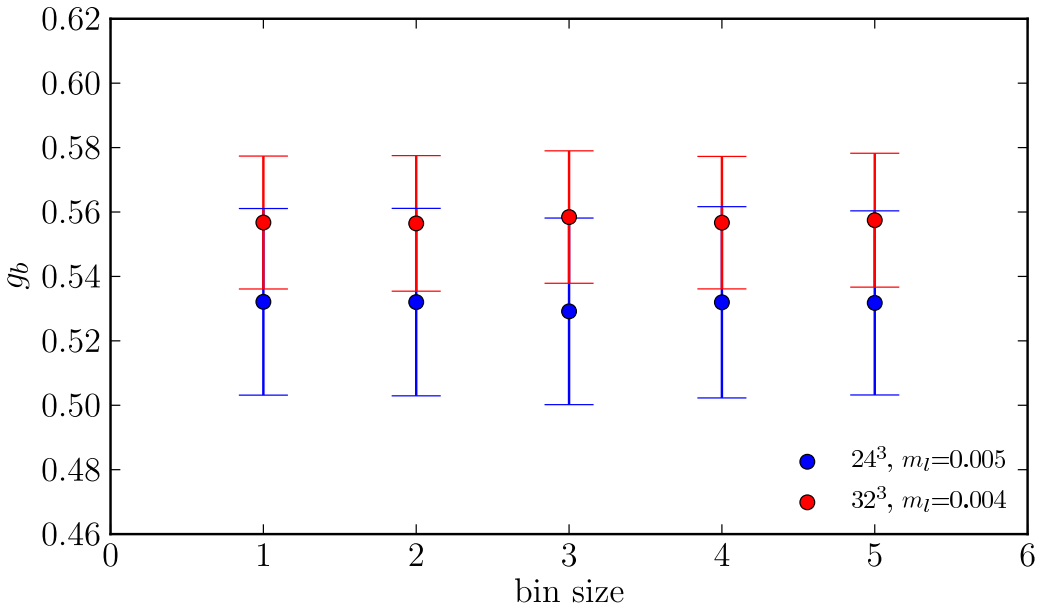

Figure 4.15: The coupling g_b with jack-kife errors plotted against the bin size. No effect is seen, so we conclude each configuration is suitably uncorrelated.

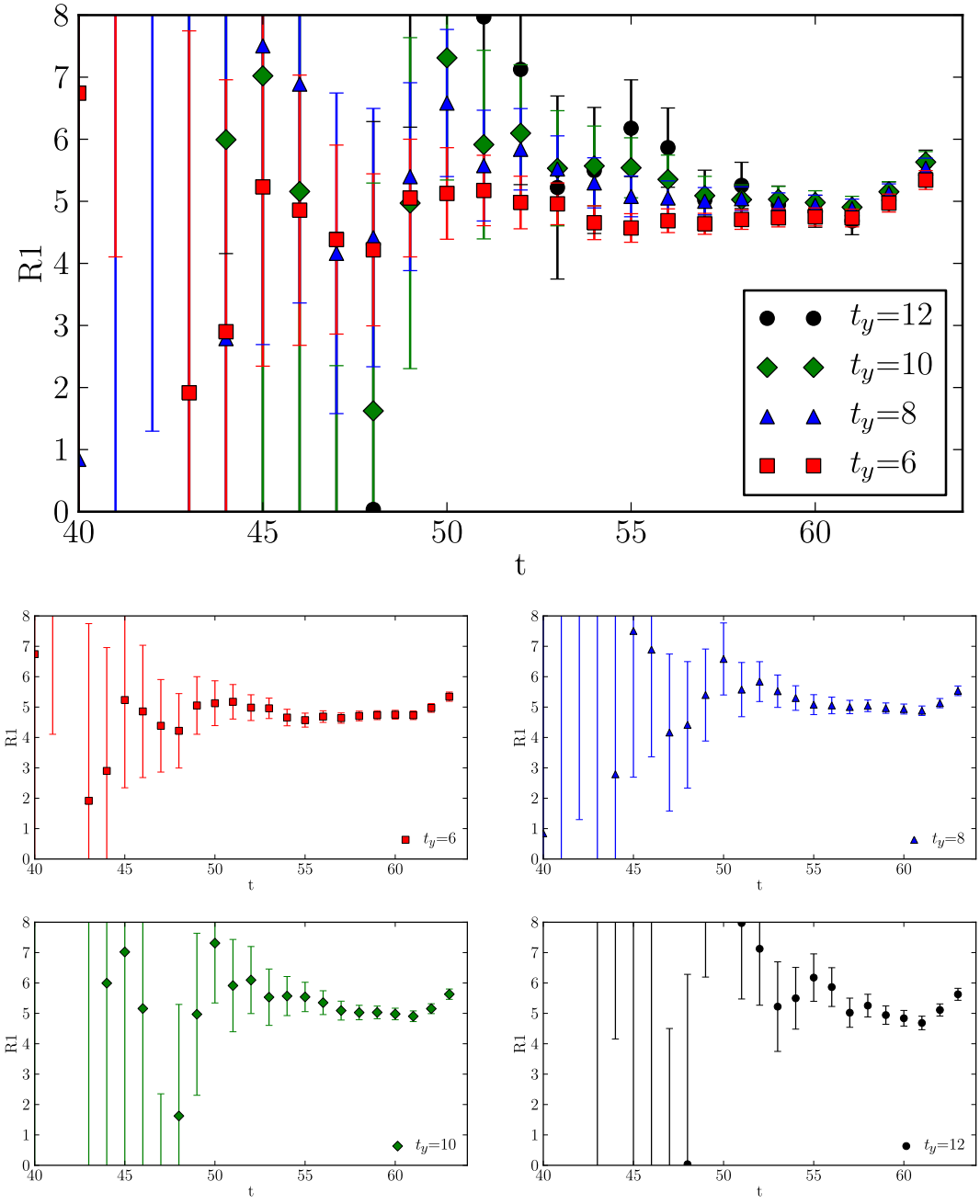

Figure 4.16: The ratio R_1 evaluated for different values of t_y on the 24^3, $m_l = 0.005$ ensemble. The longest plateau is seen for the value t_y=6. We show the region in the latter half of the lattice where we expect to see the signal.

4.7.4 Chiral and Continuum extrapolation

Our calculation is performed with light-quark masses heavier than in nature, corresponding to pions upwards of 290 MeV. This means that to have a physical result we will need to perform an extrapolation down to the chiral point. We can be guided in this by using HMχPT, as calculations of the axial current matrix element in the effective theory, beyond tree level, have a dependence on the pion mass squared. Detmold, Lin

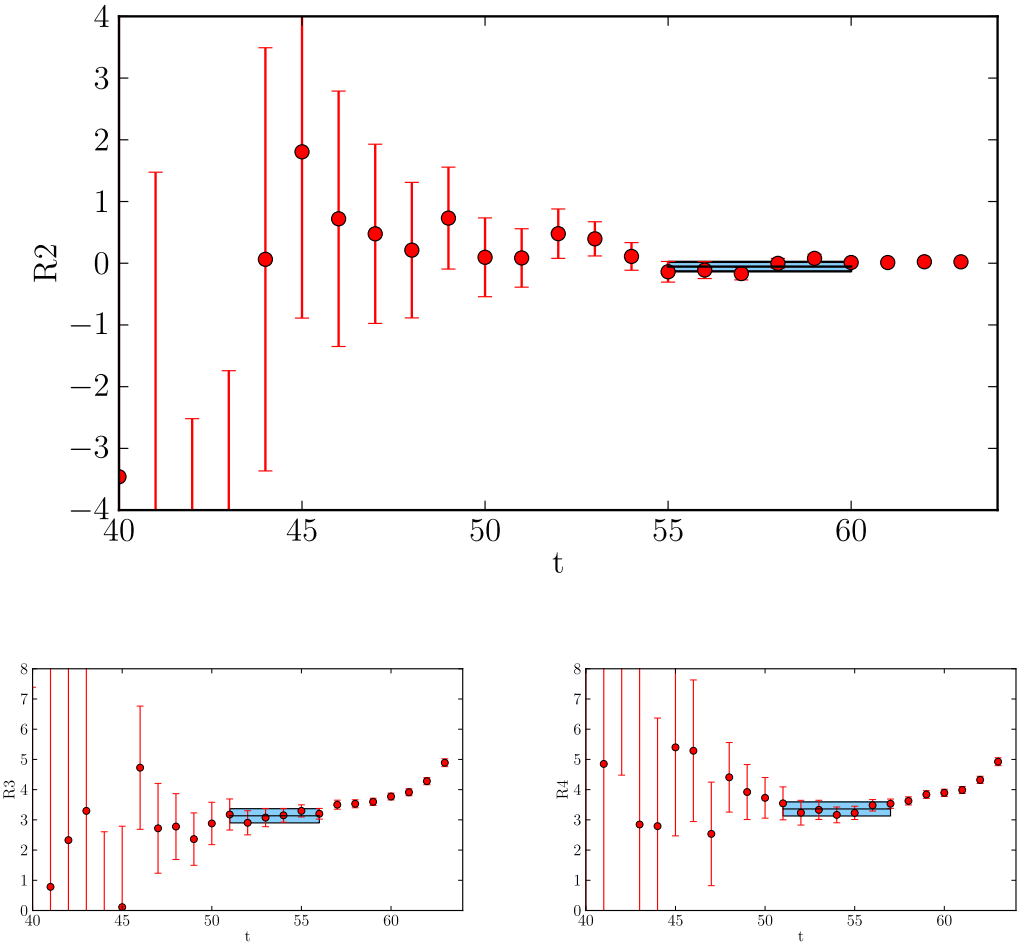

Figure 4.17: The ratios R_1, R_2 and R_3 calculated on the 24^3, $m_l = 0.005$ ensemble

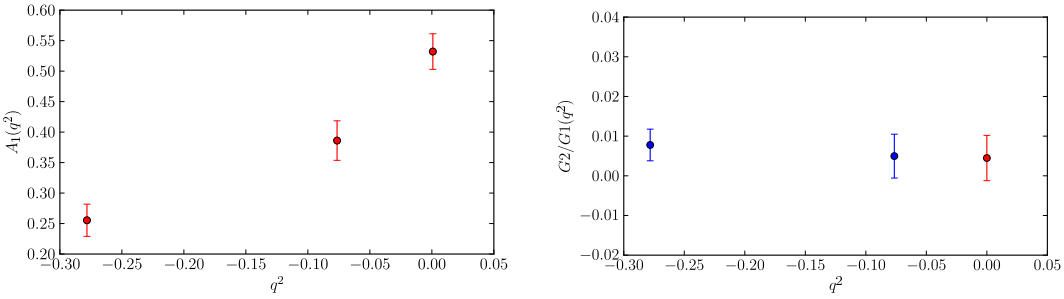

Figure 4.18: The q^2 dependence of the form factor A_1 (left) and the linear extrapolation of the ratio G_2/G_1 to $q^2 = 0$ on 24^3, $m_l = 0.005$ ensemble

and Meinel [109] have carried out this calculation in HMχPT for both the SU(2) and the SU(3) case, with both unitary and partially-quenched sea quarks. For the SU(2) case, with unitary masses they give the result

$$g = g_0 \left(1 - \frac{2(1+2g_0^2)}{(4\pi f_\pi)^2} m_\pi^2 \log \frac{m_\pi^2}{\mu^2} + \alpha m_\pi^2\right). \tag{4.43}$$

		Ensemble					
		24^3	24^3	24^3	32^3	32^3	32^3
	$\vec{p}a[\pi/L]$	0.005	0.010	0.020	0.004	0.006	0.008
B fit-range	(0,0,0)	$8-16$	$8-16$	$8-16$	$8-17$	$8-17$	$8-17$
B^* fit-range	(0,0,0)	$7-15$	$7-15$	$7-15$	$8-16$	$8-16$	$8-16$
R_1 fit-range	(0,0,0)	$50-58$	$50-58$	$50-58$	$50-58$	$50-58$	$50-58$
B^* fit-range	(1,0,0)	$7-15$	$7-15$	$7-15$	$8-16$	$8-16$	$8-16$
R_2 fit-range	(1,0,0)	$51-60$	$51-60$	$51-60$	$47-55$	$47-55$	$47-55$
R_3 fit-range	(1,0,0)	$50-56$	$50-56$	$50-56$	$46-55$	$46-55$	$46-55$
R_4 fit-range	(1,0,0)	$50-57$	$50-57$	$50-57$	$47-56$	$47-56$	$47-56$
B^* fit-range	(1,1,0)	$9-15$	$9-15$	$7-15$	$10-16$	$10-16$	$10-16$
R_2 fit-range	(1,1,0)	$51-60$	$51-60$	$51-60$	$47-55$	$47-55$	$47-55$
R_3 fit-range	(1,1,0)	$49-55$	$49-55$	$49-55$	$46-55$	$46-55$	$46-55$
R_4 fit-range	(1,1,0)	$51-57$	$51-57$	$51-57$	$46-54$	$46-54$	$46-54$

Table 4.6: Fit ranges used for the two-point functions and the ratios. For non-zero momenta equivalent combinations are averaged.

which is NLO in the chiral expansion, but only leading order in the heavy-quark expansion. This means that strictly it is only applicable for static heavy-quarks. We will discuss the implications of this in the section on systematic errors. They point out that this is the correct chiral formula for g_b, and it differs by a chiral log of f_π to the formula for $g_{B^*B\pi}$, due to the factor f_π that appears in the relation between the two couplings. The term containing the chiral log comes from the one-loop intergrals and the term with the α coefficient corresponds to the NLO analytic terms. The analytic terms should cancel the renormalisation scale dependence, which we confirmed explicitly by fitting with a range of μ^2. We have added a quadratic term in the lattice spacing to account for discretisation effects. The light-quark and gluon actions are $\mathcal{O}(a)$ improved, so this should account for leading order effects. We cannot model any higher order effects with only two lattice spacings. Our complete fit function, including the lattice scale depenence is given by

$$g = g_0 \left(1 - \frac{2(1+2g_0^2)}{(4\pi f_\pi)^2} m_\pi^2 \log \frac{m_\pi^2}{\mu^2} + \alpha m_\pi^2 + \beta a^2\right). \tag{4.44}$$

Discretisation effects arising from the heavy-quark action are not so straight forward to account for, and if large could change our assumption of leading a^2 effects. Therefore we will treat them separately in the next section. Figure 4.19 shows the combined chiral and continuum extrapolation down to the physical point. We fit each ensemble by minimising an uncorrelated χ^2 and find a surface in parameter space (g, α, β) where $\Delta\chi^2$=3.50. This correponds to a one-sigma confidence limit for three parameters [122]. We then find the extremes of the fit function on this surface, which are represented by the green shaded regions in Figure 4.19. To carry out the fit we use the PDG value of the pion decay constant f_π=130.40(04)(20) MeV [30]. The uncertainties for the axial current renormalisation factor are added in quadrature to each data point.

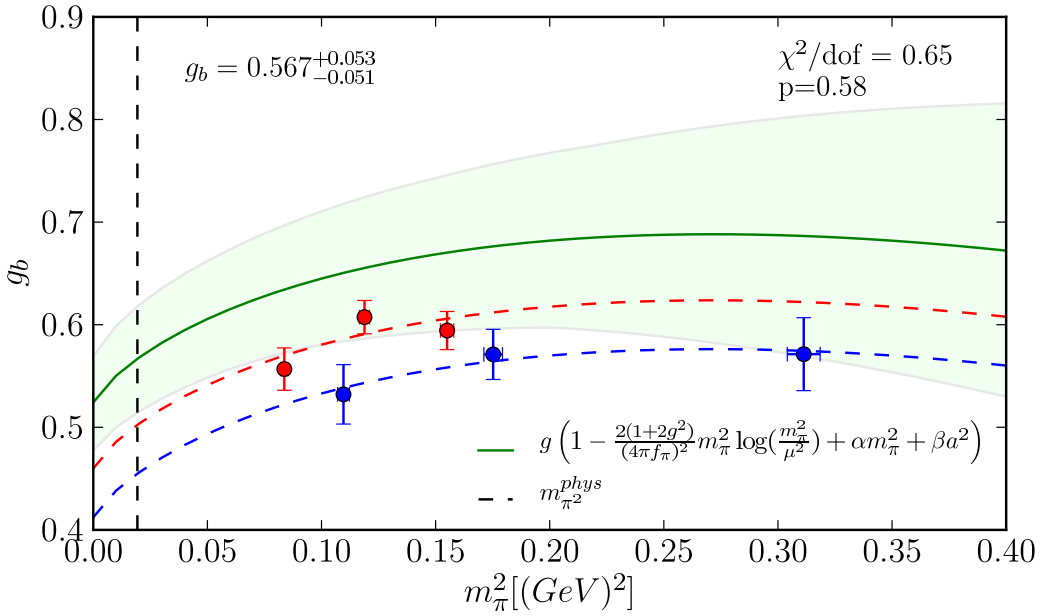

Figure 4.19: Combined chiral and continuum extrapolation to the physical point. The blue points and dashed line are the 24^3 data points and fit respectively. The red points, and dashed line correspond to the finer 32^3 ensembles. The green solid is the extrapolation to the continuum, surrounded by a one sigma error band. The point where the green line crosses the vertical dashed line corresponds to a physical pion mass. The fit function is given by Eq. (4.44).

4.8 Systematic Errors

4.8.1 $1/M_Q$ effects

The expression (4.43) for the axial vector current matrix element that we use to fit the light-quark mass dependence of our calculation is NLO in the light degrees of freedom, but only leading order in the heavy degrees of freedom. This corresponds to infinitely heavy-quarks. Our calculation is however performed at the physical b-quark mass. Intuitively we expect this not to be significant as we are using the formula only to fit the light mass dependence. Referring to previous studies [123, 124] we see that the effect of the next order in HMχPT is extra terms in the Lagrangian that can be accounted for by rescaling the coupling by two unknown parameters.

$$g \to g + \frac{1}{M_Q}(g_1 + g_2) \tag{4.45}$$

For our purposes this means that our fit parameter g contains an explicit dependence on the heavy-quark mass. This does not alter our results and shows the procedure is valid up to NLO. We therefore ascribe no systematic errors specifically to the truncation of the series in $1/M_Q$. We will however consider uncertainties present overall in the chiral extrapolation.

4.8.2 Heavy-quark discretisation errors

A discussion of cut off effects for heavy-quarks on the lattice can be tackled using an effective field theory, similar to the Symanzik approach [49]. This involves constructing an effective theory that reproduces the same physics as the lattice theory.

$$\mathcal{L}^{Lat} \doteq \mathcal{L}^{Sym} \tag{4.46}$$

The Symanzik side of the equality is QCD, plus higher order operators.

$$\mathcal{L}^{Sym} = \frac{1}{2g^2} tr\left[F_{\mu\nu}F^{\mu\nu}\right] - \bar{q}\left(\not{D} + m\right) q + \sum_i \mathcal{C}_i(g^2, ma, \mu a)\mathcal{O}_i(\mu a) \tag{4.47}$$

By identifying the relevant operators, and determining the coefficients which encode the short distance physics, it is possible to subtract from the lattice side the relevant pieces to improve the continuum limit. This is the usual improvement picture, but what about for heavy-quarks with mass m_Q? Unfortunately, for large $m_Q a$ we do not have QCD plus small corrections because some of the higher order operators, containing derivatives, produce powers of $(m_Q a)^n$, meaning the corrections are not necessarily small. However, by making field transformations we can remove these contributions at all orders. This is effectively just a reordering of the higher-order terms, but the leading order Lagrangian also changes in the process [125].

$$\mathcal{L}^{QCD} \doteq \mathcal{L}^{Sym} = \cdots - \bar{Q}\left(\gamma_4 D_4 + m_1 + \sqrt{\frac{m_1}{m_2}}\gamma\cdot\mathbf{D}\right) Q + \sum_i \mathcal{C}_i^{Cont}(g^2, m_2 a, \mu a)\mathcal{O}_i \tag{4.48}$$

Similarly we write a continuum effective theory that reproduces the matrix elements of our lattice action.

$$\mathcal{L}^{Lat} \doteq \cdots - \bar{Q}\left(\gamma_4 D_4 + m_1 + \sqrt{\frac{m_1}{m_2}}\gamma\cdot\mathbf{D}\right) Q + \sum_i \mathcal{C}_i^{Lat}(g^2, m_2 a, \mu a)\mathcal{O}_i \tag{4.49}$$

In both the above equations the ellipsis stands for the gauge part of the action. Both effective theories contain the same operators, so any mismatch between the coefficients of the operators reveals the heavy-quark discretisation errors. Otkay and Kronfeld [126] have catalogued the relevant operators according to two different power-counting schemes, NRQCD and HQET and calculated the Wilson coefficients to tree level.

The coupling g_b is proportional to the matrix elememt $\langle B^*_\mu(p)|A^\mu(q)|B(p')\rangle$ at $p = p' = q = 0$. If we write the continuum QCD action in terms of the lattice action, plus the differences between $\mathcal{L}^{Cont}$ and $\mathcal{L}^{Lat}$, then expand to first order, the expectation value we want becomes

$$\begin{aligned}
&\langle B^*_\mu(p)|A^\mu|B(p')\rangle_{Cont} \\
&\quad = \langle B^*_\mu(p)|A^\mu|B(p')\rangle_{Lat} + \int d^4x \sum_i \left(\mathcal{C}_i^{Cont} - \mathcal{C}_i^{Lat}\right) \langle B^*_\mu(p)|T\{\mathcal{O}_i(x)A^\mu(0)\}|B(p')\rangle_{Lat} \\
&\quad = \langle B^*_\mu(p)|A^\mu|B(p')\rangle_{Lat} \left[1 + \sum_i \left(\mathcal{C}_i^{Cont} - \mathcal{C}_i^{Lat}\right) \frac{\langle [B]|\mathcal{O}_i(x)|[B]\rangle}{2M_B}\right]
\end{aligned} \tag{4.50}$$

After the first line we have inserted a complete set of states between both time orderings, allowing us to factor out the original matrix element. Here $[B]$ means the sum over the B and B^*, including excited states, coming from the two different time orderings and assuming that matrix elements $\langle B|A_\mu|B\rangle$ and $\langle B^*|A_\mu|B^*\rangle$ do not contribute. As we are only calculating a small correction, and it is assumed that the excited state contributions would themselves be small, we will only consider the ground states, and treat the vector and pseudoscalars as equivalent in the powercounting.

$$g_b^{\text{error}} = g_b \sum_i \left(\mathcal{C}_i^{Cont} - \mathcal{C}_i^{Lat}\right) \sum_i \frac{\langle \mathcal{O}_i \rangle}{2M_B} \tag{4.51}$$

We can then estimate the size of the $\langle \mathcal{O}_i \rangle$ using HQET power-counting arguments. In the HQET power-counting the RHQ action is non-pertubatively tuned up to order λ, where

$$\lambda \sim a\Lambda_{QCD}, \Lambda_{QCD}/m_Q. \tag{4.52}$$

Therefore we wish to evaluate equation (4.51) for all operators of order λ^2. There are two such operators identified in [126],

$$\begin{aligned}
&\bar{h}\left\{\gamma \cdot \mathbf{D}, \alpha \cdot \mathbf{E}\right\} h, \\
&\bar{h}\gamma_4 \left(\mathbf{D} \cdot \mathbf{E} - \mathbf{E} \cdot \mathbf{D}\right) h.
\end{aligned} \tag{4.53}$$

The relevant mismatch function $f_E(m_0a, c_p, \xi) = \mathcal{C}^{Cont} - \mathcal{C}^{Lat}$, for both operators, was also calculated to tree level in [126].

$$f_E(m_0a, c_p, \xi) = \frac{1}{8m_E^2a^2} - \frac{1}{8m_2^2a^2}, \tag{4.54}$$

where

$$\frac{1}{m_2 a} = \frac{2\xi^2}{m_0 a(2+m_0 a)} + \frac{\xi}{1+m_0 a}, \tag{4.55}$$

$$\frac{1}{4m_E^2 a^2} = \frac{\xi^2}{[m_0 a(2+m_0 a)]^2} + \frac{\xi c_p}{m_o a(2+m_0 a)}, \tag{4.56}$$

and $(m_0 a, c_p, \xi)$ are the tuned parameters of the action (see Section 3.4.3). The estimated size of the operators in equation (4.53) is

$$\langle \mathcal{O}_E \rangle^{HQET} \sim a^2 \Lambda_{QCD}^3. \tag{4.57}$$

Evaluating the mismatch function (4.54) at the values of the tuned RHQ paramters on the 32^3 lattice and combining with the operators in (4.53), for both B and B^*-mesons, we get

$$error = \sqrt{4} f_E \langle \mathcal{O}_E \rangle / 2M_B \sim 0.009\% \tag{4.58}$$

This is negligible compared to the scaling we see between the two lattice spacings, which we therefore ascribe solely to light-quark and gluon discretisation effects.

4.8.3 Light-quark and gluon discretisation errors

Our theoretical understanding of domain wall fermions and the Iwasaki gauge action tells us the lowest order cut-off effects should be proportional to a^2. However, examination of the data suggests that no cut-off dependence may also be a reasonable hypothesis. Figure 4.20 shows chiral fits to the data without an a^2 term. To estimate the systematic errors coming from the continuum extrapolation we consider the difference between a fit to our finest data set ($a \approx 0.086$fm) and the a^2 extrapolation using both lattices. The chiral value of the coupling in the no-scaling picture is 10% smaller than using our full chiral-continuum fitting procedure.

4.8.4 Chiral Extrapolation

To estimate the uncertainty in the chiral extrapolation we consider a range of possible fits. First, we consider the effect of neglecting the heaviest masses (Figure 4.22, left). This alters the form of the fit dramatically, but does not change the final result significantly. Figure 4.22 shows a fit to our data using a function linear in m_π^2. Finally, we try to simulate the effect of the missing higher-order terms in our fit function by varying the value of f_π by 25% in each direction (Figure 4.21). The largest variation in the chiral value of g_b is from the linear fit. This value is larger than our full chiral-continuum fit

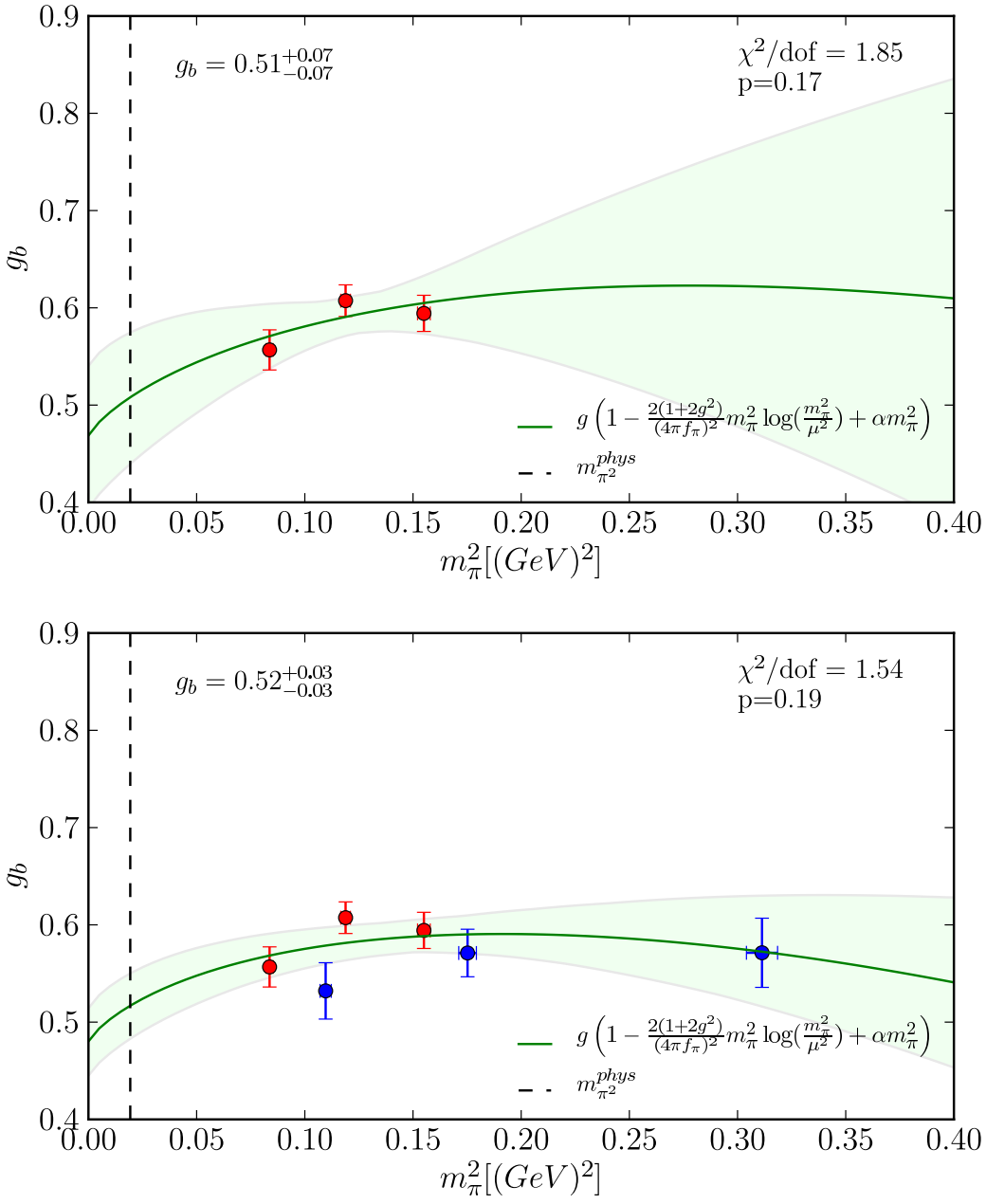

Figure 4.20: Chiral fits of the 32^2 data points (top) and the data points from both lattices (bottom). The data points in both plots are fitted to Eq. (4.43).

by approximately 10%. Considering together the similar size but opposite sign variations we produce in both the chiral and continuum fits, it seems reasonable to use the full fit (Figure 4.19) as our central value and include an error of 10% to account for uncertainties in the combined fitting procedure.

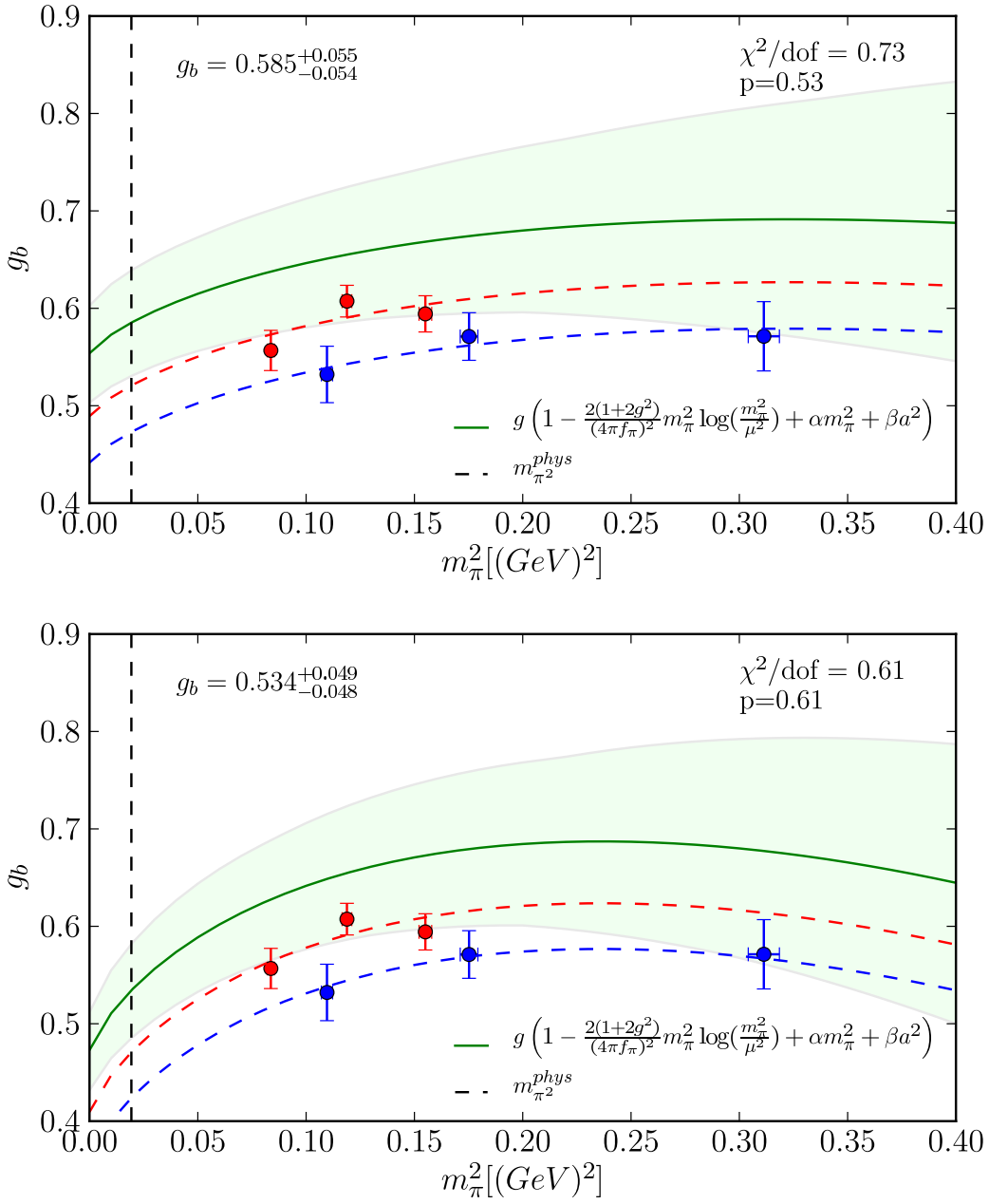

Figure 4.21: Increasing the value of f_π used in the fit (Eq. 4.44) by 25% (top) and decreasing by 25% (bottom).

4.8.5 Lattice Spacing Dependence

The coupling g_b is a dimensionless number calculated from ratios of correlators, hence it should have no strong dependence on the uncertainty in the lattice spacing. However, variations in a may have an effect on the chiral and continuum extrapolations. Table 4.7 shows the effect of varying the lattice spacing on the extrapolated chiral-continuum value of g_b. The largest variation in g_b is achieved by increasing the value of the lattice spacing by σ_{24} on the 24^3 lattice and decreasing the 32^3 lattice spacing by σ_{32}. Here

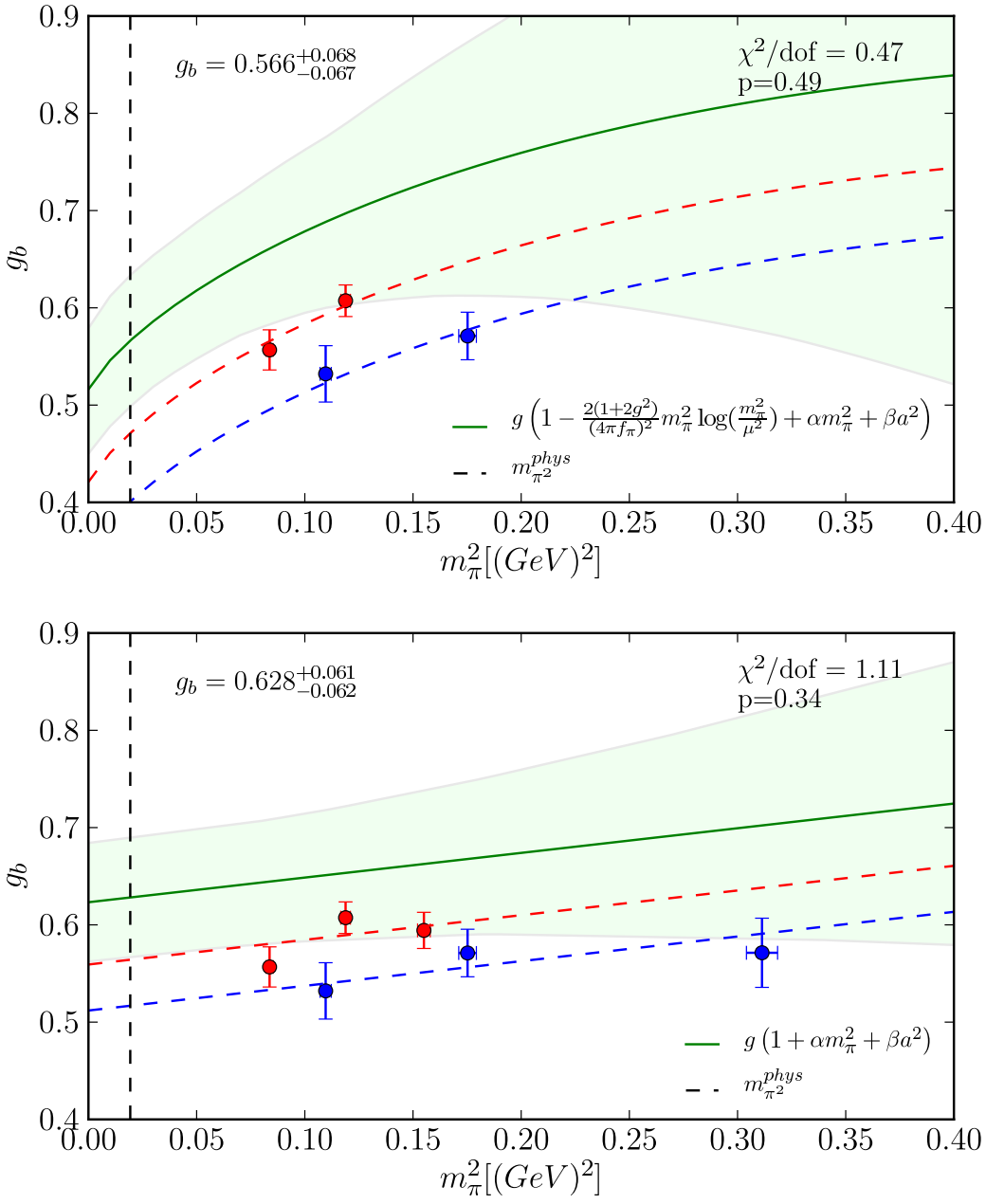

Figure 4.22: Chiral fit (Eq. 4.44) with the heaviest masses missing (top), and a simple linear fit ($g_0(1 + m_{pi}^2 + \beta a^2)$) to all the data (bottom).

σ corresponds to the quoted lattice scale uncertainty in [115]. In this extreme case, which assumes the errors on the two lattice spacings are completely anti-correlated, g_b changes by 1.44%. Therefore ascribing an error of 1% to this source of uncertainty seems reasonable.

Lattice Spacing		g_b	Δg_b	% change
a_{24}	a_{32}	0.5667		
$a_{24}+\sigma$	$a_{32}+\sigma$	0.5659	-0.0008	-0.14
$a_{24}-\sigma$	$a_{32}-\sigma$	0.5674	0.0007	0.12
$a_{24}-\sigma$	$a_{32}+\sigma$	0.5749	0.0082	1.44
$a_{24}+\sigma$	$a_{32}-\sigma$	0.5601	-0.0066	-1.16
$a_{24}+2\sigma$	$a_{32}+2\sigma$	0.5652	-0.0015	-0.26
$a_{24}-2\sigma$	$a_{32}-2\sigma$	0.5686	0.0019	0.34

Table 4.7: Variation in g_b as a function of the lattice spacing, where $a_{24}^{-1} = 1.729(28)$ GeV and $a_{32}^{-1} = 2.28(3)$ GeV

4.8.6 Finite Volume

We can expect that finite volume effects are small as there are no propagating light particles in the simulated system. To estimate the size of these effects we compare the axial vector matrix element at NLO in heavy meson χPT, fitted to our data, with and without the finite volume effects included. In the infinite volume the form of the effective coupling at NLO is calculated in [109].

$$g = g_0\left[1 - \frac{2}{(4\pi f_\pi)^2}I(m_\pi) - \frac{4g_0^2}{(4\pi f_\pi)^2}\frac{\partial F(m_\pi,\Delta)}{\partial\Delta} + \text{analytic terms}\right]\Bigg|_{\Delta=0} \tag{4.59}$$

In a finite volume the integrals $I(m_\pi)$ and $F(m_\pi, 0)$ become sums over discrete momenta. These can be treated as corrections and separated from the infinite volume results by the substitutions

$$I(m_\pi) \to I(m_\pi) + I_{FV}(m_\pi) \tag{4.60}$$

$$F(m_\pi) \to F(m_\pi) + F_{FV}(m_\pi). \tag{4.61}$$

The form of these corrections has been calculated in [127, 128], and in the limit $mL \gg 1$ they are given by

$$I_{FV}(m_\pi) = \frac{1}{4\pi^2}\sum_{\vec{u}\neq\vec{0}}\sqrt{\frac{m\pi}{2uL}}\left(\frac{1}{uL}\right)e^{-umL}\times\left\{1 + \frac{3}{8umL} - \frac{15}{128(umL)^2} + \mathcal{O}\left(\left[\frac{1}{umL}\right]^3\right)\right\}, \tag{4.62}$$

$$F_{FV}(m_\pi) = \frac{-m^2}{24\pi}\sum_{\vec{u}\neq\vec{0}}\frac{e^{-umL}}{uL}\mathcal{A}. \tag{4.63}$$

where $\bar{u} = (u_1, u_2, u_3)$ with $u_i \in \mathbb{Z}$, $u \equiv |\bar{u}|$ and

$$\mathcal{A} = e^{(z^2)}\left[1 - \mathrm{erf}(z)\right] + \left(\frac{1}{umL}\right)\left[\frac{1}{\sqrt{\pi}}\left(\frac{9z}{4} - \frac{z^3}{2}\right) + \left(\frac{z^4}{2} - 2z^2\right)e^{(z^2)}\left[1 - \mathrm{erf}(z)\right]\right] \tag{4.64}$$

$$- \left(\frac{1}{umL}\right)^2\left[\frac{1}{\sqrt{\pi}}\left(-\frac{39z}{64} + \frac{11z^3}{42} - \frac{9z^5}{16} + \frac{7z}{8}\right) - \left(-\frac{z^6}{2} + \frac{z^8}{8}\right)e^{(z^2)}\left[1 - \mathrm{erf}(z)\right]\right] \tag{4.65}$$

$$+ \mathcal{O}\left(\frac{1}{(umL)^3}\right), \tag{4.66}$$

$$z = \left(\frac{\Delta}{m}\right)\sqrt{\frac{umL}{2}}. \tag{4.67}$$

where $\Delta = m_{B^*} - m_B$. By evaluating the correction terms numerically and comparing the finite and infinite volume expressions fitted to our data at all simulated pion masses, we can estimate the size of the effects. These results are shown in Table 4.8. For our lightest data point, where you would expect finite volume effects to be largest, the size of the correction is 1%, so as a conservative estimate of the overall effect we add 1% to our error budget.

m_π [GeV]	g^{IV}	g^{FV}	$(g^{IV} - g^{FV})/g^{IV}$
0.289	0.5688	0.5628	0.0104
0.331	0.5387	0.5357	0.0056
0.344	0.5907	0.5882	0.0041
0.393	0.6061	0.6049	0.0019
0.418	0.5652	0.5644	0.0014
0.557	0.5733	0.5732	0.0002

Table 4.8: Finite volume corrections to the effective coupling

4.8.7 RHQ parameter uncertainties

4.8.7.1 Statistical

To test the dependence of g_b on the uncertainties in the tuned RHQ parameters we calculate the coupling on the 24^3 $m_l = 0.005$ ensemble using the full box of RHQ parameters around the tuned values (3.57). We then interpolate g_b to the point of the tuned parameters using equations (4.68, 4.69, 4.70). By following this procedure underneath a jack-knife, using the tuned parameter values on each configuration, we can propagate the errors from the tuning through to g_b. Comparison of this number to the result calculated directly using the tuned values of the parameters gives a measure of how sensitive g_b is to the uncertainties arising from the tuning.

$$M_{g_b}^{RHQ} = J_M \times \begin{bmatrix} m_o a \\ c_p \\ \xi \end{bmatrix}^{Tuned} + A_M \tag{4.68}$$

$$J_M = \begin{bmatrix} \frac{M_3 - M_2}{2\sigma_{m_0 a}}, & \frac{M_5 - M_4}{2\sigma_{c_p}}, & \frac{M_7 - M_6}{2\sigma_\xi} \end{bmatrix} \tag{4.69}$$

$$A_M = M_1 - J_M \times \begin{bmatrix} m_o a, & c_p, & \xi \end{bmatrix}^T \tag{4.70}$$

Comparing the two values (Table 4.9) there is no significant difference. The central values differ by 0.1%, and the errors differ by 0.9%. In the context of the overall uncertainty this can be considered negligible.

	g_b
Tuned point	0.7581 ± 0.0412
Interpolated	0.7573 ± 0.0408

Table 4.9: Values of the (unrenormalised) coupling constant g_b on the 24^3 $m_l = 0.005$ ensemble calculated directly at the tuned RHQ parameters, and interpolated to the tuned point under the jack-knife. The difference between the two values is negligible.

4.8.7.2 Systematic

We also consider the effect of systematic uncertainties that arise in the determination of the RHQ parameters. These are estimated in [3], the sources being heavy-quark discretisation effects, uncertainty on the lattice spacing, and uncertainty in the experimental inputs. To determine the sensitivity of g_b on these uncertainties we use the calculation on the box of parameters (3.57) to interpolate to the value of the coupling at the tuned parameter values, shifted by the systematic uncertainties. This procedure relies on the box being small enough that the parameter dependence is linear within this region. We shift one parameter at a time by each error source and consider the overall error as the effect of each of these shifts added in quadrature. Figures 4.23, 4.24 and 4.25 show g_b as a function of each RHQ parameter, with shaded regions corresponding to the parameter uncertainties. The combined result is an error of 1.5% for the systematic uncertainties on the RHQ parameters, as shown in table 4.10.

4.8.8 Unphysical strange-quark mass

Our simulation is performed with a sea strange-quark mass that differs from the physical value by approximately 10%. Although the correlators we calculate to extract the

	% error from parameter			
Source	$m_o a$	c_p	ξ	Total
HQ discretisation	0.25	0.65	0.30	0.76
Lattice scale	0.97	0.65	0.24	1.19
Experimental	0.14	0.33	0	0.35
All sources	1.01	0.98	0.38	1.46

Table 4.10: The effect of RHQ parameter systematic errors on g_b. Each parameter was shifted by one sigma and the effect on g_b calculated by extrapolation using equation (4.68).

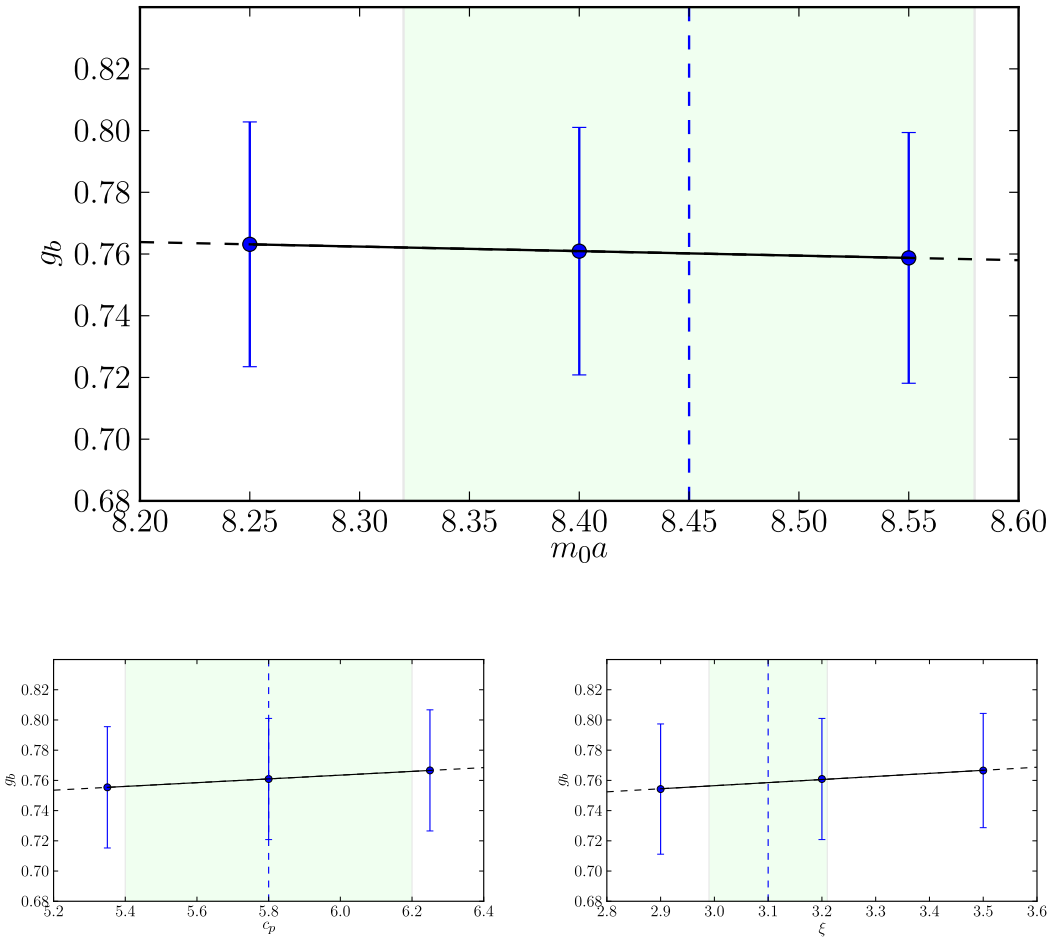

Figure 4.23: g_b as a function of the three RHQ parameters $m_0 a$ (top), c_p (left) and ξ (right). The vertical dashed line shows the tuned parameter value, and the shaded region shows the systematic error coming from the heavy-quark discretisation effects.

coupling contain no valence strange-quarks, the value of m_s can affect loops. To test the dependence of our calculation on the sea strange-quark mass we initially tried reweighting [129, 130]. The reweighting factors have already been calculated [115] on a subset of the configurations used in this study. We examine the lightest available ensemble on

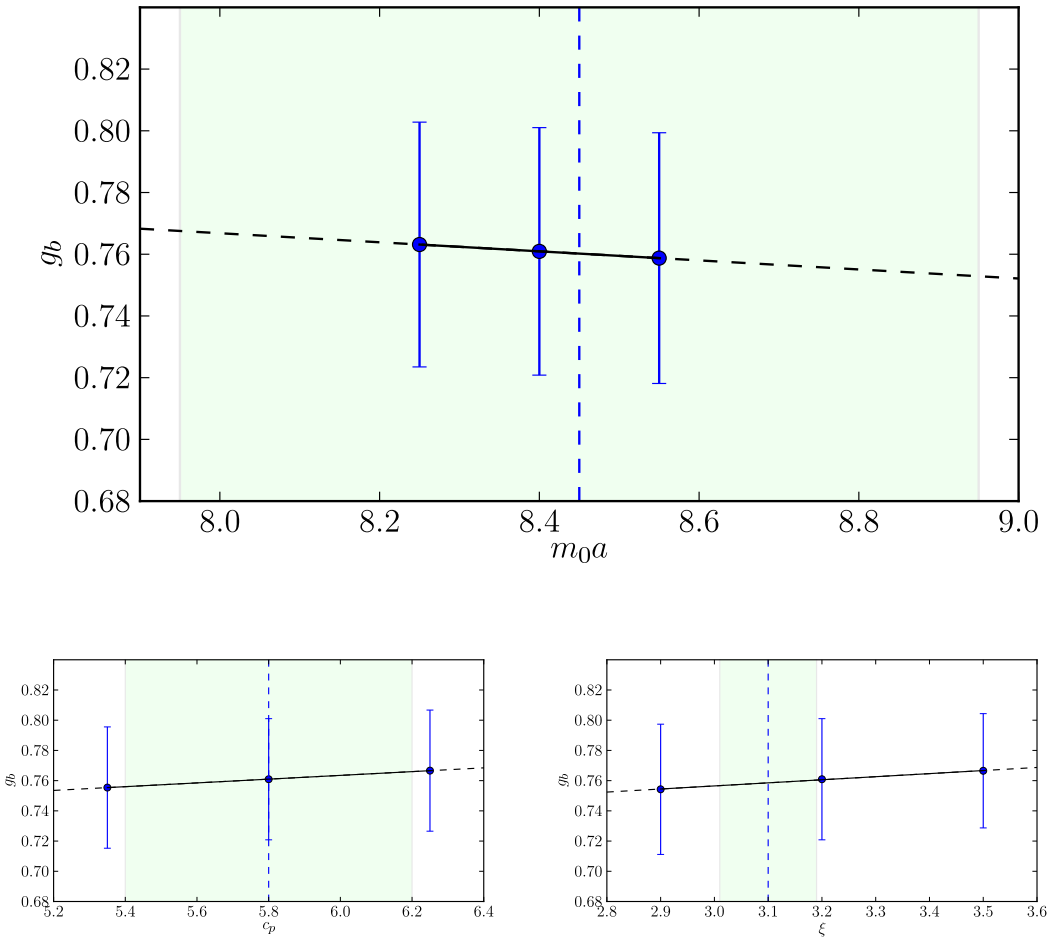

Figure 4.24: g_b as a function of the three RHQ parameters $m_0 a$ (top), c_p (left) and ξ (right). The vertical dashed line shows the tuned parameter value, and the shaded region shows the systematic error coming from the lattice scale uncertainty.

both the fine and the coarser lattice. For the 24^3 lattice we reweight from $m_s^{(sim)} = 0.04$ to the physical mass of $m_s = 0.0345$, in 22 steps on a subset of 195 configurations. On the finer lattice we reweight $m_s^{(sim)} = 0.03$ to $m_s = 0.0275$, in 5 steps on a subset of 307 configurations, using two source positions. Figure 4.26 shows the dependence of g_b on the sea strange-quark mass over these ranges. The reweighting calculation on the coarser ensemble suffers from poor statistics, both from the small number of configurations used, and the additional statistical fluctuation introduced by the reweighting procedure. Each step in the reweighting proceedure is highly correlated to the previous one, therefore to ascertain whether we see any statistically significant result we take the difference between either end of the mass range on each configuration and perform a jack-knife. The change in the coupling after rewighting to the physical mass is smaller than the resolution given by the jack-knife errors. We therefore turn to other techniques to determine the effect of the unphysical sea strange-quark mass.

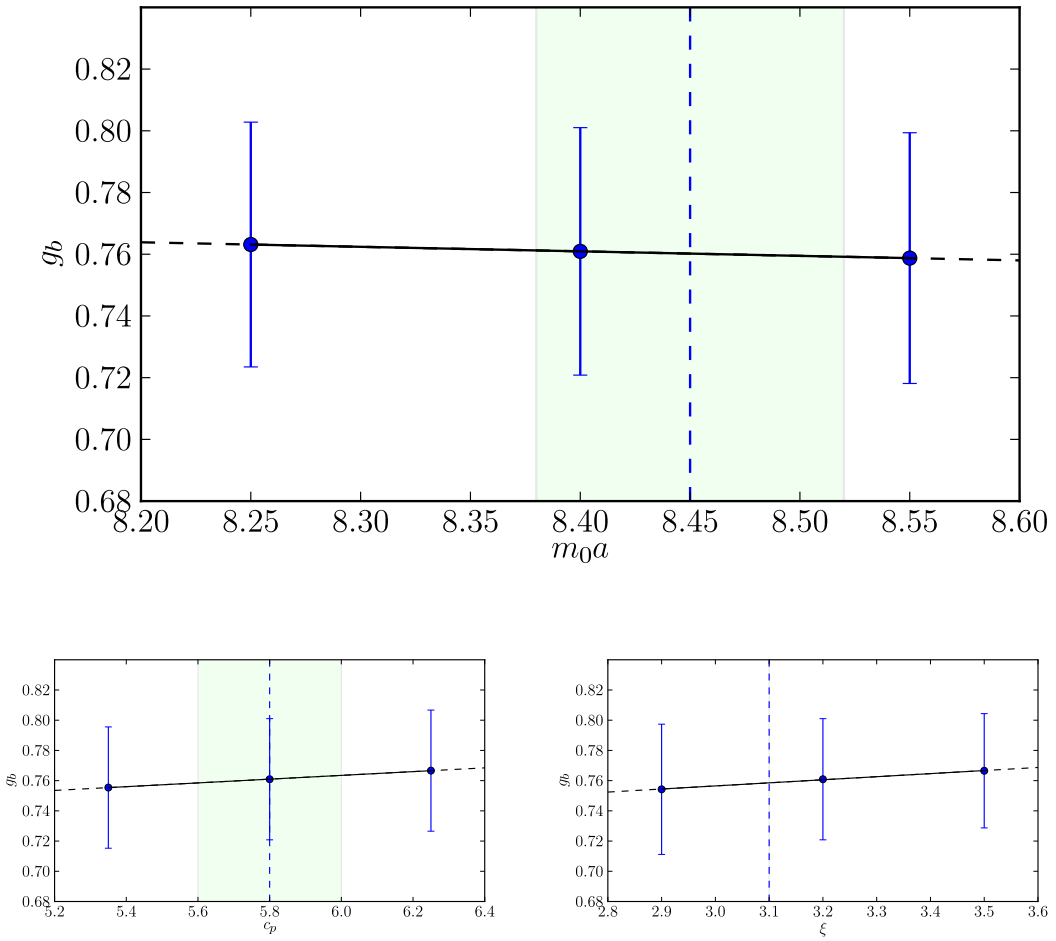

Figure 4.25: g_b as a function of the three RHQ parameters m_0a (left), c_p (middle) and ξ (right). The vertical dashed line shows the tuned parameter value, and the shaded region shows the systematic error coming from the experimental uncertainties in the quantities used to tue the paramaters.

Detmold et al. have also derived the HMχPT NLO axial-current matrix element in the partially quenched $SU(2)$ and $SU(3)$ cases [109]. This allows us to evaluate the expression with different valence and sea strange-quark masses. The NLO matrix element has four different contributions, coming from so called sunset diagrams, wave-function renormalisation, tadpole diagrams and the NLO analytic terms. Each of these contributions have been calculated explicitly, except the NLO analytic terms, for which the observation was made that their contribution is proportional to the pseudo-scalar mass squared. We have calculated the effect of a 10% change in the sea strange-quark on the loop diagrams, and this propagates to a 1.5% change in the value of the coupling. This result seems consistent with the study of reweighting on the ensembles [115] performed by the RBC/UKQCD collaboration where similar quantities, namely the pion-decay constant, was seen to display a 1.5% change in reweighting to the physical strange-quark mass. Therefore we ascribe an error of 1.5% due to the unphysical strange-quark mass.

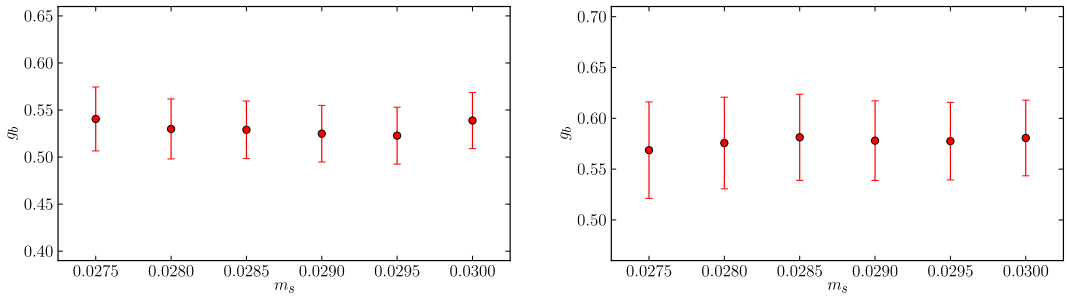

Figure 4.26: Reweighting on a subset of configurations. 32^3 $m_l = 0.004$ (left), 32^3 $m_l = 0.006$ (right)

Ensemble	$m_s^{(sim)}$	$m_s^{(phys)}$	N_{conf}
24^3 $m_l = 0.005$	0.04	0.0345	195
24^3 $m_l = 0.010$	0.04	0.0345	178
32^3 $m_l = 0.004$	0.03	0.0275	307 ($\times$2 sources)
32^3 $m_l = 0.006$	0.03	0.0275	156 ($\times$2 sources)
Ensemble	g_b at $m_s^{(sim)}$	g_b at $m_s^{(phys)}$	Δg_b
24^3 $m_l = 0.005$	0.447±0.088	0.540±0.159	0.093±0.114
24^3 $m_l = 0.010$	0.694±0.089	0.826±0.186	0.133±0.141
32^3 $m_l = 0.004$	0.539±0.030	0.540±0.034	0.002±0.018
32^3 $m_l = 0.006$	0.581±0.037	0.569±0.047	-0.012±0.024

Table 4.11: Parameters and results of strange-quark mass reweighting. The Δg_b column gives the difference between the coupling at the simulated and physical strange mass, calculated underneath a jack-knife. The differences are not statistically significant.

4.8.9 Final result and error budget

Systematic Errors	
Lattice spacing uncertainty	1%
Finite volume	1%
RHQ parameters	1.5%
Chiral and continuum extrapolation	10%
Nonphysical strange-quark mass	1.5%
Total	10.3%

Table 4.12: Systematic error budget.

Taking the sum in quadrature of all the systematic errors described in section 4.8 we arrive at a total uncertainty of 10.3%. Our final value of the g_b coupling including statistical and systematic errors is:

$$g_b = 0.567(52)_{stat}(58)_{sys} \tag{4.71}$$

Chapter 5

Conclusions

We have performed a calculation of the single low energy constant of the heavy meson chiral perturbation theory interaction Lagrangian, g_b and arrived at a final result of:

$$g_b = 0.567(52)_{stat}(58)_{sys} \tag{5.1}$$

Our calculation used the domain wall fermion action for the light-quarks that provides good chiral properties, and automatic $\mathcal{O}(a)$ improvement. To simulate the heavy b-quarks we use the non-pertubatively tuned relativistic heavy-quark action. This allowed us to keep discretisation effects under good control, whilst simulating with a physical heavy-quark mass. In fact by utilising the RHQ action we have been able to perform the first calculation of the coupling directly at the physical b-quark mass. Our simulation was performed at unphysical light-quark masses, but we have performed a theoreticaly guided extrapolation down to the physical point. Furthermore, we have applied our understanding of the scale dependence of our lattice actions to subtract any cut-off effects, giving us a result valid in the continuum. We have acheived good statistical precision and conducted a full analysis of all sources of systematic uncertainty. The dominant sources of systematic errors are the chiral and continuum extrapolations, both of which can be improved by further numerical simulation with lighter quarks and extra lattice spacings. We feel that we have made conservative estimates of these effects, as it is always better to over, rather than underestimate systematics.

Our result is in agreement with other determinations of the coupling, but has the advantage of being performed with $2+1$ flavours of dynamical sea quarks. The only previous calculation in a $2+1$ flavour formulation [108] simulated the heavy quark in the infinite mass limit, whereas we have utilised the non-perturbatively tuned relativistic heavy quark action to simulate with a physical b-quark mass. Figure 5.1 shows a comparison of previous calculations of the coupling. The only previous result at the b-quark mass was found by interpolating between static and charm-mass results, and is shown as transparent in Fig. 5.1. Interestingly, our value also lies in the region which you

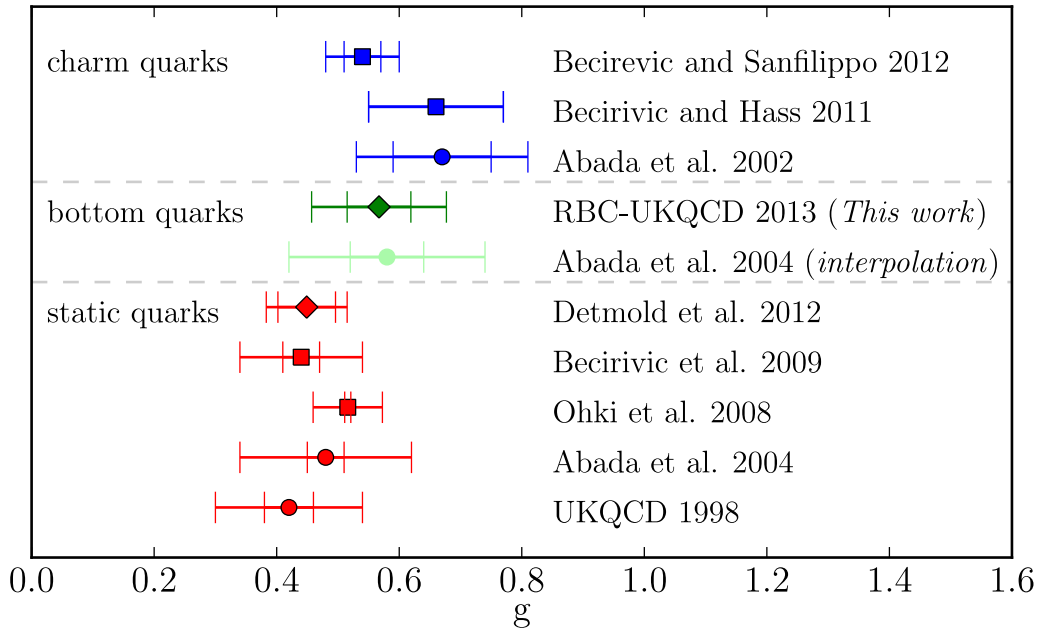

Figure 5.1: Comparison of recent calculations of the HMχPT coupling. The inner bars represent statistical errors and the outer bars represent systematic errors, except Becirevic and Hass who only quote a single error. Quenched calculations are represented with circular markers, the n_f=2 calculations are shown with square markers and diamond markers correspond to n_f=2+1 calculations.

would expect by making this interpolation. Examination of these results point to only a mild dependence on the heavy-quark mass which inspires confidence in the framework of HMχPT. Further confidence is taken from experimental results of $\Gamma(D^*)$ [48, 131] which are in agreement with the calculations at the charm mass. It is not possible to experimentally determine the coupling with b-quarks as there is not sufficient phase space for the decay to proceed. This is further evidence for the value of this calculation. It is hoped that further study of this quantity with configurations closer to the physical light-quark mass would reduce the systematics arising from the chiral extrapolations, and application of low-mode-averaging techniques would further increase the statistical precision.

Appendix A

Correlator Ratios

The form factor A_1 can be accessed through the ratio of the three-point correlator, defined in (4.11), and the two two-point functions (4.12) and (4.12). Both the momentum of B and the B^* meson are set to zero, meaning the extracted value of the form factor is $A_1(q_0^2)$ where $q_0^2 = (m_{B^*} - m_B)^2$.

$$R_1 = \frac{C^{(3)}_{i,i}\left(t_x, t_y; \bar{p} = 0, \bar{p}' = 0\right) Z_B^{1/2} Z_{B^*}^{1/2}}{C^{(2)}_{BB}\left(t_y; \bar{p} = 0\right) C^{(2)}_{B^*{}_i B^*{}_i}\left(T - t_x; \bar{p} = 0\right)} = (m_{B^*} + m_B) A_1(q_0^2) \tag{A.1}$$

To access the other form factors we need to inject a unit of momentum, such that $\bar{q} = \bar{p} = (1, 0, 0) \times 2\pi/L$ and $\bar{p}' = 0$. Following the notation from [107], we define the ratio

$$R_2 = \frac{C^{(3)}_{1,0}\left(t_x, t_y; \bar{p} \neq 0, \bar{p}' = 0\right) Z_B^{1/2} Z_{B^*}^{1/2}}{C^{(2)}_{BB}\left(t_y; \bar{p} = 0\right) C^{(2)}_{B^*{}_2 B^*{}_2}\left(T - t_x; \bar{p} \neq 0\right)} = \sum_\lambda \langle B(p'|A_0|B^*(p,\lambda)\rangle \epsilon_1^\lambda$$

$$\begin{aligned}
&= 2m_{B^*} A_0 \frac{q_1 q_0}{q^2}\left(1 - \frac{p\cdot q}{q^2}\right) + (m_{B^*} + m_B) A_1 \left(-\frac{q_1 p_o}{p^2} - \frac{q_1 q_0}{q^2}\left(1 - \frac{p\cdot q}{p^2}\right)\right) \\
&\qquad + \frac{A_2}{m_{B^*} + m_B}\left(p_0 + p_0' - \frac{m_{B^*}^2 + m_B^2}{q^2} q_0\right) q_1 \left(1 - \frac{p\cdot q}{p^2}\right) \\
&= \frac{q_1 q_0}{q^2}\left(1 - \frac{p\cdot q}{p^2}\right)\left[2m_{B^*} A_0 - (m_{B^*} + m_B) A_1 + \frac{1}{m_{B^*} + m_B}\left(\frac{p_0 + p_0'}{q_0} - (m_{B^*}^2 - m_B^2)\right) A_2\right] \\
&\qquad - \frac{(m_{B^*} + m_p) q_1 p_0}{p^2} A_1 \\
&= \frac{q_1 q_0}{q^2}\left(1 - \frac{p\cdot q}{p^2}\right)\left[2m_{B^*} A_0 - (m_{B^*} + m_B) A_1 - (m_{B^*} - m_B) A_2\right] \\
&\qquad - (m_{B^*} + m_B)\frac{q_1 p_0}{p^2} A_1 + \frac{a_1}{m_{B^*} + m_B}\frac{p_0 + p_0'}{q_0} q_1 q_0 \left(1 - \frac{p\cdot q}{p^2}\right)
\end{aligned} \tag{A.2}$$

where in the first line the polarisation vector was extracted for the B^* matrix element Z_{B^*} and in subsequent lines the polarisation states are summed over with the polarisation vectors in the form factor decomposition (4.5). Furthermore, a similar calculation is carried out to form the ratios $R3$ and $R4$.

$$\begin{aligned} R_3 &= \frac{C^{(3)}_{1,1}\left(t_x, t_y; \bar{p} \neq 0, \bar{p}' = 0\right) Z_B^{1/2} Z_{B^*}^{1/2}}{C^{(2)}_{BB}\left(t_y; \bar{p} = 0\right) C^{(2)}_{B^*{}_2 B^*{}_2}\left(T - t_x; \bar{p} \neq 0\right)} = \sum_\lambda \langle B(p'|A_1|B^*(p,\lambda)\rangle \epsilon_1^\lambda \\ &= 2m_{B^*} A_0 \frac{q_1^2}{q^2}\left(1 - \frac{p\cdot q}{q^2}\right) + (m_{B^*} + m_B) A_1 \left(1 - \frac{q_1^2}{p^2} - \frac{q_1^2}{q^2}\left(1 - \frac{p\cdot q}{q^2}\right)\right) \\ &\qquad + \frac{A_2}{m_{B^*} + m_B}\left(p_1 - \frac{m_{B^*}^2 - m_B^2}{q^2} q_1\right) q_1 \left(1 - \frac{p\cdot q}{q^2}\right) \\ &= \frac{q_1^2}{q^2}\left(1 - \frac{p\cdot q}{q^2}\right)\left[2m_{B^*}A_0 - (m_{B^*} + m_B)A_1 - A_2(m_{B^*} - m_B)\right] \\ &\qquad + (m_{B^*} + m_B) A_1 \left(1 - \frac{q_1^2}{p^2}\right) + \frac{A_2}{m_{B^*} + m_B} q_1^2 \left(1 - \frac{p\cdot q}{p^2}\right) \end{aligned} \tag{A.3}$$

$$\begin{aligned} R_4 &= \frac{C^{(3)}_{2,2}\left(t_x, t_y; \bar{p} \neq 0, \bar{p}' = 0\right) Z_B^{1/2} Z_{B^*}^{1/2}}{C^{(2)}_{BB}\left(t_y; \bar{p} = 0\right) C^{(2)}_{B^*{}_2 B^*{}_2}\left(T - t_x; \bar{p} \neq 0\right)} = \sum_\lambda \langle B(p'|A_2|B^*(p,\lambda)\rangle \epsilon_2^\lambda \\ &= (m_{B^*} + m_B) A_1(q^2) \end{aligned} \tag{A.4}$$

These ratios can then be combined to access to the form factor A_2 through the expression

$$\frac{A_2}{A_1} = \frac{(m_{B^*} + m_B)^2}{2m_B^2 q_1^2}\left[-q_1^2 + E_{B^*}(E_{B^*} - m_B) - \frac{m_{B^*}^2 (E_{B^*} - m_B)}{E_{B^*}} \frac{R_3}{R_4} - \mathrm{i}\frac{m_{B^*}^2 q_1}{E_{B^*}} \frac{R_2}{R_4}\right]. \tag{A.5}$$

Appendix B

Other Plots

This appendix contains plots of the correlator ratios and meson two-point functions for the ensembles not shown in the main text.

B.1 24^3, $m_l = 0.005$

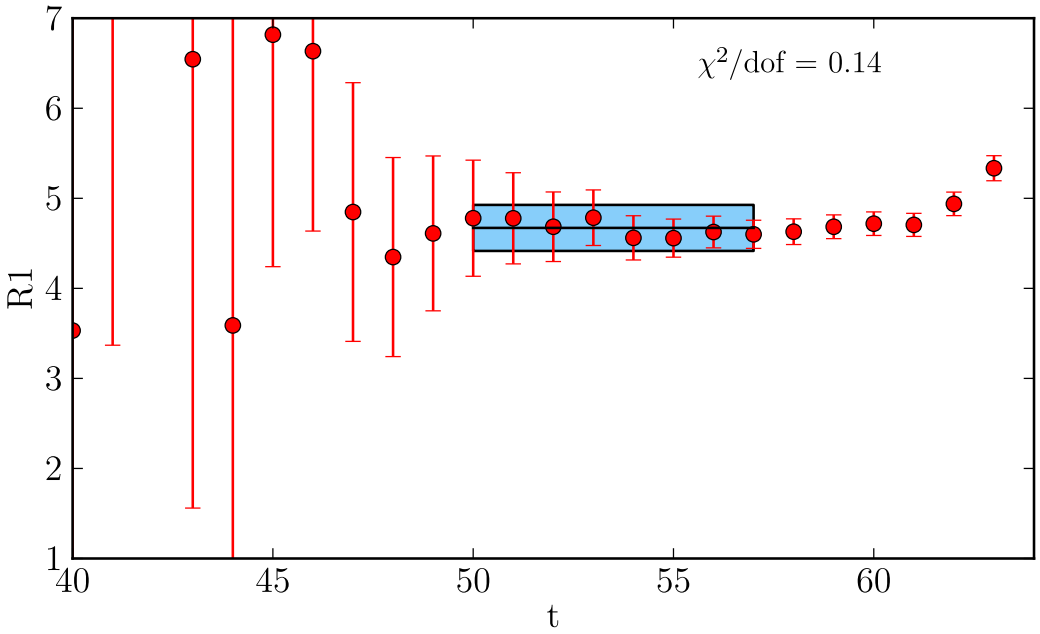

Figure B.1: Ratio R_1 on the 24^3, $m_l = 0.005$ ensemble.

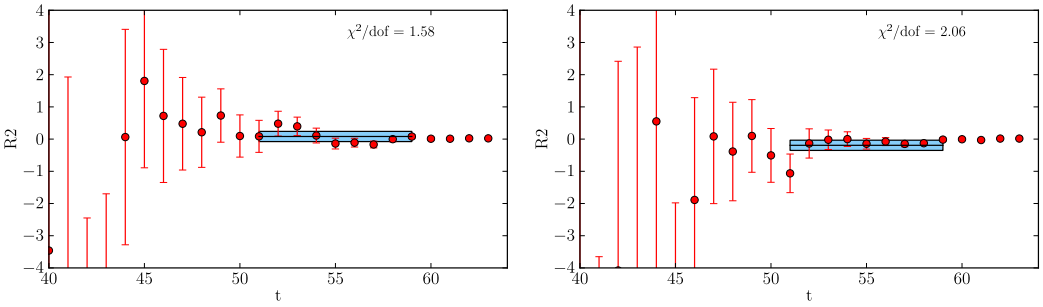

Figure B.2: Ratio R_2 on the 24^3, $m_l = 0.005$ ensemble, at the first (left) and second (right) non-zero momentum.

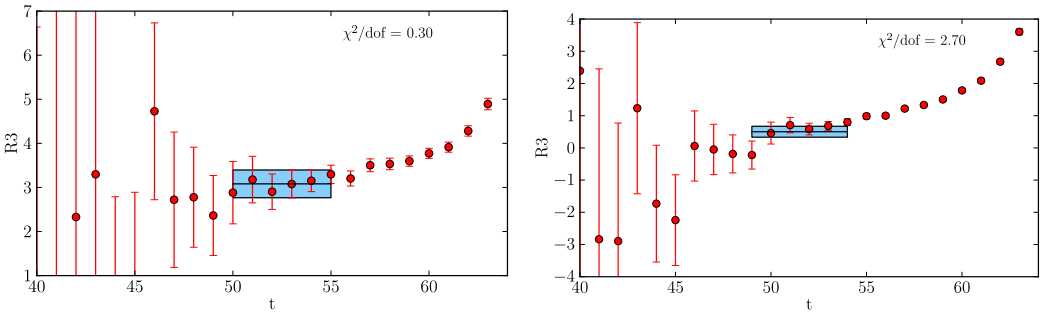

Figure B.3: Ratio R_3 on the 24^3, $m_l = 0.005$ ensemble, at the first (left) and second (right) non-zero momentum.

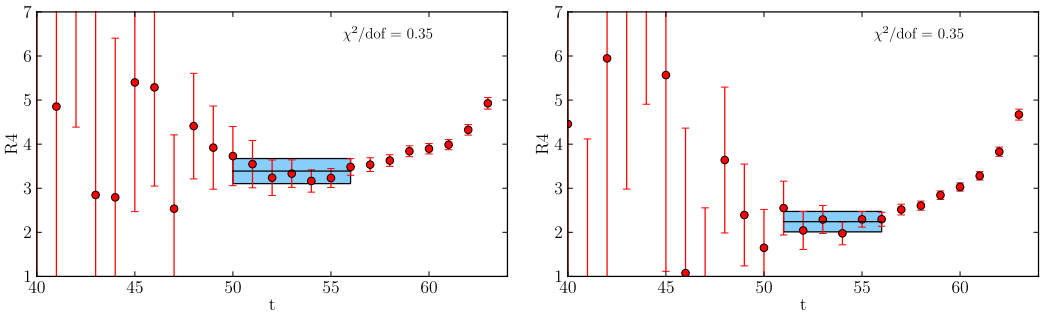

Figure B.4: Ratio R_4 on the 24^3, $m_l = 0.005$ ensemble, at the first (left) and second (right) non-zero momentum.

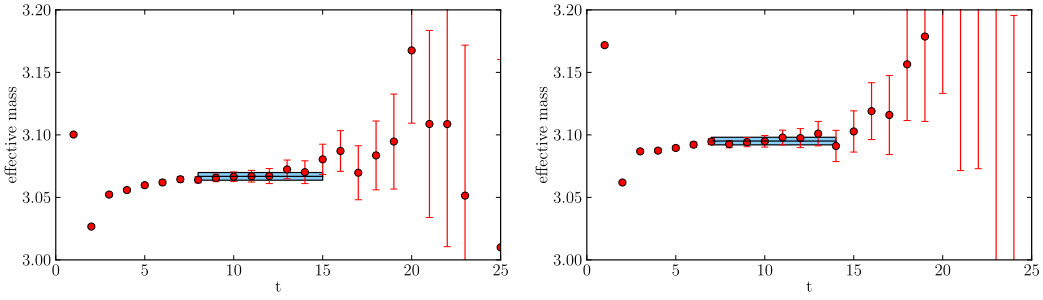

Figure B.5: B meson (left) and B^* meson effective mass on the 24^3, $m_l = 0.005$ ensemble, at zero momentum.

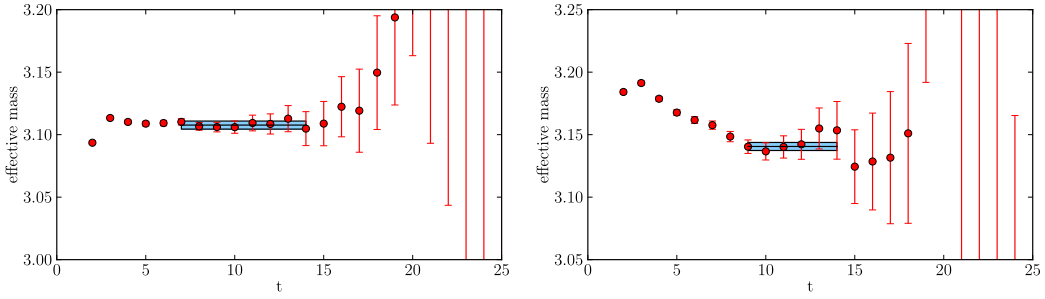

Figure B.6: B^* meson effective mass on the 24^3, $m_l = 0.005$ ensemble at the first non-zero momentum (left) and the second non-zero momentum (right).

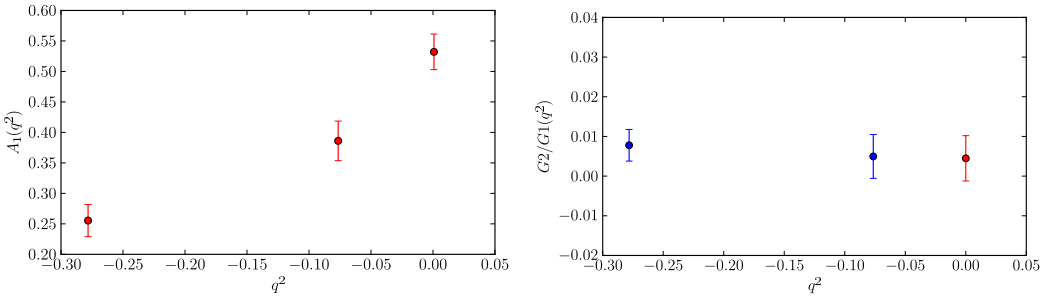

Figure B.7: $A_1(q^2)$ and $G2/G1(q^2)$ on the 24^3, $m_l = 0.005$ ensemble.

B.2 24^3, $m_l = 0.010$

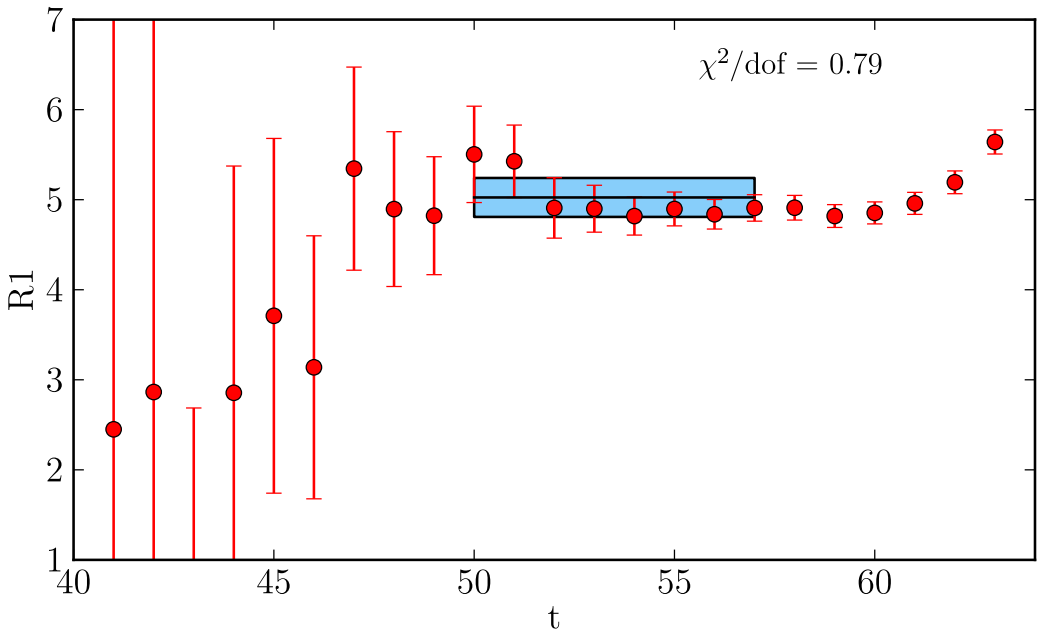

Figure B.8: Ratio R_1 on the 24^3, $m_l = 0.010$ ensemble.

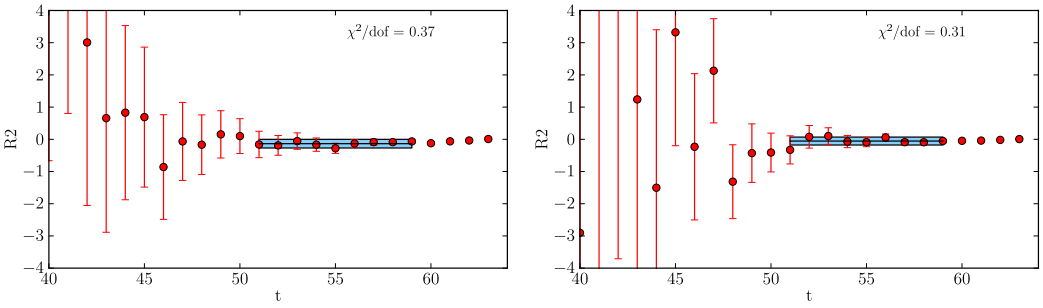

Figure B.9: Ratio R_2 on the 24^3, $m_l = 0.010$ ensemble, at the first (left) and second (right) non-zero momentum.

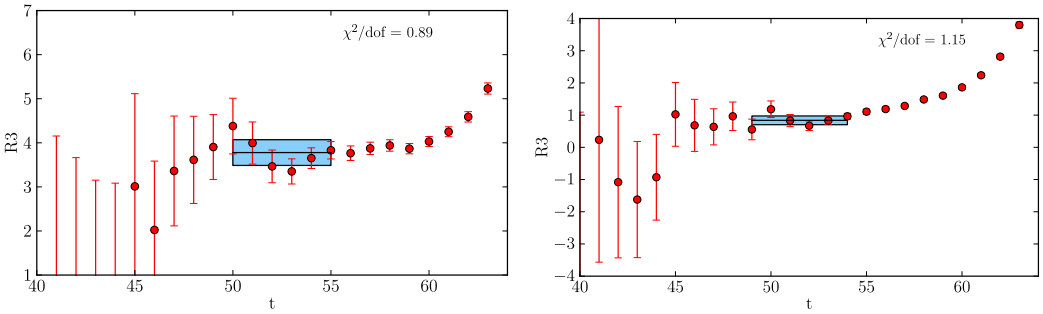

Figure B.10: Ratio R_3 on the 24^3, $m_l = 0.010$ ensemble, at the first (left) and second (right) non-zero momentum.

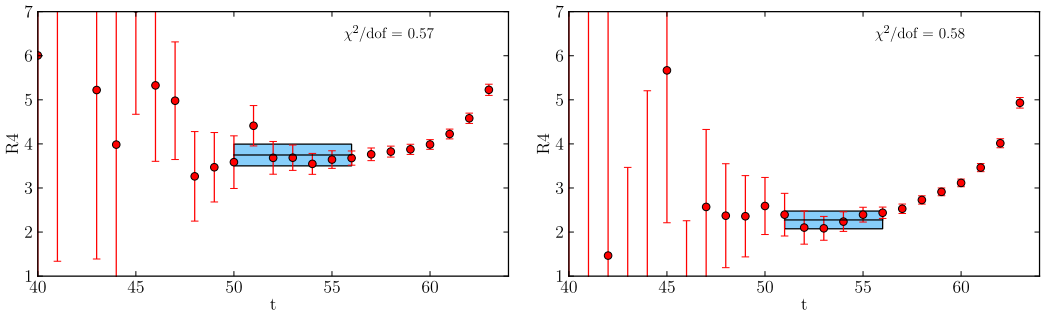

Figure B.11: Ratio R_4 on the 24^3, $m_l = 0.010$ ensemble, at the first (left) and second (right) non-zero momentum.

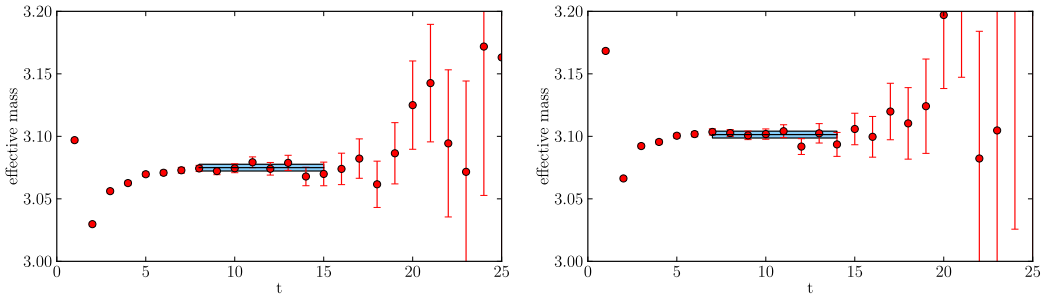

Figure B.12: B meson (left) and B^* meson effective mass on the 24^3, $m_l = 0.010$ ensemble, at zero momentum.

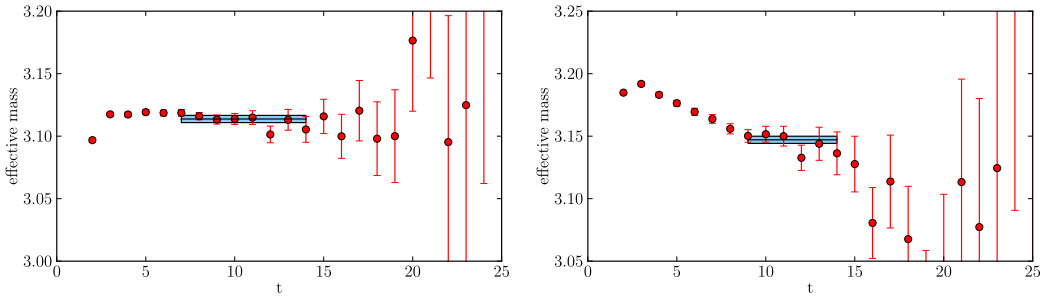

Figure B.13: B^* meson effective mass on the 24^3, $m_l = 0.010$ ensemble at the first non-zero momentum (left) and the second non-zero momentum (right).

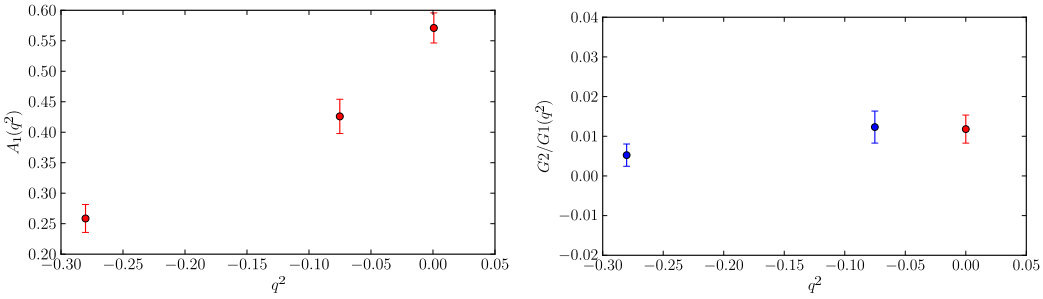

Figure B.14: $A_1(q^2)$ and $G2/G1(q^2)$ on the 24^3, $m_l = 0.010$ ensemble.

B.3 24^3, $m_l = 0.020$

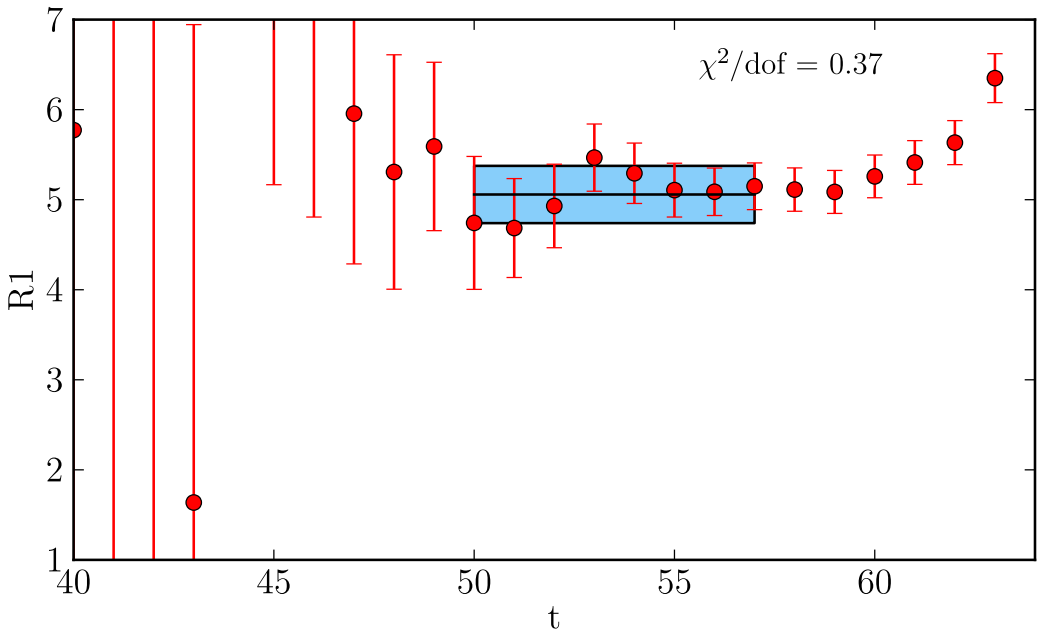

Figure B.15: Ratio R_1 on the 24^3, $m_l = 0.020$ ensemble.

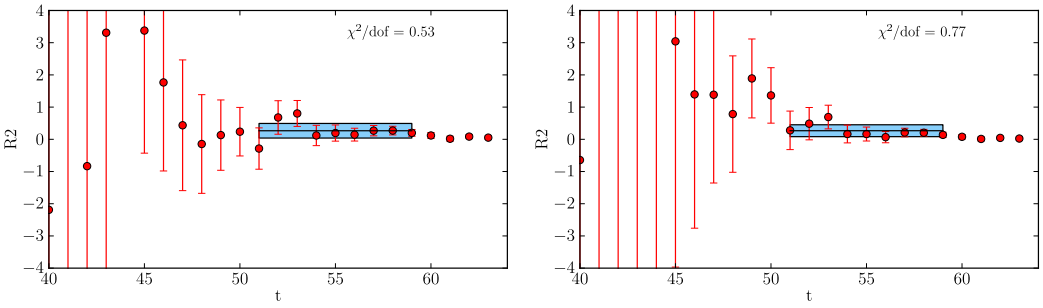

Figure B.16: Ratio R_2 on the 24^3, $m_l = 0.020$ ensemble, at the first (left) and second (right) non-zero momentum.

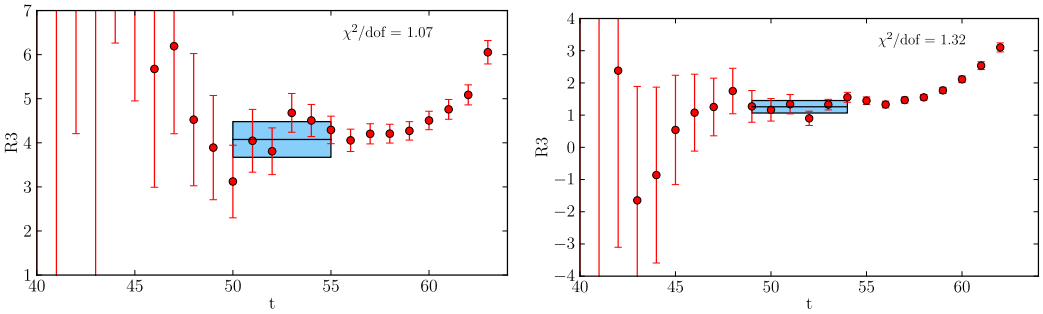

Figure B.17: Ratio R_3 on the 24^3, $m_l = 0.020$ ensemble, at the first (left) and second (right) non-zero momentum.

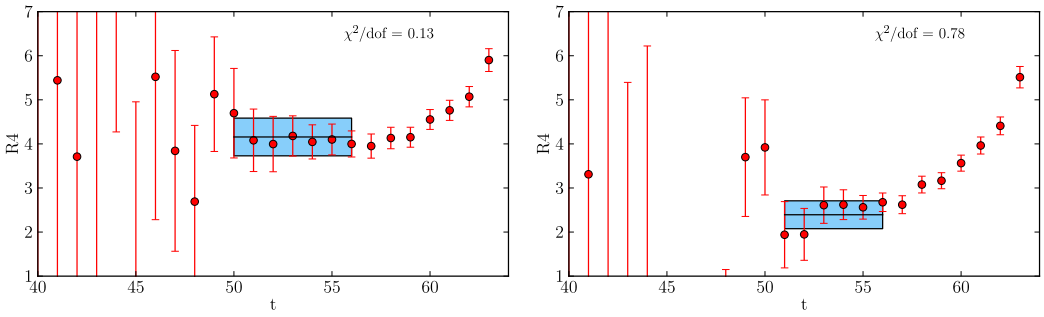

Figure B.18: Ratio R_4 on the 24^3, $m_l = 0.020$ ensemble, at the first (left) and second (right) non-zero momentum.

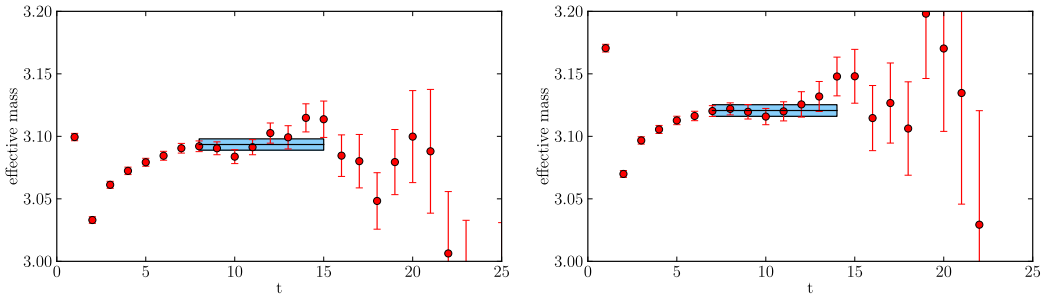

Figure B.19: B meson (left) and B^* meson effective mass on the 24^3, $m_l = 0.020$ ensemble, at zero momentum.

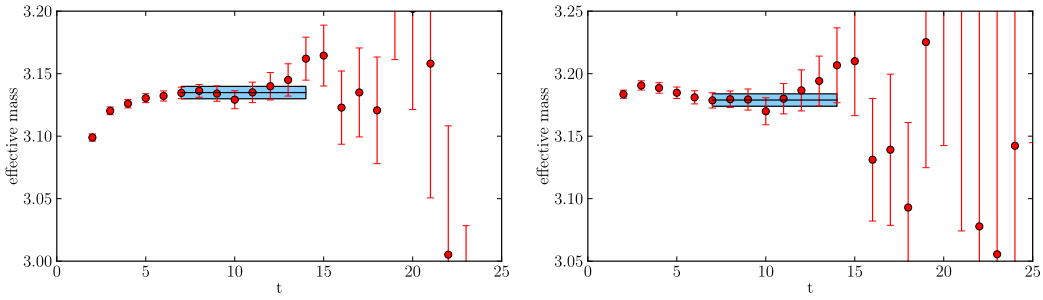

Figure B.20: B^* meson effective mass on the 24^3, $m_l = 0.020$ ensemble at the first non-zero momentum (left) and the second non-zero momentum (right).

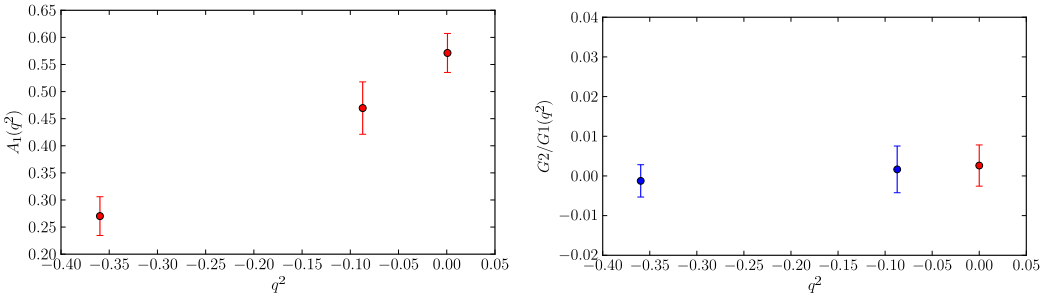

Figure B.21: $A_1(q^2)$ and $G2/G1(q^2)$ on the 24^3, $m_l = 0.020$ ensemble.

B.4 32^3, $m_l = 0.004$

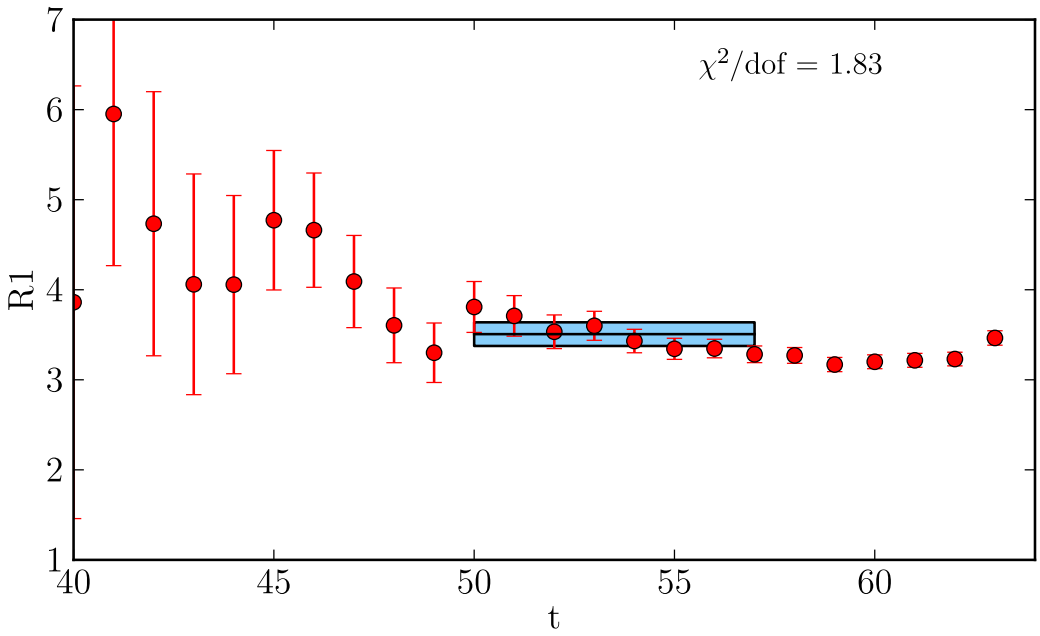

Figure B.22: Ratio R_1 on the 32^3, $m_l = 0.004$ ensemble.

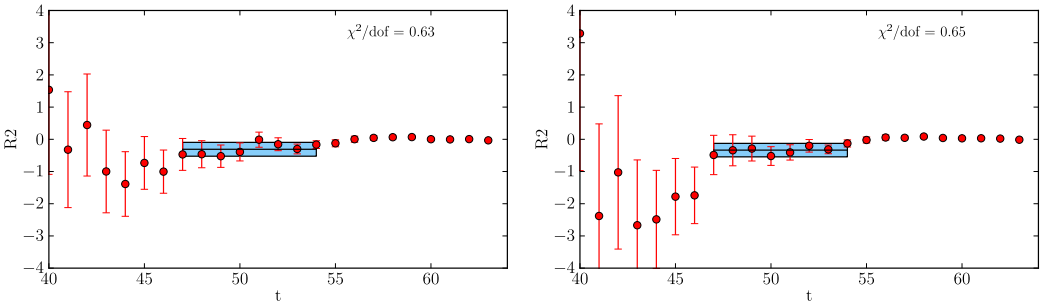

Figure B.23: Ratio R_2 on the 32^3, $m_l = 0.004$ ensemble, at the first (left) and second (right) non-zero momentum.

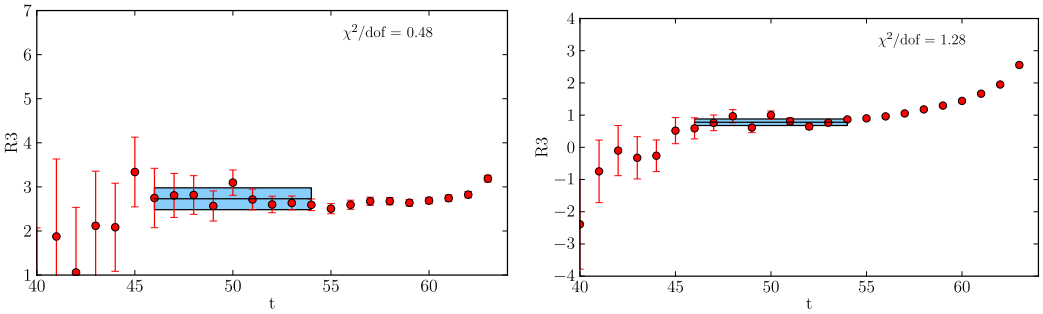

Figure B.24: Ratio R_3 on the 32^3, $m_l = 0.004$ ensemble, at the first (left) and second (right) non-zero momentum.

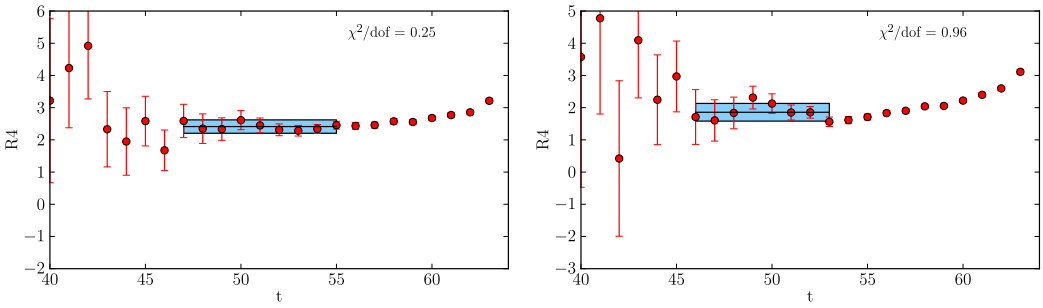

Figure B.25: Ratio R_4 on the 32^3, $m_l = 0.004$ ensemble, at the first (left) and second (right) non-zero momentum.

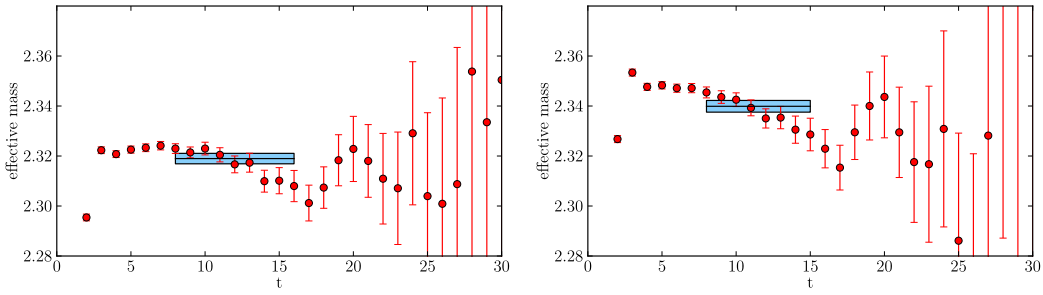

Figure B.26: B meson (left) and B^* meson effective mass on the 32^3, $m_l = 0.004$ ensemble, at zero momentum.

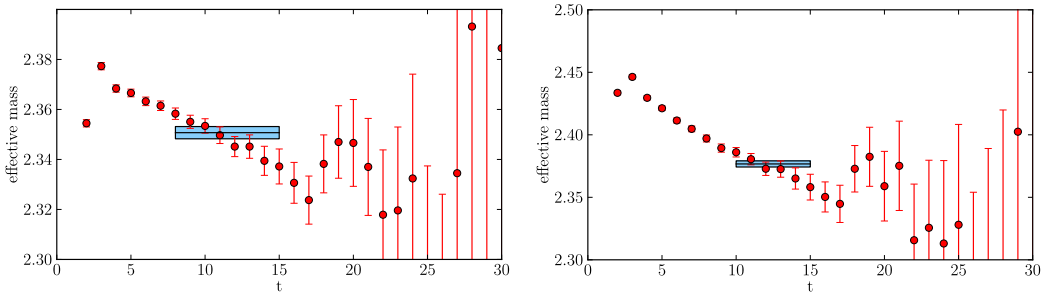

Figure B.27: B^* meson effective mass on the 32^3, $m_l = 0.004$ ensemble at the first non-zero momentum (left) and the second non-zero momentum (right).

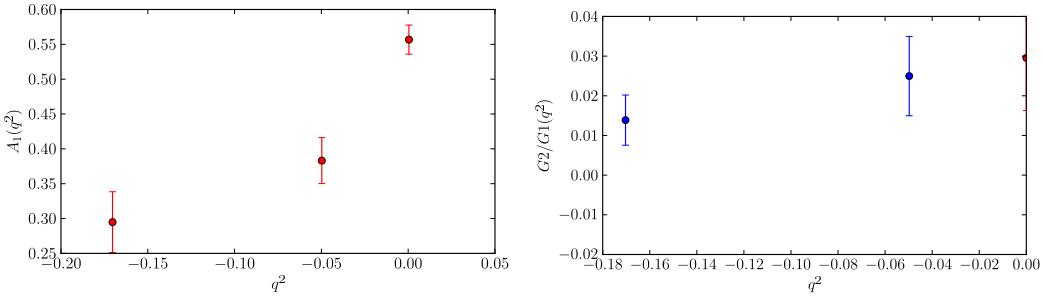

Figure B.28: $A_1(q^2)$ and $G2/G1(q^2)$ on the 32^3, $m_l = 0.004$ ensemble.

B.5 32^3, $m_l = 0.006$

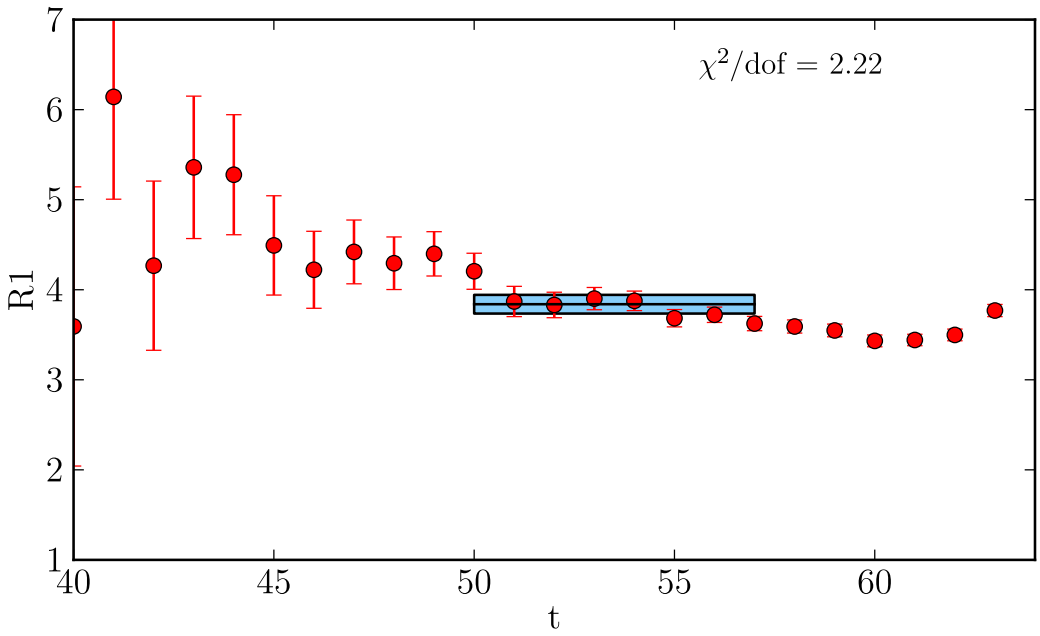

Figure B.29: Ratio R_1 on the 32^3, $m_l = 0.006$ ensemble.

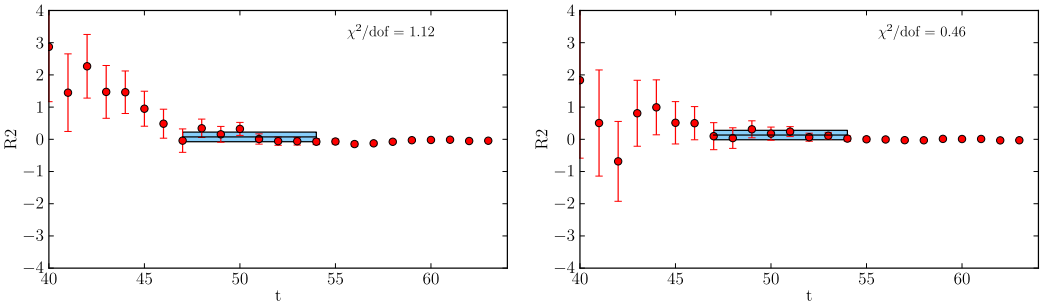

Figure B.30: Ratio R_2 on the 32^3, $m_l = 0.006$ ensemble, at the first (left) and second (right) non-zero momentum.

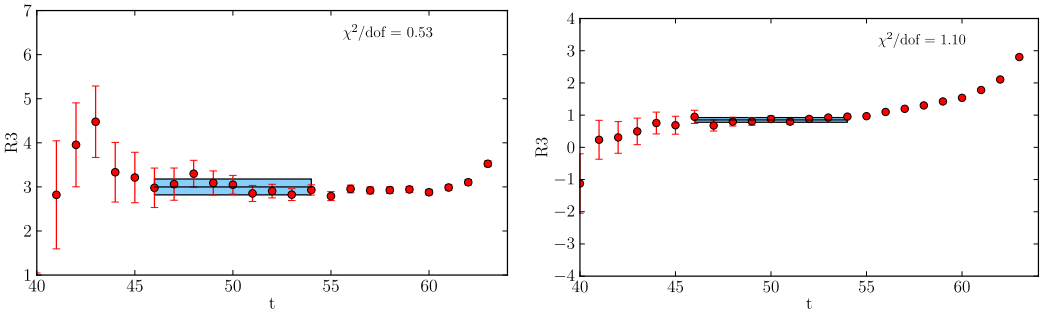

Figure B.31: Ratio R_3 on the 32^3, $m_l = 0.006$ ensemble, at the first (left) and second (right) non-zero momentum.

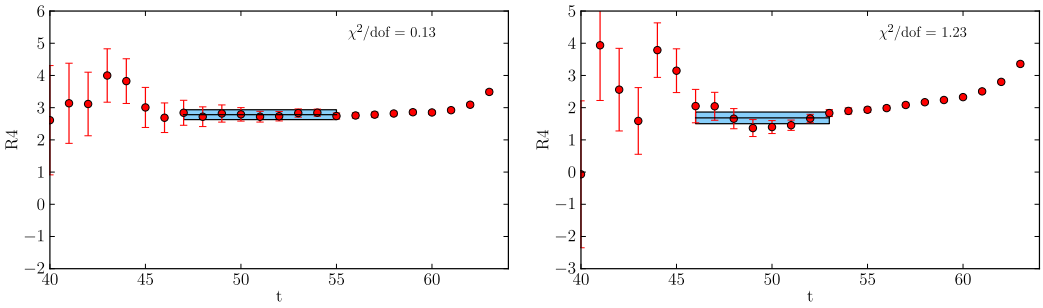

Figure B.32: Ratio R_4 on the 32^3, $m_l = 0.006$ ensemble, at the first (left) and second (right) non-zero momentum.

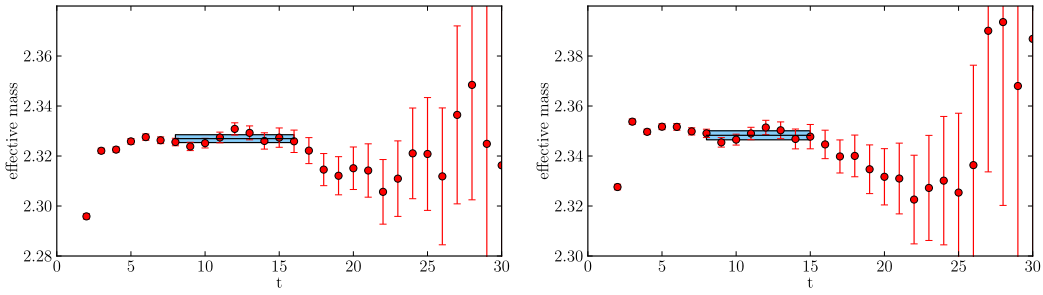

Figure B.33: B meson (left) and B^* meson effective mass on the 32^3, $m_l = 0.006$ ensemble, at zero momentum.

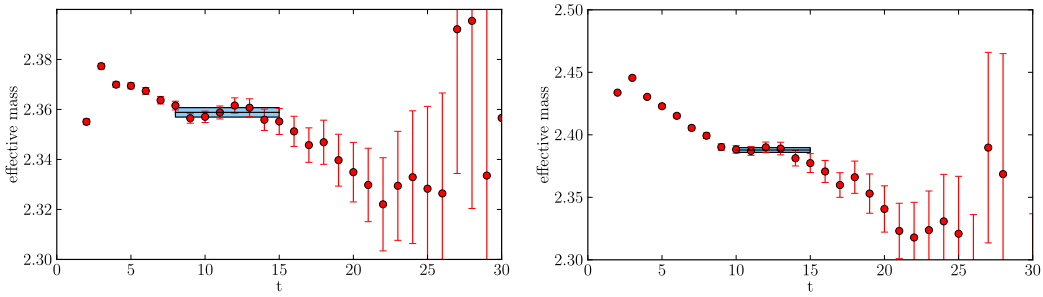

Figure B.34: B^* meson effective mass on the 32^3, $m_l = 0.006$ ensemble at the first non-zero momentum (left) and the second non-zero momentum (right).

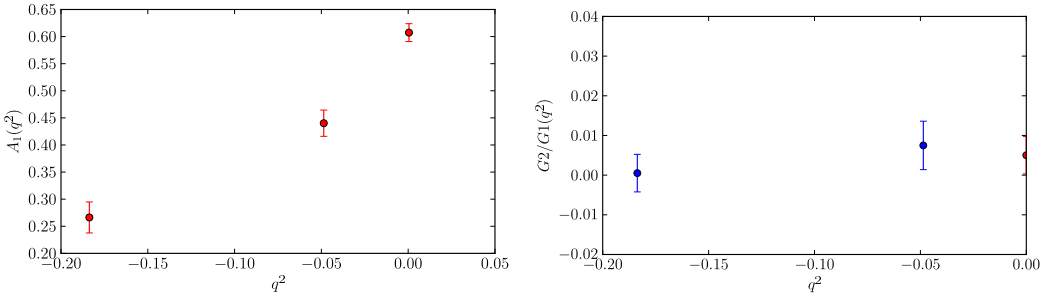

Figure B.35: $A_1(q^2)$ and $G2/G1(q^2)$ on the 32^3, $m_l = 0.006$ ensemble.

B.6 32^3, $m_l = 0.008$

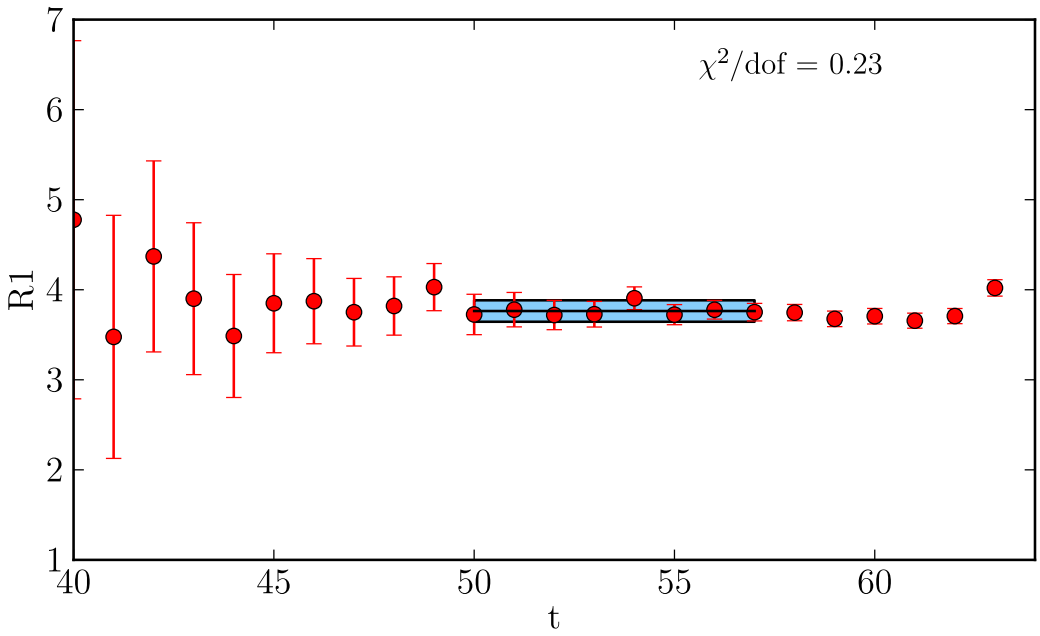

Figure B.36: Ratio R_1 on the 32^3, $m_l = 0.008$ ensemble.

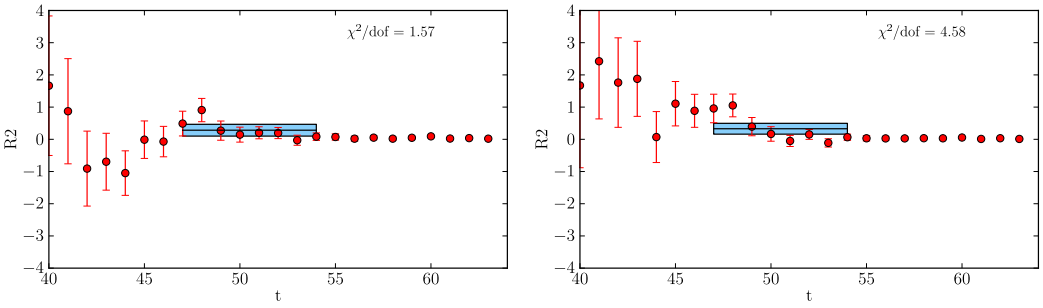

Figure B.37: Ratio R_2 on the 32^3, $m_l = 0.008$ ensemble, at the first (left) and second (right) non-zero momentum.

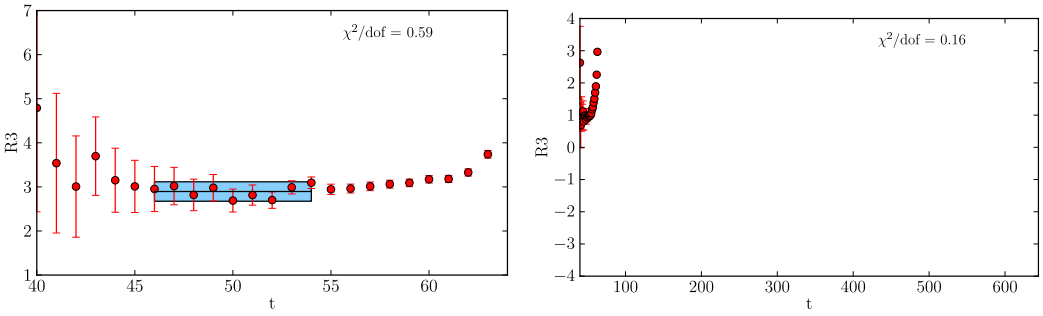

Figure B.38: Ratio R_3 on the 32^3, $m_l = 0.008$ ensemble, at the first (left) and second (right) non-zero momentum.

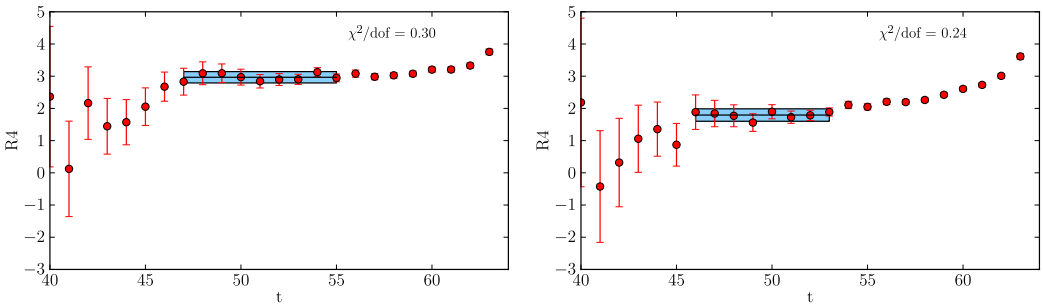

Figure B.39: Ratio R_4 on the 32^3, $m_l = 0.008$ ensemble, at the first (left) and second (right) non-zero momentum.

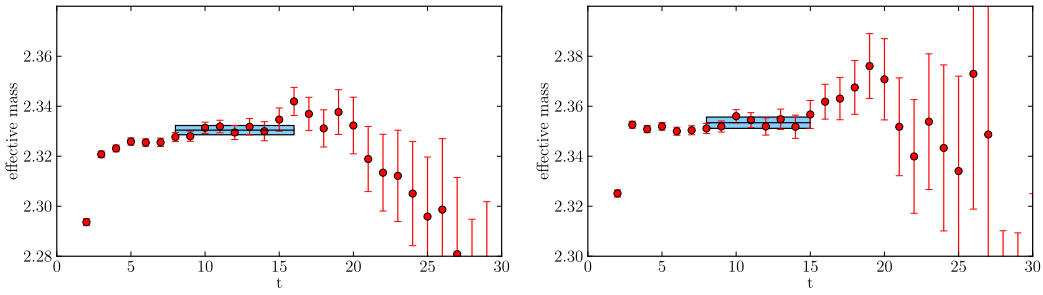

Figure B.40: B meson (left) and B^* meson effective mass on the 32^3, $m_l = 0.008$ ensemble, at zero momentum.

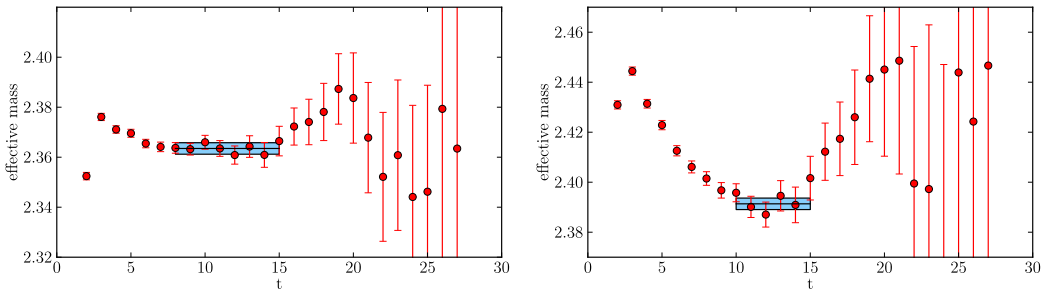

Figure B.41: B^* meson effective mass on the 32^3, $m_l = 0.008$ ensemble at the first non-zero momentum (left) and the second non-zero momentum (right).

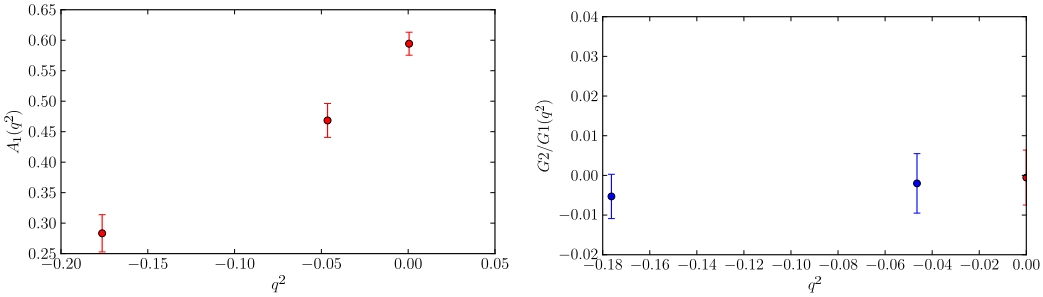

Figure B.42: $A_1(q^2)$ and $G2/G1(q^2)$ on the 32^3, $m_l = 0.008$ ensemble.

References

[1] J. Charles *et al.*, The European Physical Journal C **41**, 1 (2005).

[2] A. Lenz *et al.*, Physical Review D **83**, 036004 (2011), arXiv:1008.1593v3.

[3] Y. Aoki *et al.*, Physical Review D **86**, 116003 (2012), 1206.2554.

[4] A. Y. Smirnov, Journal of Physics: Conference Series **53**, 44 (2006).

[5] S. Chatrchyan *et al.*, Journal of High Energy Physics **2013**, 81 (2013).

[6] G. Aad *et al.*, Physics Letters B **716**, 1 (2012).

[7] ATLAS Collaboration, (2013), arXiv:1307.1432.

[8] S. Chatrchyan *et al.*, Physical Review Letters **110**, 081803 (2013).

[9] J. S. Bell, *A Thesis*, PhD thesis, Birmingham University, 1954.

[10] G. Lüders, Det. Kong. Danske Videnskabernes Selskab Mat.-fysiske Meddelelser **28** (1954).

[11] G. 't Hooft, Physical Review Letters **37**, 8 (1976).

[12] G. 't Hooft, Physical Review D **14**, 3432 (1976).

[13] R. D. Peccei, *The Strong CP Problem and Axions* (Springer Berlin Heidelberg, 2008).

[14] J. Goldstone, A. Salam, and S. Weinberg, Physical Review **127**, 965 (1962).

[15] S. L. Glashow, Nuclear Physics **22**, 579 (1961).

[16] S. Weinberg, Physical Review Letters **19**, 1264 (1967).

[17] N. Cabibbo, Physical Review Letters **10**, 531 (1963).

[18] M. Kobayashi and T. Maskawa, Progress of Theoretical Physics **49**, 652 (1973).

[19] L.-L. Chau and W.-Y. Keung, Physical Review Letters **53**, 1802 (1984).

[20] A. D. Sakharov, Soviet Physics Uspekhi **34**, 392 (1991).

[21] J. H. Christenson, J. W. Cronin, V. L. Fitch, and R. Turlay, Physical Review Letters **13**, 138 (1964).

[22] H. Burkhardt *et al.*, Physics Letters B **206**, 169 (1988).

[23] V. Fanti *et al.*, Physics Letters B **465**, 335 (1999).

[24] A. Alavi-Harati *et al.*, Physical Review Letters **83**, 22 (1999).

[25] B. Aubert *et al.*, Physical Review Letters **89**, 201802 (2002).

[26] K. Abe *et al.*, Physical Review D **66**, 071102 (2002).

[27] R. Aaij *et al.*, Physics Letters B **712**, 203 (2012).

[28] A. J. Buras, M. Jamin, and P. H. Weisz, Nuclear Physics B **347**, 491 (1990).

[29] T. Inami and C. S. Lim, Progress of Theoretical Physics **65**, 297 (1981).

[30] J. Beringer *et al.*, Physical Review D **86**, 010001 (2012).

[31] E. Gámiz, C. Davies, G. Lepage, J. Shigemitsu, and M. Wingate, Physical Review D **80**, 014503 (2009), arXiv:0902.1815v3.

[32] A. Bazavov *et al.*, Physical Review D **86**, 034503 (2012), arXiv:1205.7013v1.

[33] J. Laiho, E. Lunghi, and R. S. Van de Water, Physical Review D **81**, 034503 (2010).

[34] E. Lunghi and A. Soni, Physics Letters B **697**, 323 (2011).

[35] K. Hara *et al.*, Physical Review Letters **110**, 131801 (2013).

[36] T. Kawanai, R. S. Van de Water, and O. Witzel, PoS Lattice , 7 (2012), 1211.0956.

[37] K. Wilson, Physics Reports **12**, 75 (1974).

[38] K. Wilson, Reviews of Modern Physics **47**, 773 (1975).

[39] A. Pich, Effective Field Theory, in *Lectures at the 1997 Les Houches Summer School*, pp. 949–1049, 1998, 9806303.

[40] A. V. Manohar, Effective Field Theories, in *Perturbative and nonperturbative aspects of quantum field theory*, pp. 311–362, Springer, 1997, 9606222.

[41] A. Pich, Reports on Progress in Physics **58**, 563 (1995), 9502366.

[42] M. R. Scherer, Stefan and Schindler, hep-ph/0505265 (2005).

[43] D. B. Kaplan, Nuclear Physics , 79 (2005), 0510023.

[44] J. Goldstone, A. Salam, and S. Weinberg, Physical Review **127**, 965 (1962).

[45] S. Coleman, J. Wess, and B. Zumino, Physical Review **177**, 2239 (1969).

[46] C. Callan, S. Coleman, J. Wess, and B. Zumino, Physical Review **177**, 2247 (1969).

[47] V. Belyaev, V. Braun, A. Khodjamirian, and R. Rückl, Physical Review D **51**, 6177 (1995).

[48] S. Ahmed *et al.*, Physical Review Letters **87**, 251801 (2001).

[49] K. Symanzik, Nuclear Physics B **226**, 187 (1983).

[50] K. Symanzik, Nuclear Physics B **226**, 205 (1983).

[51] B. Sheikholeslami and R. Wohlert, Nuclear Physics B **259**, 572 (1985).

[52] P. Luscher, M. and Weisz, Communications in Mathematical Physics **97**, 59 (1985).

[53] M. Lüscher and P. Weisz, Nuclear Physics B **479**, 429 (1996).

[54] G. Lepage and P. Mackenzie, Physical Review D **48**, 2250 (1993).

[55] M. Creutz, Physical Review D **21**, 2308 (1980).

[56] S. Adler, Physical Review D **23**, 2901 (1981).

[57] D. Callaway and A. Rahman, Physical Review D **28**, 1506 (1983).

[58] M. Clark, A. Kennedy, and Z. Sroczynski, Nuclear Physics B - Proceedings Supplements **140**, 835 (2005).

[59] K. Wilson, Physical Review D **10**, 2445 (1974).

[60] P. Weisz, Nuclear Physics B **212**, 1 (1983).

[61] P. Weisz and R. Wohlert, Nuclear Physics B **236**, 397 (1984).

[62] Y. Iwasaki, **118**, 20 (1983), 1111.7054.

[63] Y. Iwasaki and T. Yoshié, Physics Letters B **143**, 449 (1984).

[64] T. Takaishi, Physical Review D **54**, 1050 (1996).

[65] Y. Aoki *et al.*, Physical Review D **69**, 074504 (2004), 0211023v2.

[66] H. Nielsen and M. Ninomiya, Physics Letters B **105**, 219 (1981).

[67] P. Ginsparg and K. Wilson, Physical Review D **25**, 2649 (1982).

[68] R. Narayanan, Physics Letters B **302**, 62 (1993), 9212019.

[69] R. Narayanan and H. Neuberger, Nuclear Physics B **412**, 574 (1994), 9307006.

[70] R. Narayanan and H. Neuberger, Nuclear Physics B **443**, 305 (1995).

[71] D. B. Kaplan, Physics Letters B **288**, 342 (1992).

[72] R. Edwards and U. Heller, Physical Review D **63** (2001).

[73] A. D. Kennedy, Algorithms for Dynamical Fermions, in *Perspectives in Lattice QCD*, p. 62, 2006, 0607038.

[74] S. Aoki and Y. Taniguchi, Physical Review D **59**, 094506 (1999), 9811007.

[75] T. Blum, A. Soni, and M. Wingate, Physical Review D **60**, 114507 (1999), 9902016v2.

[76] Y. Shamir, Nuclear Physics B **406**, 90 (1993), 9303005v1.

[77] P. M. Vranas, Physical Review D **57**, 1415 (1998), 9705023.

[78] R. Baron *et al.*, Journal of High Energy Physics **2010**, 111 (2010).

[79] R. Baron *et al.*, Computer Physics Communications **182**, 299 (2011).

[80] R. A. Briceño, H.-W. Lin, and D. R. Bolton, Physical Review D **86**, 094504 (2012).

[81] E. Eichten and B. Hill, Physics Letters B **234**, 511 (1990).

[82] M. Albanese *et al.*, Physics Letters B **192**, 163 (1987).

[83] A. Hasenfratz, R. Hoffmann, and F. Knechtli, Nucl.Phys.Proc.Suppl. **106**, 3 (2002), 0110168.

[84] G. Lepage, Nuclear Physics B - Proceedings Supplements **26**, 45 (1992).

[85] A. X. El-Khadra, A. S. Kronfeld, and P. B. Mackenzie, Physical Review D **55**, 3933 (1997), 9604004.

[86] S. Aoki, Y. Kuramashi, and S.-i. Tominaga, Progress of Theoretical Physics **109**, 383 (2003), 0107009.

[87] N. Christ, M. Li, and H.-W. Lin, Physical Review D **76**, 074505 (2007), 0608006.

[88] B. Efron, *The Jackknife, the Bootstrap and Other Resampling Plans* (Society for Industrial and Applied Mathematics, 1982).

[89] M. Alford, T. Klassen, and P. Lepage, Nuclear Physics B - Proceedings Supplements **47**, 370 (1996).

[90] A. C. Lichtl, *Quantum Operator Design for Lattice Baryon Spectroscopy*, Ph.d, Carnegie Mellon University, 2006, 0609019.

[91] T. DeGrand and A. Hasenfratz, Spectroscopy , 21 (2000), 0012021.

[92] R. B. Lehoucq and D. C. Sorensen, SIAM Journal on Matrix Analysis and Applications **17**, 789 (1996).

[93] T. Kalkreuter, Computer Physics Communications **93**, 33 (1996).

[94] J. Foley *et al.*, Computer Physics Communications **172**, 24 (2005), 0505023.

[95] G. S. Bali, S. Collins, and A. Schaefer, Computer Physics Communications **181**, 26 (2009), 0910.3970.

[96] S.-J. Dong and K.-F. Liu, Phys. Lett. **B328**, 130 (1994).

[97] C. McNeile and C. Michael, Physical Review D **73**, 074506 (2006), PhysRevD.73.074506.

[98] P. Boyle, C. Kelly, R. Kenway, and A. Jüttner, Journal of High Energy Physics **2008**, 086 (2008), 0804.1501.

[99] T.-M. Yan *et al.*, Physical Review D **46**, 1148 (1992).

[100] G. N. P. Colangelo, F. De Fazio, Phys.Lett. B **334**, 175 (1994), 9406320.

[101] P. Colangelo *et al.*, Physics Letters B **339**, 151 (1994).

[102] V. Belyaev, V. Braun, A. Khodjamirian, and R. Rückl, Physical Review D **51**, 6177 (1995).

[103] H. Dosch and S. Narison, Physics Letters B **368**, 163 (1996).

[104] P. Colangelo and F. De Fazio, The European Physical Journal C **4**, 503 (1998).

[105] A. Anastassov *et al.*, Physical Review D **65**, 032003 (2002).

[106] G. M. de Divitiis *et al.*, Journal of High Energy Physics **1998**, 010 (1998), 9807032.

[107] A. Abada *et al.*, Physical Review D **66**, 074504 (2002), 0206237.

[108] W. Detmold, C.-J. Lin, and S. Meinel, Physical Review D **85**, 114508 (2012).

[109] W. Detmold, C.-J. Lin, and S. Meinel, Physical Review D **84**, 094502 (2011), 1108.5594.

[110] D. Bečirević and F. Sanfilippo, Physics Letters B **721**, 94 (2013), 1210.5410.

[111] C. Sachrajda and G. Villadoro, Physics Letters B **609**, 73 (2005).

[112] J. Flynn, A. Jüttner, and C. Sachrajda, Physics Letters B **632**, 313 (2006).

[113] M. Foster and C. Michael, Physical Review D **59**, 074503 (1999).

[114] C. Gattringer and C. B. Lang, *Quantum chromodynamics on the lattice: an introductory presentation* (Springer Verlag, 2009).

[115] Y. Aoki *et al.*, Physical Review D **83**, 074508 (2011), 1011.0892.

[116] S. R. Sharpe, arXiv preprint hep-lat/07060218 , 22 (2007), 0706.0218.

[117] C. Allton *et al.*, Physical Review D **78**, 114509 (2008).

[118] D. J. Antonio *et al.*, Phys. Rev. D **77** (2008).

[119] S. Meinel, Physical Review D **82**, 114502 (2010).

[120] R. G. Edwards and B. Joo, Nucl. Phys. Proc. Suppl. **140**, 832 (2005).

[121] F. James and M. Roos, Computer Physics Communications **10**, 343 (1975).

[122] Y. Avni, The Astrophysical Journal **210**, 642 (1976).

[123] R. Casalbuoni *et al.*, Physics Reports **281**, 145 (1997), 9605342.

[124] C. Boyd and B. Grinstein, Nuclear Physics B **442**, 205 (1995), 9402340.

[125] A. Kronfeld, Physical Review D **62**, 014505 (2000), 0002008.

[126] M. B. Oktay and A. S. Kronfeld, Physical Review D **78**, 014504 (2008), 0803.0523.

[127] W. Detmold and C.-J. Lin, Physical Review D **71**, 054510 (2005), 0501007v2.

[128] D. Arndt and C.-J. Lin, Physical Review D **70**, 014503 (2004), 0403012v2.

[129] A. Hasenfratz, R. Hoffmann, and S. Schaefer, Physical Review D **78**, 014515 (2008), arXiv:0805.2369v1.

[130] M. Lüscher and F. Palombi, PoS Lattice **049**, 7 (2008), 0810.0946.

[131] R. Godang, ICHEP , 1 (2012).